Alma Mater Studiorum – Università di Bologna

DOTTORATO DI RICERCA IN
AUTOMOTIVE PER UNA MOBILITA' INTELLIGENTE

Ciclo 34

Settore Concorsuale: 09/A3 – PROGETTAZIONE INDUSTRIALE, COSTRUZIONI DI MACCHINE E METALLURGIA

Settore Scientifico Disciplinare: ING-IND/14 – PROGETTAZIONE MECCANICA E COSTRUZIONI DI MACCHINE

SMART TRACKING OF COMPOSITE PARTS: FEASIBILITY STUDY AND EFFECTS ON MECHANICAL BEHAVIOUR

Presentata da: Ambrosini Daniele

Coordinatore Dottorato
Nicolò Cavina

Supervisore
Alessandro Pirondi

Co-supervisore
Dario Croccolo

Esame finale anno 2022

ABSTRACT

This research proposes a solution for integrating RFID - Radio Frequency Identification technology within a structure based on CFRPs - Carbon Fiber Reinforced Polymers. Therefore, the main objective is to use technology to monitor and track composite components during manufacturing and service life.

The study can be divided into two macro-areas. The first portion of the research evaluates the impact of the composite materials used on transmitting the electromagnetic signal to and from the tag. RFID is a wireless technology that uses electromagnetic fields (radio waves) to transfer data to track and trace goods associated with the tags. In the first instance, a feasibility study was carried out to assess using commercially available tags. Then, after evaluating different solutions, it was decided to incorporate the tags into coupons during production.

The second portion of the research is focused on evaluating the impact on the composite material's resistance to tag embedding. It starts with designing tensile test specimens through the FEM model with different housing configurations. Subsequently, the best configuration was tested in the facilities of the

In the Faculty of Aerospace Engineering at TU Delft, particularly in the Structure & Materials Laboratory, two tests were conducted: the first one based on ASTM D3039/D3039 - 14 - Standard Test Method for Tensile Properties of Polymer Matrix Composite Materials, the second one dividing the path to failure into failure intervals in a load-unload-reload (ramps).

Both tests were accompanied by instruments such as DIC (Digital Image Correlation), AE (Acoustic Emission), C-Scan and Optical Microscopes.

The expected result of the inclusion of RFID tags in composite components is that it brings added value to the parts with which it is associated without affecting too much its mechanical properties. This comes first from the automatic identification of RFID during the production cycle and its useful life. As a result, improvements were made in the design of production facilities.

LIST OF CONTENTS

LIST OF FIGURES

LIST OF TABLES

NOMENCLATURE

Nomenclature	*Meaning*
CFRPs	Carbon Fiber Reinforced Polymers
RFID	Radio Frequency Identification
FBG	Fiber Bragg Grating
RUL	Remaining Useful Life
SHM	Structural Health Monitoring
JIT	Just-In-Time
IoT	Internet of Things
Auto-ID	Automatic Identification
NDT	Non-Destructive Test
ER	Electrical Resistance
CNT	Carbon nanotubes
RF	Radio Frequencies
IFF	Identification Friend or Foe
EAS	Electronic Article Surveillance
IC	Integrated Circuit
UID	Unique Identification
LF	Low Frequency
HF	High Frequency
UHF	Ultra-High Frequency
DoE	Design of Experiment
DCHP	Die-cut hole pattern
ANOVA	Analysis of Variance
RSM	Response Surface Methodology
FEM	Finite Element Method
DIC	Digital Image Correlation
AE	Acoustic Emission
PZT	Piezoelectric

1 INTRODUCTION

1.1 SMART MATERIALS

The introduction discusses incorporating electronic sensors into carbon fibre reinforced polymers (CFRP) and Radio Frequency Identification (RFID) to satisfy wireless communication with these sensors. On the one hand, to satisfy the wireless communication with the sensor, and on the other hand, to control the structural health of the material under different loads. This chapter explains why material tracking and identification are necessary, how wireless detection is proper during production, and how detection enables intelligent materials. Finally, the introductory chapter sets out the research objective, the executive summary, and the thesis structure.

There are different reasons why researchers and engineers try to make materials capable of detecting changes or acquiring data during production.

Firstly, the production of reinforced polymer materials is characterised by making thicker products than necessary, mainly due to defects during production. There is a wide range of defects during the production process, but the most common is "porosity", i.e., the presence of small voids in the matrix. The voids can be caused by an incorrect curing process, such as time, temperature, pressure or even the outflow of resin from the vacuum bag. The porosity variation within the structure can reduce mechanical properties such as interlaminar shear stress [1]. Therefore, researchers and engineers try to monitor the manufacturing process by acquiring as much information as possible with sensors [2, 3, 4, 5]. Including sensors within components can lead to higher-quality manufacturing, thus facilitating designers in the design phase and reducing weight.

A second reason is to understand material conditions during production. Indeed, residual stresses may accumulate during the curing process within the structure. Therefore, some research studies use sensors such as fibre optics or FBG (Fiber Bragg Grating) embedded within the structure for health monitoring [6, 7]. Many of these residual deformations can affect the RUL (Remain Useful

Life) and thus reduce the loads borne during the useful life. During service life, the same sensors are also used as SHM (Structural Health Monitoring) to detect stresses.

For this reason, once the parts are produced, they can be spot tested to assess whether they meet the minimum design requirements. Therefore, coupling structural monitoring sensors with products helps the designer and the production, making it more efficient and reducing costs. This combination allows composite materials to become more economically desirable.

A further reason why research and industry are interested in integrating sensors into composite materials is due to the increasing demand for information during the industrial process. Nowadays, this is called Industry 4.0. Many companies have started to use advanced information technologies and methods to facilitate the flow of information. In recent years, the increasing volume of data generated and collected from the various production steps and during service life has led Industry 4.0 to integrate and analyse data to apply decision-making processes. The application of decision-making processes improves each step's performance and the exchange of data flows [8]. Combining sensors with objects has improved many industrial areas by connecting machines, objects and even people without wires [9]. The fourth industrial revolution began with the emergence of the Internet and industrial technologies combined into the Internet of Things (IoT). The main body is the concept of information exchange between smart objects and intelligent management systems.

The driving force behind this new industrial revolution is the RFID system. RFID technology allows turning any object into a wirelessly communicating device. Moreover, this technology can be coupled with sensor technology to monitor the structure's mechanical and physical properties [10]. For example, monitoring and detecting damage from various events can be used to assess the need for maintenance based on the actual use rather than on a specific time window.

1.1.1 AUTO-ID AND RFID REQUEST

There is a growing demand for integrating sensors into components in the industrial environment. This study was born from the collaboration with "Dallara Automobili" to proceed with a feasibility study to incorporate a sensor which can track and monitor objects, logistical and mechanical property, passing from the production process to the in-service life.

As reported in [11] the "Enabling Technologies and Approaches - sensors and measurements" section, it was pointed out that the sensors did not have good integration between data and production processes.

This need for interconnection and communication of data and products to the production processes has led to the informatization of the product life cycle management, avoiding errors in the

production management. In addition, the JIT – Just-In-Time - production concept and the cycle time reduction have been increasingly used in the automotive industry [12, 13]. This concept, combined with IoT and sensors for unique automatic identification (Auto-ID) concerning RFID tags, has enabled many logistics applications to become intelligent. Auto-ID systems are based on associating a name or identifier to a physical object through automatic reading. With the help of this digitalisation and the new technologies available, many companies can monitor the various stages of the production chain in real-time. [14]. Automatic identification has dramatically impacted the supply chain of goods to the final consumer in the automotive sector. Another aspect to consider is that using RFID tags can solve the problem of anti-counterfeiting. As Strassner et al. [12] explained, the unique code embedded in the tag is exploited. Tag readers should be installed in centres where vehicle parts can be validated, sold, and replaced.

1.1.2 SENSOR INTEGRATION

There is an increasing demand for integrating sensors for internal damage detection and Non-Destructive Testing (NDT) during the production process [11]. These processes would help understand the life of composite components, increasing their use in various applications.

Thus, integrating sensors for structural monitoring has the common objective of assessing in real-time what stresses materials are exposed to, such as mechanical or thermal stress.

In some cases, the sensors are an integral part of the structure. In other cases, sensors are integrated to assess the material's mechanical strength, but they make structural changes and create defects. Many sensors, such as optical fibres or FBGs, have the problem of being electrically connected outside the material. A further issue is that there is local structural monitoring with these sensors. While the component is stressed, the distortion of the emitted light beam is evaluated.

Other applications directly exploit the material’s electrical resistance (ER) [15, 16]. The ER change is associated with a variation in the material's intrinsic properties, so it can be used to assess the presence of damage.

Adhesives with embedded carbon nanotubes are increasingly used and studied [17]. Carbon nanotubes (CNTs) are subject to change when they undergo mechanical deformation. They are mainly used for strain sensing. Here again, electrical resistivity is measured, which increases linearly with strain. CNTs are often used in mat form to evaluate the performance of bonded adhesive joints [18, 19]. Again, the main disadvantage is using electrical cables protruding from the affected part.

Therefore, using these sensors always requires external energy to obtain measurements of the stresses occurring on the structure connected to them.

New research exploits RFID sensors for monitoring the curing process, but with limitations. Unlike in the building sector, where active tags (with a battery) can be used, which use an additional sensor connected to them, such as a temperature or strain sensor, passive tags (without a battery) are used in the automotive or aerospace sector. In the first case, storing information in the sensor's memory is possible. In the second case, data transmission occurs in real-time, as it is impossible to store data. In [4], the difference of the RSSI (Received Signal Strength Indicator) signal of the RFID tag placed inside a glass fibre component during the curing process is evaluated. The RFID technology is combined with a cure monitoring system, thus exploiting the full potential of both technologies. The main limitation of this technology is the transmissibility of the signal when placed on electrically conductive materials, such as carbon fibre. In fact, in [2], they addressed the problem of embedding an RFID sensor during the manufacturing process, either in a material "transparent" to electro-magnetic waves, such as glass fibre, or on conductive material, such as carbon fibre.

None of them evaluated the possible reduction of mechanical properties due to introducing the RFID label into the composite samples.

1.2 COMPOSITE MATERIAL

Composite materials can be defined by combining more distinct materials with different properties, resulting in improved properties [20]. The two main components are usually fibre and matrix. Fibres can be carbon, glass, and aramid. The composite products can be produced in different forms, such as continuous and discontinuous fibre, oriented or disoriented (random) Fig.1. The matrix is a polymeric material that can be thermosets or thermoplastics. Layers composed of continuous fibres are nominally laminated and placed (fibre orientation) in such a way to achieve strength in one or more main directions. The purpose of the fibres is to give strength and stiffness, whereas the matrix protects the fibres from the external environment. In addition, the matrix defines the position of the fibres.

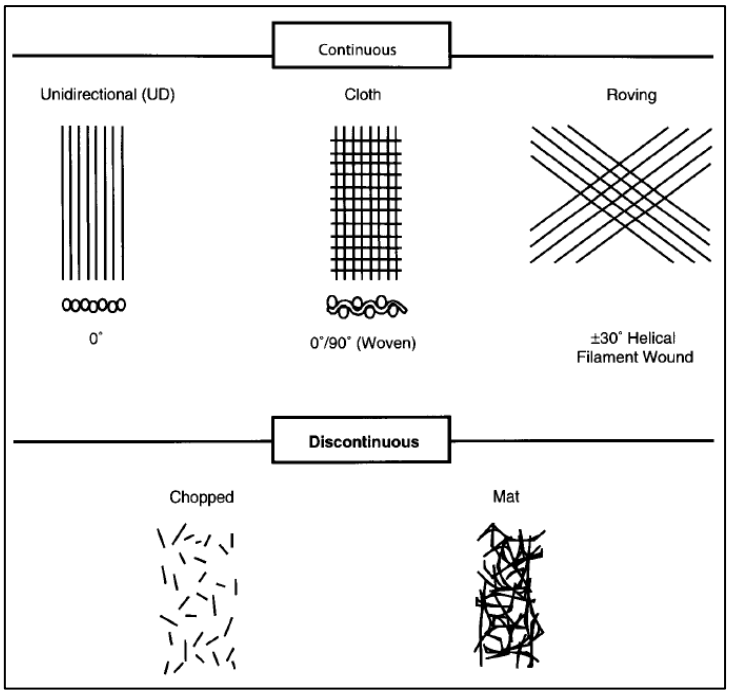

Figure 1 - Reinforcement option [20]

Composite materials combine high structural performance with relatively low density. They are often used in various fields, for example, aerospace or biomedical, in structural applications such as civil or automotive. These fields require high stiffness and resistance to fatigue cycles, corrosion resistance and lightweight.

1.3 CURING PROCESS IN COMPOSITE MATERIAL

Fig. 2 shows a typical process used to produce pre-preg components.

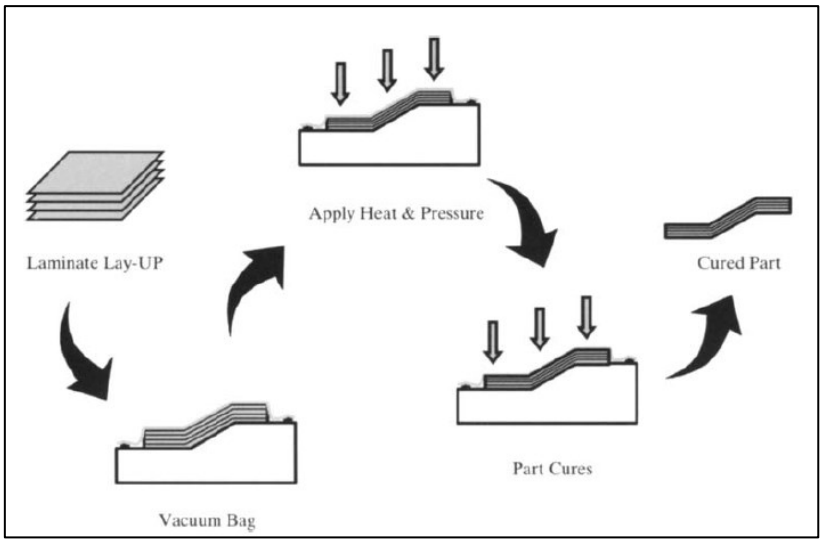

Figure 2 - Pre-preg lay-up process [20]

The pre-preg is laminated onto a tool (aluminium plate or mould), following a playbook (lamination sequence derived from the design). Subsequently, the laminate is placed in a vacuum bag (Fig.2), extracting the air inside the laminate with a relative pressure of -1bar. Afterwards, the component is placed in the vacuum bag and cured in an autoclave (Fig.3), following a cure cycle, i.e., defining the internal pressure and temperature based on the viscosity cycle of the resin. This determines the mechanical characteristics of the final part.

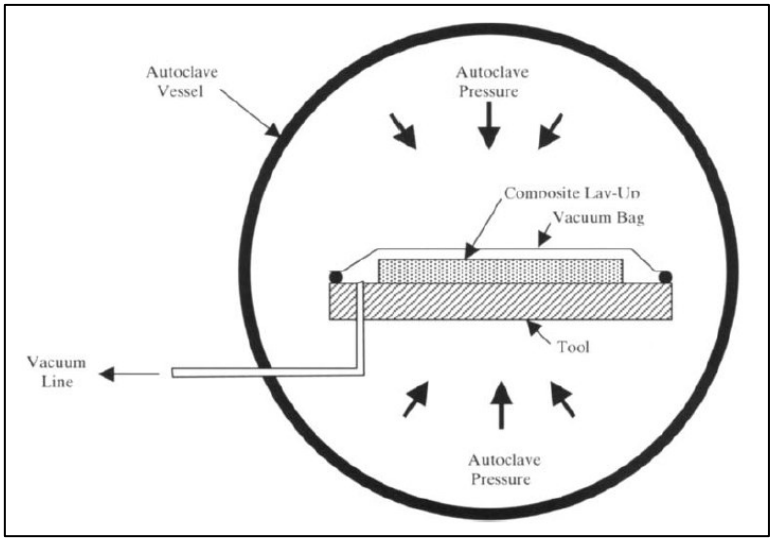

Figure 3 - Autoclave process curing [20]

The layers can be supplied as dry fibre or pre-impregnated (pre-preg), i.e., resin. Pre-pregs are fabrics soaked with epoxy resin (thermoset) and its catalyst. It has the advantage that the resin is uniformly distributed. Pre-preg is available with many fibres and different matrix combinations. It is

stored at a cold temperature (approximately 18°C and 40% humidity). It is commonly supplied in rolls.

Before being formed, it is taken to the nesting or cutting plotter. Finally, the extraction of the component takes place with subsequent finishing and possible NDT.

1.4 AIM OF THE RESEARCH

This research aims to develop an integration of an RFID tag inside a carbon fibre material component, test and evaluate the use of RFID tags to monitor and communicate wirelessly and evaluate our final specimen's mechanical properties. This part of the research addresses how the RFID tag affects the mechanical structure of the CFRPs laminate.

1.4.1 RESEARCH OBJECTIVE

Research and evaluation of embedded RFID tags on the readability performance of electromagnetic transmission. The methods and approach of this part of the research examine the readability performance of the electromagnetic transmission of embedded RFID tags. Then test and evaluate the performance factors of embedded RFID tags on the readability of electronic transmission. This study aims to implement an RFID tag ahead of the production process of composite materials, and then be able to provide information on the entire production chain while limiting human intervention to a minimum. Therefore, the transponder provides data at each manufacturing step, as shown in Fig.4. Also, as mentioned above, the tag works as anti-counterfeiting during the component service life. The flow shown in Fig. 5 refers to the service-life of a racing car component.

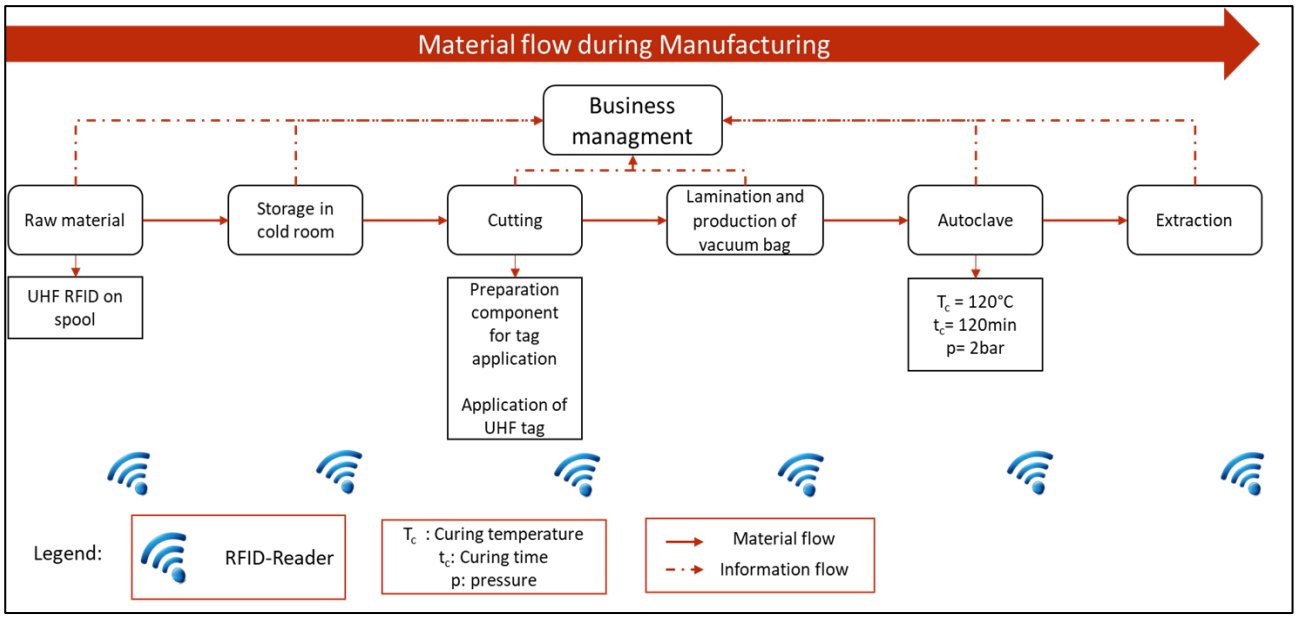

Figure 4 - Embedding process of RFID tag into CFRPs [21]

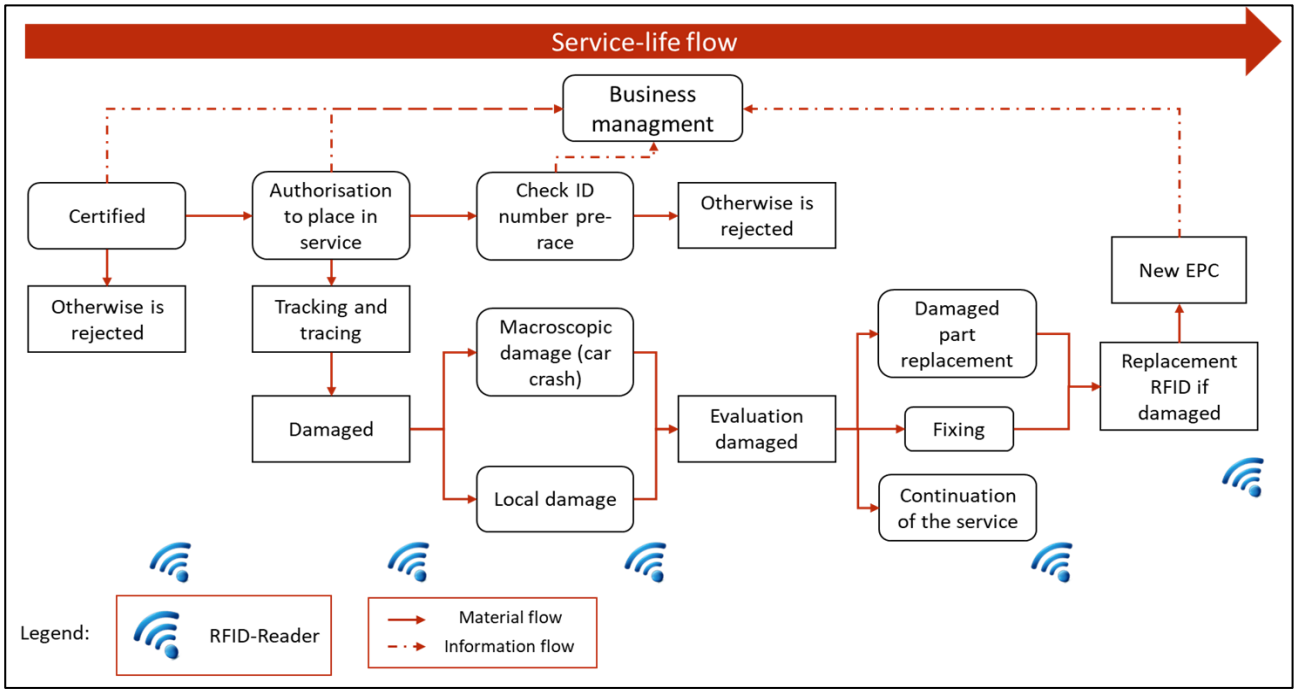

Figure 5 - Service-life of an embedded RFID tag [21]

To evaluate the impact of embedded RFID tags on the mechanical properties of a composite structure. The methods for this research are to evaluate, through destructive as well as Non-Destructive Test methods and instrumentation, the influence of the presence of the RFID tag on the mechanical properties

1.5 DISSERTATION STRUCTURE

The thesis follows an engineering format divided into a general introduction to the problem, two macro-areas referring to Smart Tracking and test monitoring, the background, methodology, result and discussion, and a final chapter. The introduction explains why this research was started. The section describes the need for wireless sensing in composite materials, especially CFRPs, explaining the physical limitations of the material and the need for mechanical testing using other sensors.

Chapter 2 discusses the literature review on RFID technologies, the methodology used to include specific objectives to be achieved and the tools used to test and validate the tests. Finally, a report on this part of the research results is helpful for the following macro-area.

Chapter 3 discusses the literature review on the technologies used to monitor mechanical experiments—an outline of mechanical simulations. In addition, the methodology used is explained, including the tools used to test and validate. Finally, the results of mechanical tests are discussed and interpreted.

Chapter 4 concludes the research and provides a summary of the experiments conducted. It includes the limitations of the research and describes the next steps in the research sequence.

2 SMART TRACKING

2.1 BACKGROUND OF RFID TECHNOLOGY

2.1.1 RFID ORIGIN

RFID is a technology based on identifying a product through an Electro-Magnetic (EM) signal or via radiofrequency (RF). Identification implies storing electronic data on a transponder assigned to a unique identity, allowing precise identification. The system employs electromagnetic signals, i.e., without wires and the components being visible (as with barcodes) or even with a direct line-of-sight.

The first mention of radio frequency identification technology dates back to the 1930s. IFF, or Friend or Foe Identification, arose from the need to automatically identify allied aircraft from enemy aircraft via RF (Radio Frequency) [22, 23, 24, 25]. From the 1950s, the development of RFID technology was extended to the non-military field. EAS (Electronic Article Surveillance) systems were created to solve the anti-shoplifting function inside large shopping centres [26]. The presence of an active transponder through a gate (composed of antennas) would trigger the alarm. Such systems are commonly used in libraries or clothing retail shops. The basic technology was developed to track cars' manufacturing process or anti-shoplifting in commerce. RFID technology began to circulate in the early 1990s, and unlike EAS systems, it allows automatic product identification. Today, there are several commercial and low-cost solutions.

2.1.1.1 STRUCTURE OF THE SYSTEM

RFID technology focuses on tags, but it is more accurate to evaluate the whole system, including transponders and other essential components. The RFID system consists of three basic elements, as shown in Fig.6:

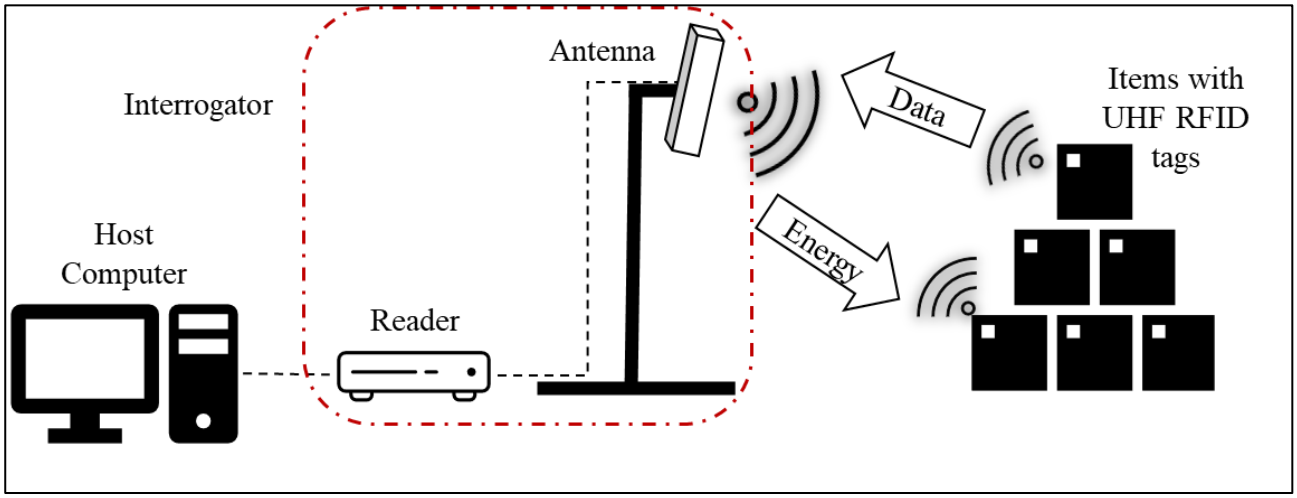

Figure 6 - RFID system

2.1.1.2 TAG

Tags or even transponders are composed of an integrated circuit (IC), or chip, coupled to an antenna and packaged on a carrier, such as a capsule, or inserted between two laminae, eventually coupled to a product. Tags can offer different performances depending on the power source and operating frequency. The variables help choose which application a particular tag can be used for and thus determine the costs. Current tags have their identification functionality on an integrated circuit (IC) or chip with memory. The chip is associated with a unique identification code (UID) transmitted via RF through the antenna to a host capable of collecting the data received [22, 26].

2.1.1.3 INTERROGATOR

The interrogator consists of a reader and one or more antennas. The antenna is a bidirectional transmitter, governed by the reader, often networked with management information systems. The readers communicate with the tags via RF to acquire information. The reader can run an anti-collision protocol in environments with many tags to avoid possible communication problems. Anti-collision protocols enable readers to communicate quickly with many tags and serial orders. RF readers power and communicate with passive tags, as they do not have an onboard battery and operate on the readers. There are different models of readers on the market, with their shape, frequency band, and functionality.

Furthermore, they can communicate over a network rather than processing power and internal memory. Readers can be fixed or integrated into portable mobile devices. Fig.7 shows that the fixed antenna can be integrated into warehouse access portals to scan tags as the shipments arrive; or on shelves to make them “smart”, allowing the monitoring of the addition or removal of a product from

a shelf. The latter is a kind of electronic gun, like a barcode gun. Mobile readers allow an operator to inventory a warehouse through the aisles.

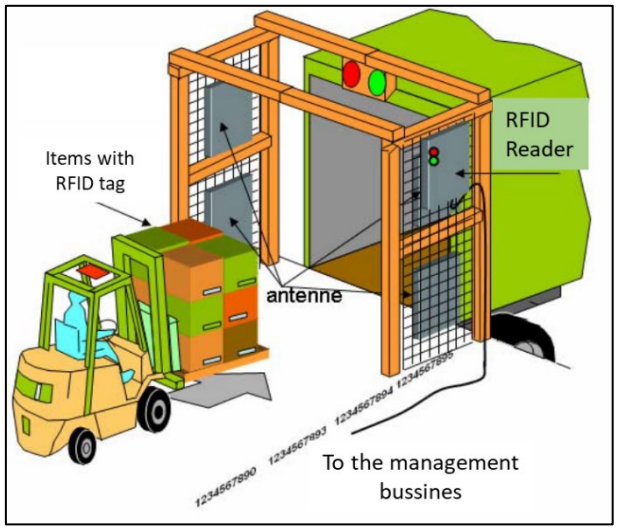

Figure 7 - RFID gate [27]

2.1.1.4 HOST SYSTEM

The physical and identification data of the tags collected employing the antennas-readers and then through the host system are transferred to the management applications of the company. The data collected may contain the product, tracking, sales, or expiry information. The control system can manage data along the supply or production chain or a central database. Everything is based on secure data transmission between the readers, the management system, and then the database.

2.1.2 THE POWER SUPPLY OF TAGS

Tags, or transponders, can obtain energy to be activated in different ways. The power supply to the tag is an important feature, as it determines its readability, cost, and available functionality. The shape and size are due to the presence or absence of an onboard power supply.

They can be classified in three ways: active, semi-passive, and passive.

Active tags use battery power to transmit and receive signals from readers or other tags. Active tags usually have a much more comprehensive reading range than passive tags. In contrast, semi-passive tags have the chip or sensors attached and use the battery, but the battery is not used to transmit the signal [22, 26]. Thus, the semi-passive tag can only activate when interrogated by a reader. The presence of the battery onboard offers more opportunities than passive tags but at a higher cost. Passive tags do not have energy sources, so they can not initiate communication. Passive tags

use the energy from the incoming RF signal to communicate. At low frequencies, they are collected by inductive coupling, and at high frequencies, by electromagnetic coupling. Among the three power types, passive tags have the shortest read range, are cheaper and easier to manufacture, and are easy to integrate.

For this reason, passive is the most used tag. Passive tags are based on the EPCglobal protocols. Without a power source, they cannot work without the presence of a reader, and because of the modulated response signal, they are sensitive to ambient noise and interference.

2.1.3 OPERATIONAL FREQUENCIES

The communication between tags and readers works in different frequency bands. Each frequency band achieves different performance, power requirements and operating distances.

International and national regulations define the ranges of power output to prevent interference. In addition, the frequency of RF signals determines which materials they can propagate. Tags working at Ultra-High Frequencies (UHF) and in the proximity of metallic materials and liquids do not function properly. Moreover, the size of the RFID tag is essential for shaping the antennas' size and operating frequency. There are three primary standards and used frequency bands, as shown in Tab.1:

Table 1 - Worldwide UHF band [24, 26]

Frequency Range	*Frequencies*	*Regions*	*Distance Reach (Passive RFID)*
LF – LOW FREQUENCY	125 - 134 kHz	EU, Canada, US, Japan	12-20 cm
HF – HIGH FREQUENCY	13.56 kHz	EU, Canada, US, Japan	12-20 cm
UHF – ULTRA HIGH FREQUENCY	865 - 868 MHz 902 - 928 MHz 952 - 954 MHz	Europe (EU) US Japan	3 m

2.1.4 APPLICATION

Active tags are used for high-value asset tracking applications and are attached to target objects, e.g., railway wagons and shipping containers, as they are of high value and have the space to attach a bulkier tag [28]. These tags can have additional functionalities beyond simple trackings, such as connecting a network of active tags or using an accelerometer rather than GPS or a temperature sensor for the cold chain [29]. One application of semi-passive tags is for electronic toll booths. They usually are attached to the inside of the car, and when it passes through the toll station, it will interrogate the semi-passive tag and read the tag's account identifier [25]. The battery, in this case,

improves the reading distance. However, since the tag only needs to transmit when interrogated, it can remain idle and save energy. Passive tags are used in a variety of applications to identify a product. One application is a proximity card commonly used to control access to buildings by checking entrances and exits, such as in subways and trams. In addition, several applications use RFID as an anti-counterfeiting device. One example is passport encryption, inserting a chip to get information about the holder and usage history. Some applications have led to a reduction in RFID operability. For example, operation in the proximity of metals or liquids is reduced [30]. Mounting or inserting an RFID tag on metal can be complex, as the metal surfaces reflect the electromagnetic waves of the readers. Metal surfaces can interfere with tag antennas, making it difficult to receive and re-transmit the signal. However, a category works in the proximity of (conductive) metal surfaces [31, 12]. They are called on-metal RFID tags, and they work mainly in UHF. They are used in the medical field to track goods and instruments in medical devices, industrial production such as oil and gas pipelines, and in-vehicle identification and tracking.

The inlay can be placed between two layers (Fig. 8a), one is the adhesive, and the other is a cover to form the classic RFID label. In a harsh environment (Fig.8b), the insert is integrated into the housing to make it more resistant.

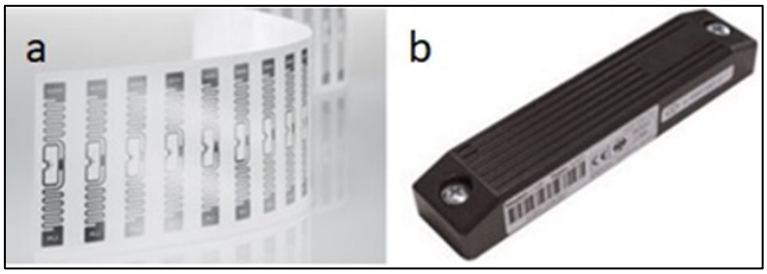

Figure 8 - RFID Label and RFID hard tags

Many On-Metal RFID tags are designed to withstand harsh conditions. They are usually encased in a hard shell to survive substantial impacts or high temperatures and pressures rather than aggressive paint. They are also called rugged. Hard tags can be attached to metal surfaces in various ways, such as welded, riveted, or bonded with industrial adhesives. On the other hand, some can be embedded inside metal elements before or after the metal component is manufactured, and the small size makes them attractive for tracking medical items or in other industries with small object tracking.

Therefore, each technology has its strengths and weaknesses, including size, cost, power requirements and environmental limitations. Therefore, different RFID technology can be used for each application to achieve the best combination and result. An example is an integration inside passports, inserting a chip to get information about the holder and the usage history.

2.1.5 STANDARD ISO AND EPCGLOBAL

RFID systems are considered a broader class of automatic identification (Auto-ID) in commercial applications. For the technology to succeed, tags and readers must communicate via specific protocols without interfering with other radio frequency services. The two most relevant standards for UHF RFID technology are ISO/IEC 18000-6 and the protocols given by the EPCglobal standard Class 1- Generation 2 [22, 26]. As shown in Fig.9, these standards do not conflict but can be adopted simultaneously. EPCglobal defines specifications for tag operation.

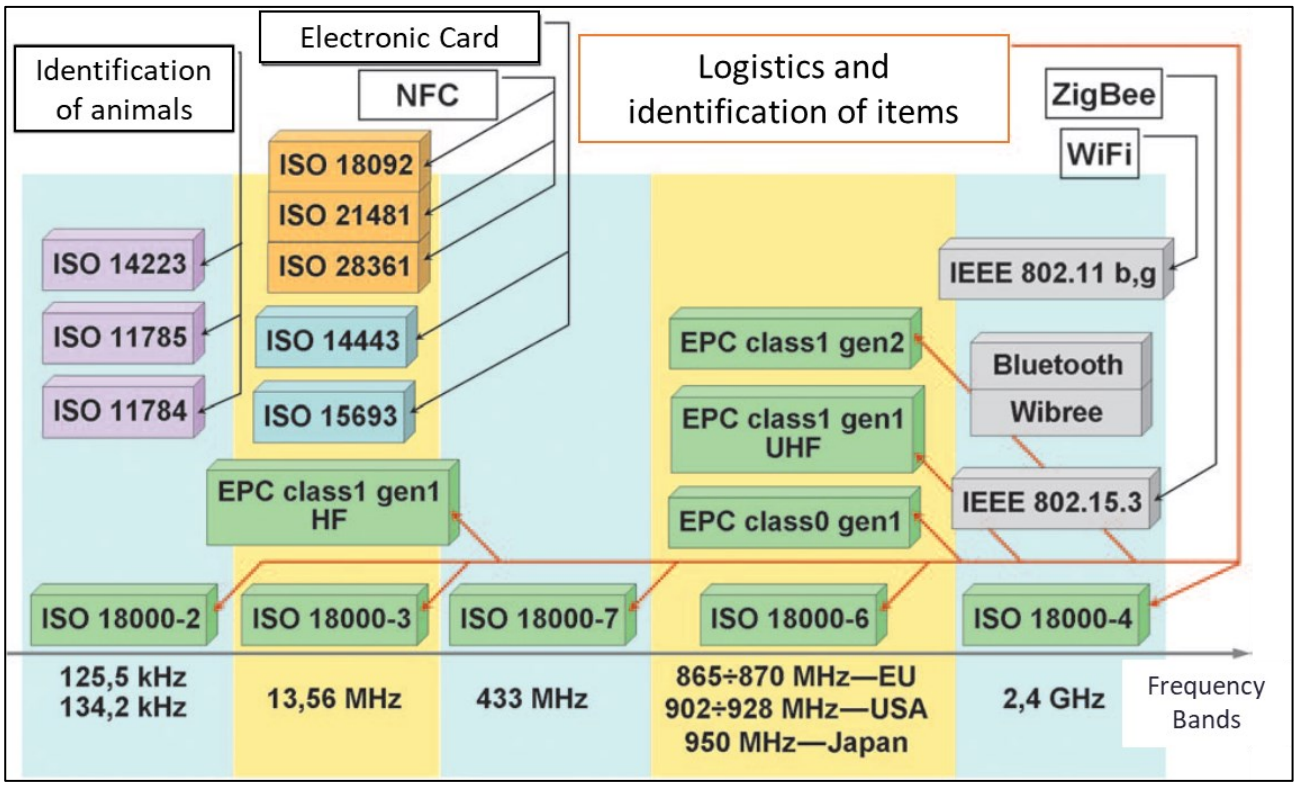

Figure 9 - Standard, Frequencies bands and Applications [22]

2.2 SMART TRACKING USING RFID

The specific steps in the research to achieve our goal will be defined. The configurations, which will be better explained in the following chapters, and the passive tag, allowed us to understand which configuration either amplifies, attenuates, or eliminates the reading distance up to the threshold of 1.5 meters.

The actions and the equipment used to build, test, and evaluate the embedded RFID tags are outlined together with the methods used to collect and analyse the test data.

2.2.1 STEP AND METHODOLOGY TASK

Tab. 2 shows the various steps and methodology used to achieve our goal.

Table 2 - Step process

Set-up with RFID sensor after curing process that can be read without signal reduction at a given distance	
Step 1	Investigation of commercial RFIDs
Step 2	Suitability of RFID sensors for embedding into CFRPs
Step 3	Design and production CFRPs mock-ups
Step 4	Evaluation of the best configurations
Step 5	Embedding in the real configuration before the curing process
Step 6	Defining the best configuration

2.2.1.1 INVESTIGATION OF COMMERCIAL RFIDS

The first challenge was to find a commercial tag that could withstand composite pre-preg storage and curing temperatures and work on conductive surfaces. In particular, the latter requirement is met by the so-called RFID On-Metal tags. The chosen tags are part of the passive UHF (Ultra High Frequency) category and are very efficient in different applications. In order to work, they need to receive the signal and send it back in backscatter. The tags can be small and cheap yet perfect for tracking items that pass through the supply chain. In this case study, the choice fell on On-Metal passive UHF tags. This type of tag is often used in the automotive industry, where production and industrial environments are full of metal components, and in our case, CFRP.

The labels have been chosen according to the real scenario, considering the high temperatures (~150/160°C) reached in polymerization in an autoclave and the low temperatures (-18°C) in the cold

chamber where the composite rolls are stored. The pressure reached in the autoclave process around 2 bar is a second constraint. Moreover, the last constraint is the size.

Three On-Metal tags were chosen (Tab. 3, Fig.10) that satisfy the size and temperature range.

Figure 10 - RFID On-Metal tag a) Xerafy Dot On XS [32] ; Omni-ID a) Fit 220 HT [33], b) Fit 400 HT [34]

Table 3 - Properties of the tags

N tags	*Name Tags*	*Size [mm]*	*Operating temperature [°C]*	*Application temperature [°C]*
1	Fit 220 (Omni-ID®)	7.8*6.8*2.7	-40/ 85	-40 / 220
2	Fit 400 (Omni-ID®)	13.1*7.8*3.1	-40/ 85	-40 / 220
3	Dot On XS (Xerafy®)	Ø6*2.5	-40/ 85	-40 / 220

2.2.1.2 SUITABILITY OF RFID SENSORS FOR EMBEDDING INTO CFRPS

Once the sensor met these three critical criteria, the reading tests were evaluated with a mobile reader by placing the different tags on the materials of interest to understand their reading potential. To understand the potential of the tags from the market survey, they were tested on the following materials chosen according to availability and the company's needs, i.e., dry smooth weave carbon fibre (Fig.11a), aluminium foil (Fig.11b), brass foil (Fig.11c) and thick aluminium inserts (Fig.12). Each coupon was cut into a square shape of 150mm side. In terms of thickness, the aluminium foil is 0.1mm, and the brass foil is 0.2mm. The aluminum inserts were made with grooves where to house the RFID tag, with dimensions of 1, 2, 3 and 4 times the nominal size of the tag. The use of different dimensions has been decided to evaluate the emission of the electromagnetic signal of tags. The groove depth was kept constant and equal to the height of the tag. The performance evaluated the reading distance obtained along the axis perpendicular to the sheet and centred on the tag.

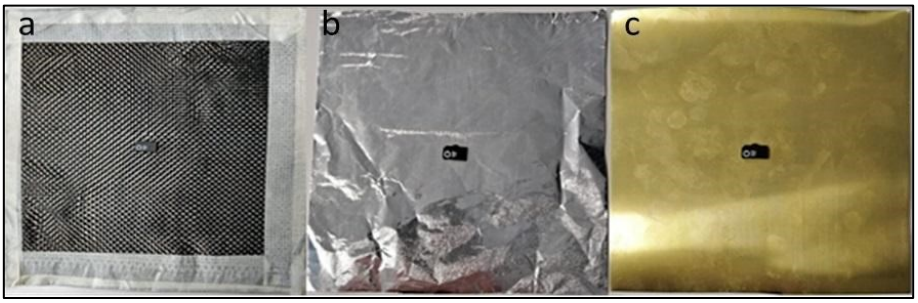

Figure 11 - Fit 400 HT (Omni-ID) on a) dry carbon fiber, b) aluminium, and c) brass foil

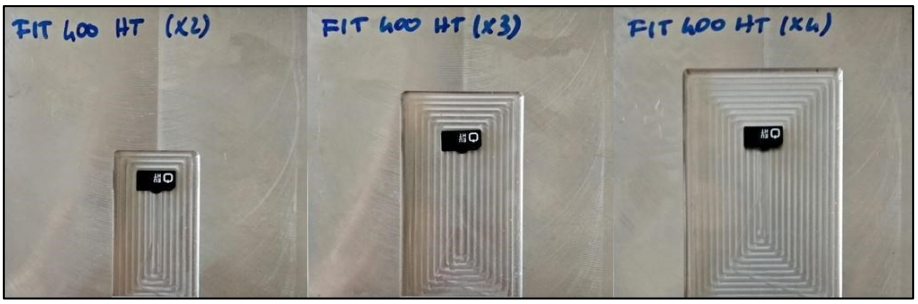

Figure 12 - Fit 400 HT (Omni-ID) on Metal insert

The results in Fig. 8 obtained in these experiments allowed us to understand the three tags' performance based on their reading distance. The Dot On XS tag showed the difficulty of detection even at short distances in any case, and it was discarded. Fig. 13 shows that the RFID tag Fit 220 HT gave acceptable reading distance in some cases and, therefore, it was considered for subsequent testing along with the tag Fit 400 HT, which was readable at the target reading distance of at least 1.5m.

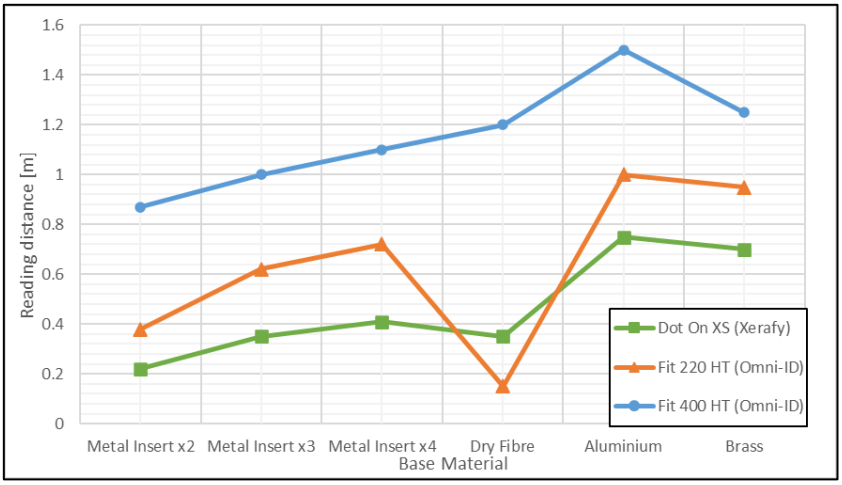

Figure 13 - Reading distance by reader mobile of the tags tested

2.2.1.3 DESIGN AND PRODUCTION OF CFRP MOCK-UPS

The methodology explained in the following two sections has been extrapolated from the reference article [21].

After selecting RFID tags, an experimental campaign with a preliminary test was performed to assess the reading distance under more realistic conditions.

The read distance test aimed to determine whether readers could read RFID tags after production. These tests help to understand the possibility of integrating RFID tags into the production of composite materials. The RFID tag embedded within the composite laminate was activated to determine how far the tag could be read. The purpose of these tests was to:

1. define the best configurations before embedding them prior to the production process,
2. realise the above and see if the production processes damage the RFID tag.

A full-factorial DoE (Design of Experiment) was established with two parameters (groove and cover size) on four levels (one combination without covering, eight combinations for non-shielding cover patches; six combinations for DCHP – die-cut hole pattern cover) for each tag, groove size and cover material, for a total of 360 tests. Not having data and studies on which to base ourselves, the full-factorial DoE allows us to understand better the interaction between the chosen dependent and independent variables concerning our outputs. Hence, it allows us to have an objective comparison of the reading obtained in the experimental phase with all the groove-cover combinations that will be proposed below.

That is, obtaining a database on which to operate and subsequently going on to study in detail and depth.

Specimens were designed and manufactured from CFRPs by making a groove to accommodate the designated tag. Three distinct shapes opted for each RFID tag.

The different groove geometries used are explained below for each tag. For the Fit 220 HT, the case studies are as follows (Fig. 14a-b):

- Square (S),
- Square chamfered (SC),
- Circular (CR).

While for the FIT 400 HT, the case studies are as follows (Fig. 14c-d):

- Rectangular (R),
- Rectangular chamfered (RC),
- Circular (CR).

The groove shapes described above are respectively 1, 2, 3, and 4 times the size of the tag, while the depth of the groove is equal to the thickness of the sensors (3 mm). The 4x size is the largest groove the company would allow on a CFRP component to affect its strength as little as possible.

The CFRPs bases were fabricated on an aluminium plate layering tool. The parts were manufactured using GG630 T700 12K 2x2 DT120 37%. The parts were made using eight layers in an $[0/90]_8$ orientation.

The bases are made up of several layers of CFRP already cut before lamination to obtain the final shape of the groove for the designated tag. After the lamination process, the vacuum bag was prepared with the samples, then cured in the autoclave: at 120 C and 2 bar for 120 minutes.

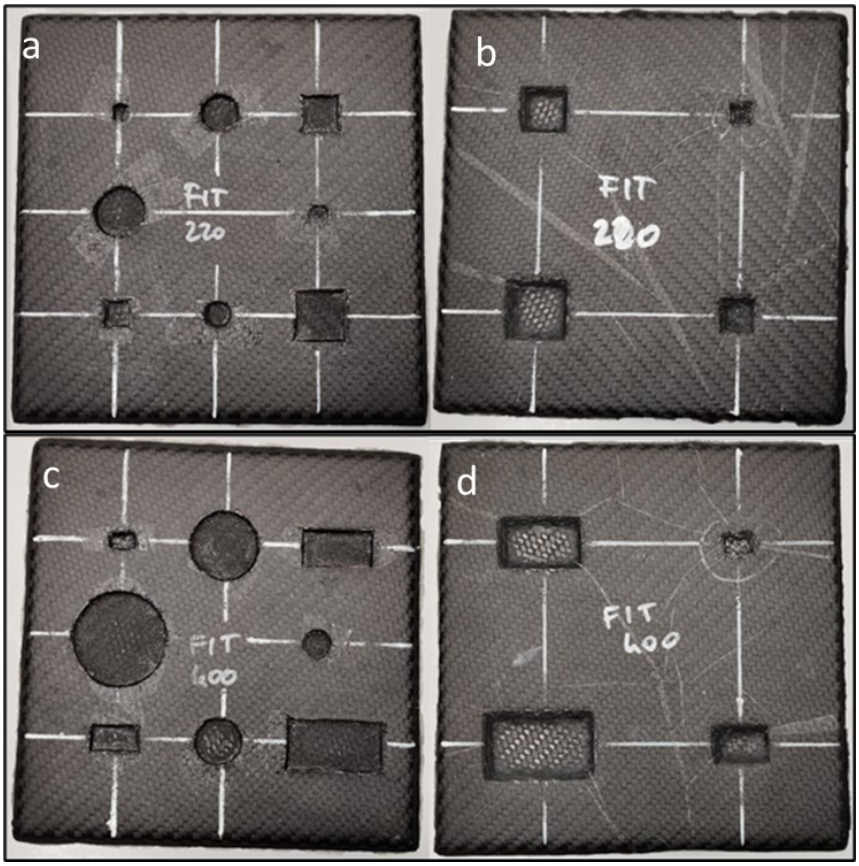

Figure 14 - Base of the tag Fit220HT a) Square and circular groove shape, b) Square chamfered groove shape, Base of the tag Fit400HT c) Square and circular groove shape, d) Square chamfered groove shape

Subsequently, the covers were made from different composite materials, which is a component that should hide the tag and protect it from the environment.

Since an overlay obtained with only CFRP would shield any signal, both incoming and outgoing, different solutions were considered based on the materials most used by the company.

This made it possible also to consider composite materials that do not shield electromagnetic waves. The chosen covers can be divided into two areas, shielding and non-shielding.

Shielding (Fig.15a-b):

- CFRP (C)
- Carbon – Kevlar (C/K)
- Carbon – Dyneema (C/D)

Non-shielding (Fig.16a-b):

- Fiberglass (FG)
- Kevlar (K)

The covers with the shielding material were made with a die-cut pattern in the centre of the cover, which leaves circular holes to pass radio waves. Since the minimum diameter of a DCHP was 5 mm, a pattern could only be made in the case of an area of 3 and 4 times the size of the plate,

respectively. In the case of non-shielding covers, patches were placed in a die-cut slot on a CFRP ply, creating a "window" for radio waves to and from the tag.

Depending on the tag used, the shape of the windows can be square or rectangular. The size is a multiple of the size of the tag, namely, 1, 2, 3 and 4 times.

The CFRPs parts were fabricated on an aluminium plate layering tool. The parts were manufactured using the following materials:

- Carbon fibre
- Carbon\Kevlar
- Carbon\Dyneema
- Kevlar
- Fibreglass

The shielding covers were laminated using three layers in $[0/90]_4$ orientations, using a single material each time. On the other hand, the non-shielding covers were laminated by placing two layers of non-shielding material, Kevlar and the other fibreglass, between 2 layers of CFRPs.

The shielding material layers were cut and die-cut and then laminated and cured in an autoclave to obtain the final form at the end of the process. The same applies to the carbon layers for the non-shielding covers, i.e., the central part is cut and then filled with the two plies of Kevlar or glass fibre.

Finally, after preparing the samples with the vacuum bag, they were cured in an autoclave: at 120°C and 2 bar for 120 minutes.

The samples described above have been designed to allow interchangeability between bases and coverages, reducing the number of samples produced. First, the tag to be tested was not cured within the sample. The tag was housed inside the grooves alternating from time to time for the covers to be tested and then moved to the next groove until the various configurations were exhausted.

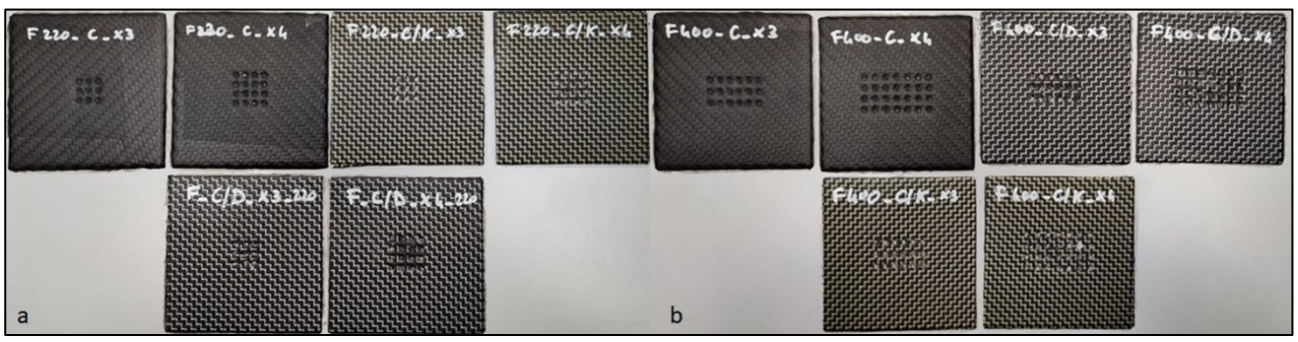

Figure 15 – Shielding covers of the a) tag Fit220HT, b) tag Fit400HT

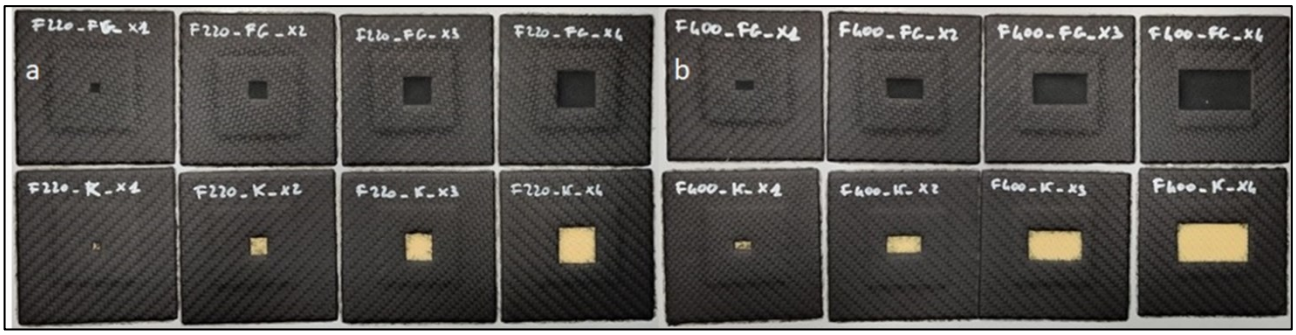

Figure 16 – Non-shielding covers of the a) tag Fit220HT, b) tag Fit400HT

2.2.1.4 EVALUATION OF THE BEST CONFIGURATIONS

At the beginning of the experimental campaign, a minimum threshold to be reached with the RFID read tests was defined.

The following picture shows that the experiments were carried out in two ways. In the tests with the mobile reader (Fig. 17), each sample was placed in a fixed position, and the distance of the mobile reader was varied until there was no more reading. Meanwhile, with the fixed antenna (Fig. 18), the tests were conducted by increasing the distance of the sample until there was no more reading. The procedure was repeated three times per configuration to obtain an average reading distance.

The preliminary experimental campaign was carried out in an industrial environment.

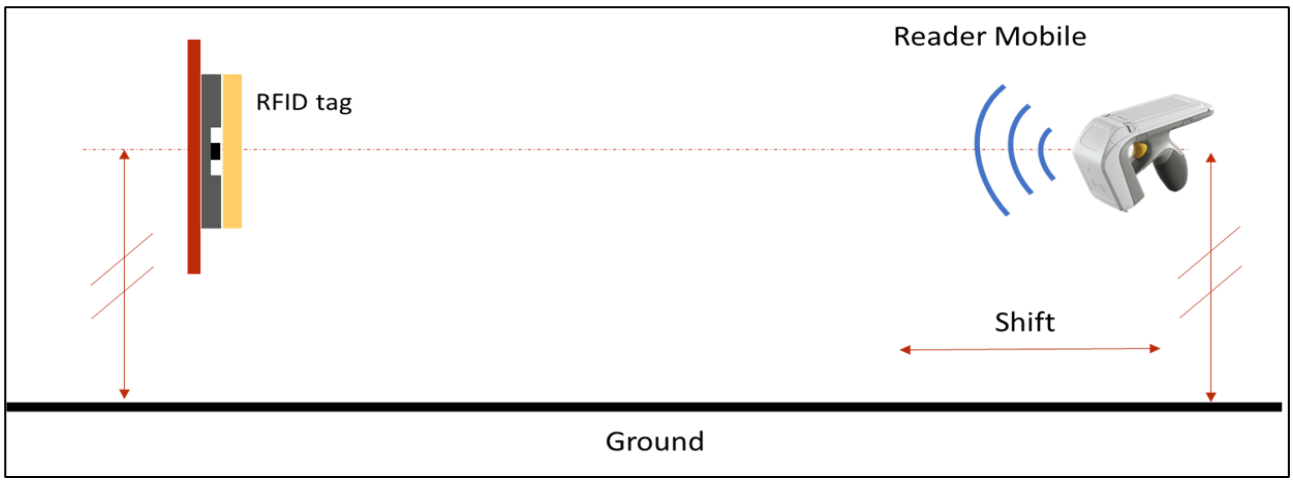

Figure 17 - Set up the mobile reader

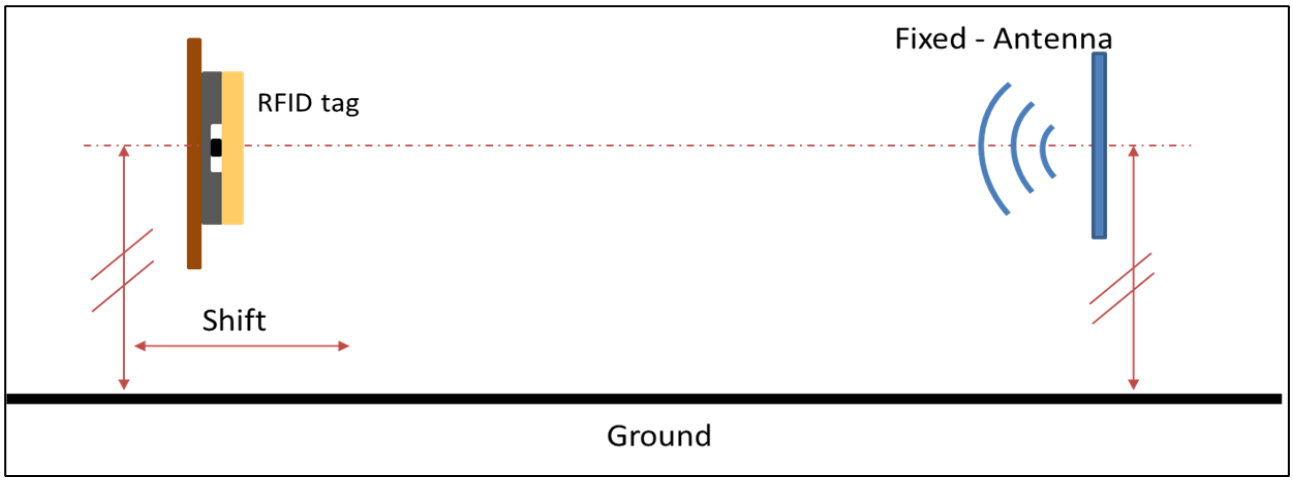

Figure 18 - Set up the fixed antenna

2.2.1.5 EMBEDDING IN THE REAL CONFIGURATION BEFORE THE CURING PROCESS

The second objective remains to determine, only for the best configurations, whether readers can read RFID tags after the autoclave curing process. These tests aimed to check if the reading distances previously obtained were confirmed. The new specimens were fabricated on a layering tool of aluminium plates. Each specimen was produced with the RFID tag embedded. They were produced following the lamination sequence of the previous specimens, but in this case, it was done in a single process, i.e., joining the base to the cover by placing the reference tag inside. Besides, in each sample, the RFID tag was placed into the groove with a Roachell®, a high-density foam used mainly in the composite structure in sandwich solutions and during the lamination process, and transparent to electromagnetic waves.

In this case, the samples were made individually with a square shape with a side of 105 mm.

The base of the samples is made of CFRP. There is a groove in the centre of the bases to house the reference tag. Then the tag is hidden by the cover made according to the reference configuration. The groove where the tag is housed has a depth equal to the thickness of the RFID tag chosen, which in this case remains constant and equal to 3mm, as explained in section 2.2.1.3. The samples were cured in an autoclave at 120°C and 2 bar for 120 minutes. In each sample, the RFID tag was placed into the groove with a Roachell®, a high-density foam used mainly in the composite structure in sandwich solutions and during the lamination process, and transparent to electromagnetic waves. The insert will be made according to the shape of the groove. The reading distance tests were carried out only with the fixed antenna, which is the most interesting case for the company. Likewise previous reading tests, the antenna was placed on fixed support and connected to the reader to record the readings obtained with the new samples (1st set-up). The tests were led with environmental conditions

like the uncured ones (as for problems due to covid-19, it was impossible to perform them in the industrial environment).

Therefore, the readings were evaluated in an environment with few metal elements. In addition, a cage was used to assess whether the presence of metallic materials in the noisy industrial environment affected the emission of the electromagnetic signal. The reading distance was estimated by rotating the sample 90 degrees from the nominal antenna (Fig. 19).

The cage is composed of two metal nets placed parallel to each other. The read-outs tests were evaluated by spacing the cage in 25, 37,5 and 50 cm steps from the antenna (Fig. 20 a-b-c). In addition

On top of that, further antenna configurations have been evaluated due to possible situations where a gate consisting of RFID antennas could be used. The antenna has been placed with an inclination of 45° relative to the ground (2nd set-up); it has been positioned at three different heights, i.e., 50, 100 and 150 cm from the ground (Fig 21-22). Similarly, the sample was rotated by 90 degrees, as in the previous case.

The procedure was repeated five times per configuration to obtain an average reading distance.

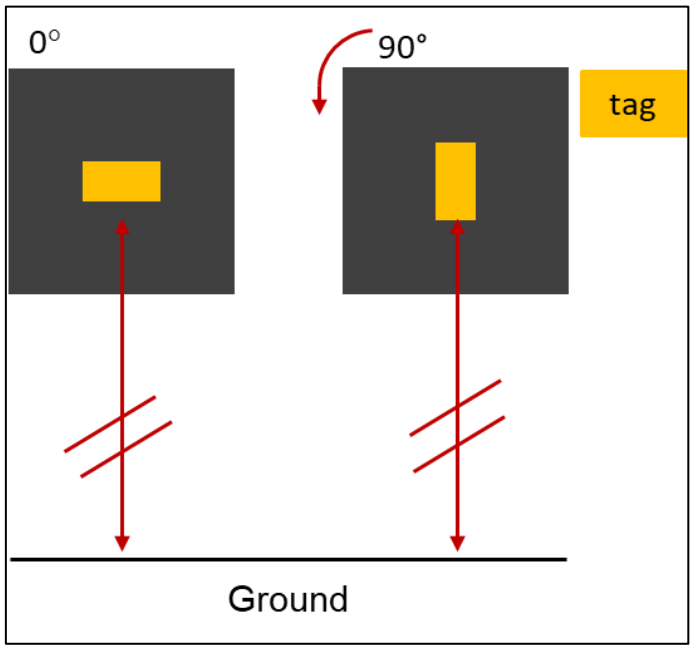

Figure 19 - Configurations for reading samples at 0° and 90°

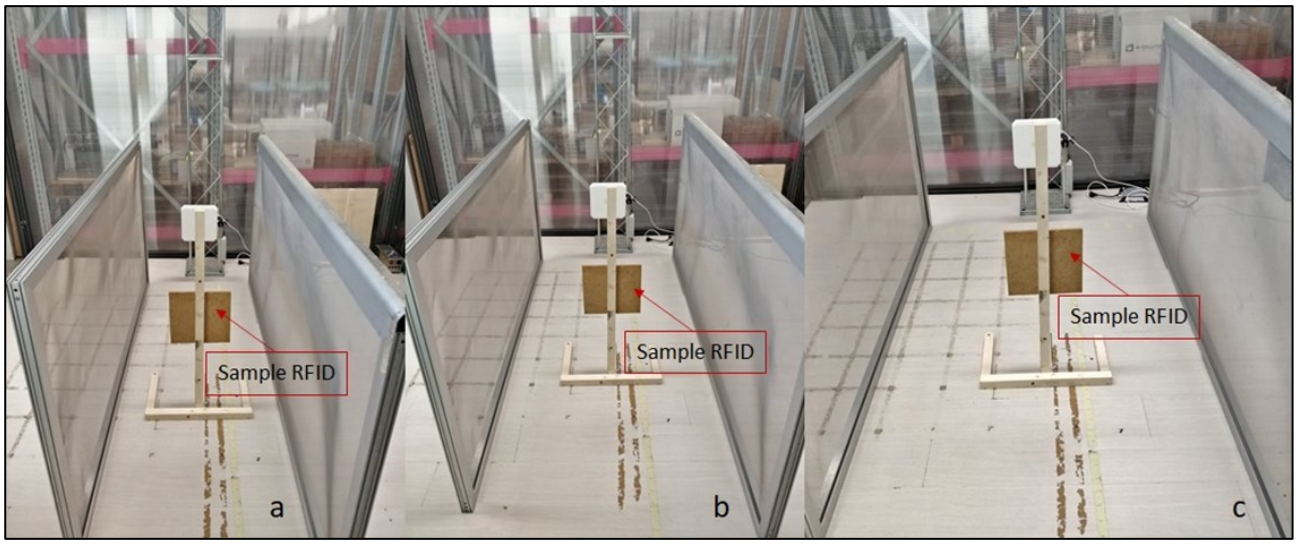

Figure 20 - 1st set-up fixed antenna with cage at different distance

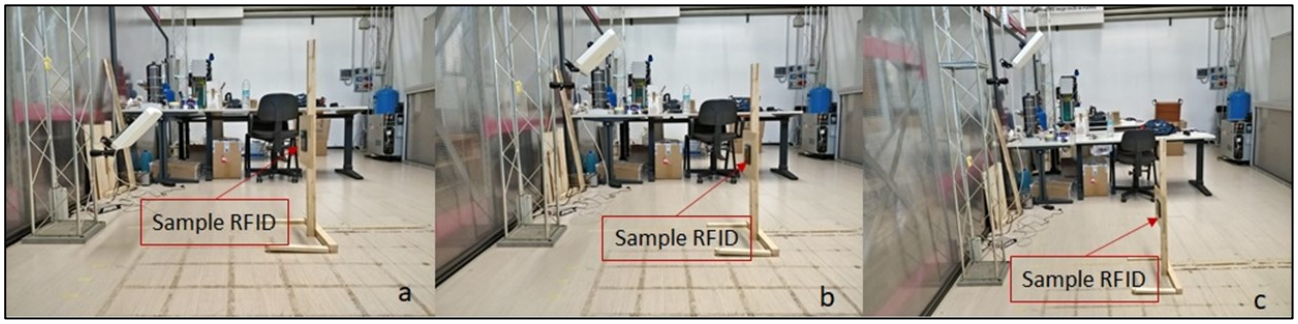

Figure 21 - 2nd set-up fixed antenna at 45° at different high

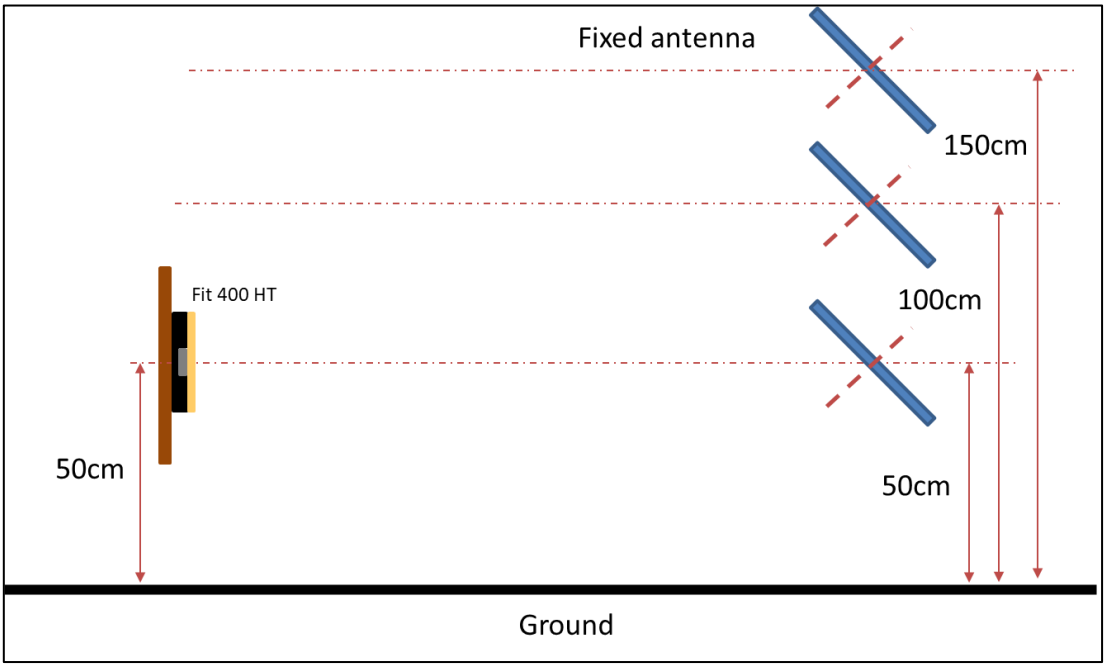

Figure 22 - Scheme 2nd set-up fixed antenna at 45° at different high

2.2.1.6 DEFINING THE BEST CONFIGURATION

Finally, after highlighting the best configuration, it was decided to evaluate a change in the shape of the Rohacell® insert. As in the previous case, the samples have a square shape with a side of 105 mm.

Similarly, the reading tests occur in the same ambient conditions and in the same fixed positions of the antenna indicated in point 2.2.1.5, allowing us to evaluate better the choices made on optimising the Roachell insert.

Compared to the previous samples, it was decided to smooth the sides of the insert Rohacell® to reduce the impact on the mechanical performance of the CFRPs.

The procedure was repeated five times per configuration to obtain an average reading distance.

2.3 RFID DETECTION EXPERIMENTS

2.3.1 LOCATION OF EXPERIMENT

All components produced for this part of the research were made in “Dallara Automobili”. The samples were made in the lamination department and then processed in an autoclave for curing. The tests for section 2.2.1.3 were carried out in the R&D laboratory of “Dallara Automobili”. The remaining tests, explained in sections 2.2.1.4 and 2.2.1.5, for Covid-19 cause were carried out within the laboratory of the University of Parma.

The samples were produced using an aluminium plate as a base to lay up the various layers, the vacuum pump, the composite materials and the autoclave.

The measurement systems used will be best explained in the following paragraph.

2.3.2 MEASUREMENT SYSTEM

The measuring systems used for the reading tests consist of two readers: one mobile and one fixed. The first is used as a sort of "electric gun" aesthetically like those used for bar codes, Fig.23a; the second in Fig.23b is often mounted on warehouse portals for access control or conveyor belts or shelves. In real industrial cases, the components can be in different ways. They can be read by the individual operator or with fixed antennas. In the first case, the operator can read at the beginning of the end of the process, for example, the rolling or finishing phase. In the second case, fixed antennas

can be arranged by forming a gate, allowing reading more products as they pass, for example, at the reception of rolls of material or during the transport of more components from the curing phase to the finishing area. It was chosen to use both RFID readers in the first instance, but the most interesting case is the readings obtained with the fixed antenna.

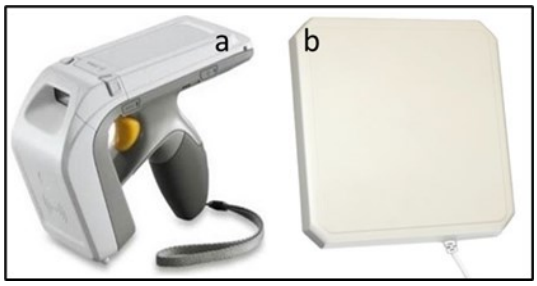

Figure 23 -a) Mobile reader Zebra RFD 8500 [35], Far-Field RFID Laird® Technologies S8658PL antenna [36]

Fig.23a shows the mobile reader RFD8500 from Zebra brands. It can be paired with a compatible third-party mobile device, such as a tablet or smartphone; it is used when and where ease of use and cost-effectiveness are required.

On the other hand, The Laird® Technologies S8658PL antenna (Fig. 23b) is a circularly polarized panel antenna that receives and transmits signals in the 865-870 MHz frequency band (EU frequency band). The fixed antenna is used to form gates to cross with objects associated with RFID. The reader completes the measuring system [37] with two antenna ports, communicating via PC to the software Multireader Gen2 RFID Utility® to record the readings (Fig.24).

Figure 24 - Reader Impinj® Speedway 220 [37] and Multireader Gen2 RFID Utility® and database reading distance on Excel®

2.4 RESULT AND DISCUSSION ON SMART TRACKING USING RFID

The ANOVA study on the best configurations has been included to understand the results' analysis better.

2.4.1 READING DISTANCE TEST OF UN-CURED RFID TAGS

After completing and acquiring all the reading distances with the 360 configurations obtained with the mock-up described in section 2.2.1.3, the analysis was carried out using ANOVA (ANalysis Of VAriance) and RSM (Response Surface Methodology).

Following careful analysis, the two best cases chosen from the experimental campaign of un-cured tags will be explained in more detail. One case was chosen for each tag.

In order to make the best use of the two-way ANOVA methodology, more values were collected for the reading distances (quantitative dependent variable) than for the different combinations (or levels) corresponding to two categorical independent variables (slot and coverage size). ANOVA with replication requires more than one observation (reading distance). Multiple values were collected from each combination of independent variables. The analysis was then subdivided and thus simplified according to the coverage used for each RFID tag

ANOVA is a hypothesis test used to assess the difference between the means of the groups. The model uses the sample data to infer the characteristics of the entire population. Each category divides the observations of the dependent variable into groups for each combination of the categories. The quantitative metric should be one for which measurements can be taken, and an average calculated. The obtained measurements (reading distance) are sufficient to calculate the mean for each combination of levels in the category specification.

The Analysis of Variance technique relies on an F-test to test statistical significance. A "test F" is a catch-all term for any test that uses the F distribution. In most cases, when people talk about the F-Test, they refer to the F-Test to Compare Two Variances. However, the f statistic is also used for the ANOVA test.

If the variance within the groups is smaller than the overall variance, the F-value will be higher, which means that the observed difference is most likely authentic and not due to chance.

The impact on the possible relationship between the dependent variable and the other independent variables indicates the interaction effect.

Based on this theory, the ANOVA test with interaction was evaluated. So, with a model with interaction, the following null hypothesis was tested (H0):

1. No difference in the group averages at any levels of the first independent variable (cover),
2. No difference in the group averages at any levels of the second independent variable (groove size),
3. The impact of one independent variable does not affect the impact of the other independent variable.

The data obtained from the reading test were first formatted correctly by dividing the categorical values into the cover and groove sizes and the dependent variable, the reading distance. Three reading values were obtained for each group consisting of all combinations of factor levels. α is "Significance level", and it was kept at 0,05. The data were collected in a matrix with one factor on the rows (cover) and the other on the columns (groove size).

Moreover, it is always possible to graph the averages of the data obtained so that the results obtained with the Anova, especially the two-way Anova, can be better understood. Fig. 25 shows the possible effects obtained when analysing the data. Concerning our case study, the abscissa shows the change in groove size, while the ordinate shows the reading distance obtained with the respective groove. Based on this, the trends of the respective averages referring to the different covers studied and compared can show various effects. The effects can be divided according to the first or second independent variable or the interaction between them, rather than no significant effect is noted.

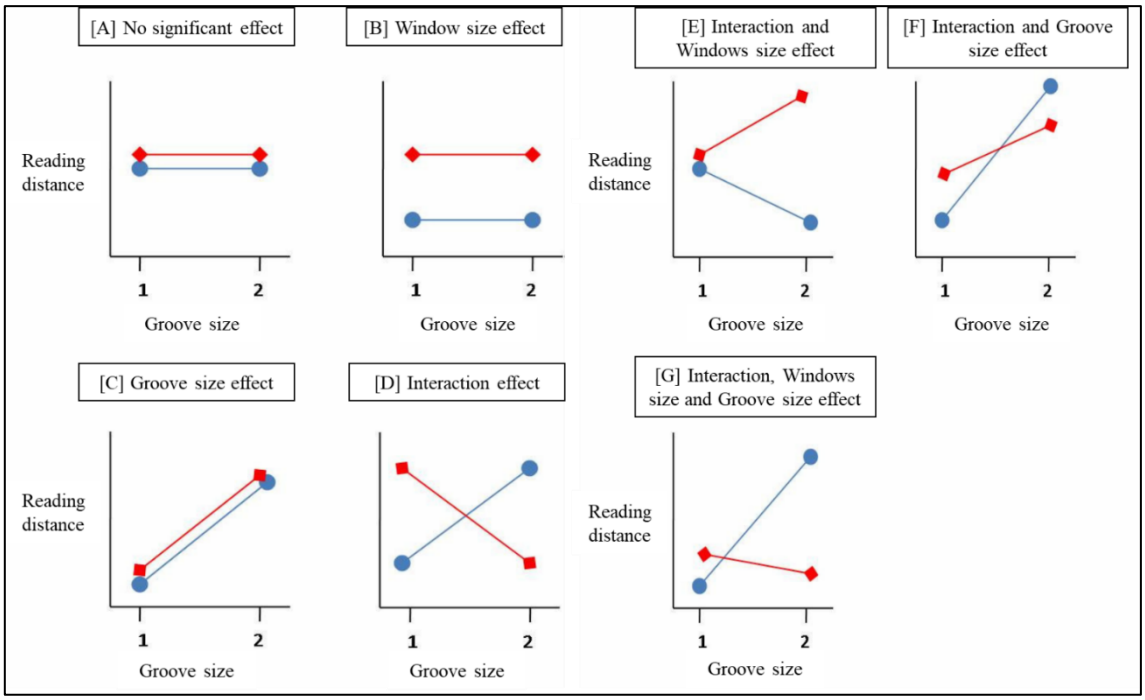

Figure 25 - Possible effects of observed mean values

The two-configuration shown in more detail below are case-related:

1. Fit 220 HT tag with square chamfered groove and DCHP shielding material
2. Fit 400 HT tag with a circular groove with Kevlar groove.

Table 3 - Analysis of Variance of case Fit220HT with DCHP cover

Origin of the variance	*SS*	*GOF*	*MS*	*F*	*p-value*	*F crit*
Cover	2.011528	5	0.402306	6.373157	0.00012968	2.408514
Groove Size	8.505278	3	2.835093	44.91236	5.65062E-14	2.798061
Interaction	1.384306	15	0.092287	1.461973	0.158291137	1.880175
In	3.03	48	0.063125			
Total	14.93111	71				

Tab.3 shows the ANOVA analysis for the first case, which refers to the Fit 220 HT tag. It allows us to evaluate whether the independent variable "Cover" statistically affects the dependent variable "reading distance". The p-value for this factor is less than 0.05. For this reason, this factor was statistically significant. In other words, a substantial difference in the reading distance between the type of cover can be observed. By assessing the "groove size", we define whether it impacts the values obtained. Again, the p-value for this factor is less than 0,05. Therefore, this factor was statistically significant too. In other words, a substantial difference in the reading distance between the groove size can be observed.

Finally, the last F-test refers to the interaction. In this case, the p-value is 0,15829, which means the result is not statistically significant. There is no significant interaction between the cover and groove size.

In conclusion, it can be possible that the cover and the groove size impact the variable dependent on the reading distance. Therefore, we expect the group of cover and groove sizes to differ. Nevertheless, from Fig.26, it is possible to notice that the non-interaction between the two independent factors is not present.

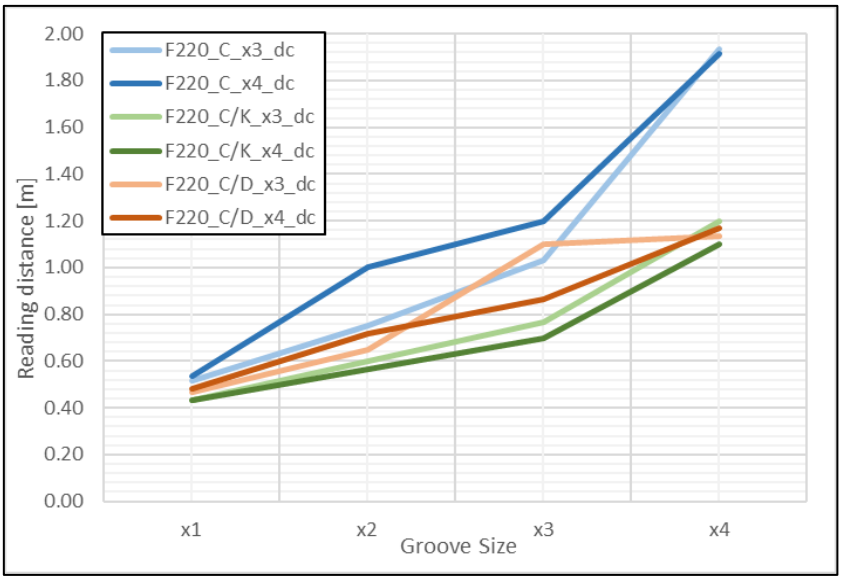

Figure 26 - Mean values observed of Fit 220 HT

Now the second case study refers to the RFID tag Fit 400 HT.

Table 4 - Analysis of Variance of case Fit 400 HT with Kevlar cover

Origin of the variance	*SS*	*GOF*	*MS*	*F*	*p-value*	*F crit*
Cover	2.350417	3	0.783472	9.040064	0.000175497	2.90112
Groove Size	6.167917	3	2.055972	23.72276	2.85204E-08	2.90112
Interaction	2.1025	9	0.233611	2.695513	0.018623095	2.188766
In	2.773333	32	0.086667			
Total	13.39417	47				

Tab.4 shows the ANOVA analysis for the first case, which refers to the Fit 400 HT tag. Starting with assessing the independent variable 'coverage', it statistically affects the dependent variable “reading distance”. The p-value for this factor is less than 0.05. For this reason, this factor was statistically significant. In other words, a substantial difference in the reading distance between the type of cover can be observed. By assessing the “groove size”, we define whether it impacts the values obtained. Again, the p-value for this factor is less than 0,05. Therefore, this factor was

statistically significant too. In other words, a substantial difference in the reading distance between the groove size can be observed.

Finally, the last F-test refers to the interaction. In this case, the p-value is less than 0,05, which means there is significant interaction between the cover and groove size. In conclusion, it can be possible that the cover and the groove size impact the variable dependent on the reading distance. Therefore, both cover and groove size groups differ and interact between the various groups. Nevertheless, from Fig. 27, it is possible to notice that the two independent factors are present.

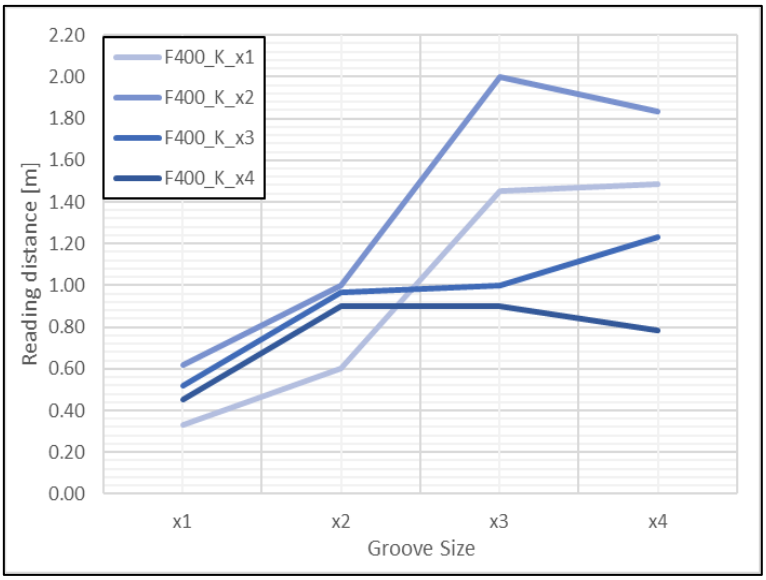

Figure 27 - Mean values observed of Fit 400 HT

The RSM analysis was also implemented to understand better the data extrapolated from the previous analysis. The analysis of the RSM allowed defining which cases to study in more detail. The surface response made it possible to define which configuration allows the RFID tag signal to be amplified when hidden by a cover. The RSM analysis for each tag was performed with the Matlab® tool "Curve Fitting Toolbox (Cftool)". The response surface has been modelled as a third-degree polynomial, least-square fit of the reading distance as a function of the groove size and the cover size for a given groove shape and cover material. In the case of DCHP covers, all three tested materials were collected in a unique response surface to reduce the number of analyses, given that only two cover sizes have been tested in this case for each material.

As explained in section 2.2.1.4, a threshold has been set to assess whether one or more configurations are ideally enforceable for tracking and monitoring assets made with CFRP. To visualize which value falls above the threshold value of 1.5m, we noted in Fig. 28-29 an additional red flat surface representing our minimum limit over the entire domain.

Two cases exceeding the threshold reading distance imposed on a substantial part of the domain are represented by:

1. Fit 220 HT tag with DCHP and square chamfered groove, cover Cx3 and grove x4 (Fig. 28),
2. Fit 400 HT tag with Kevlar and circular groove, Kx2 and groove x4 (Fig. 29).

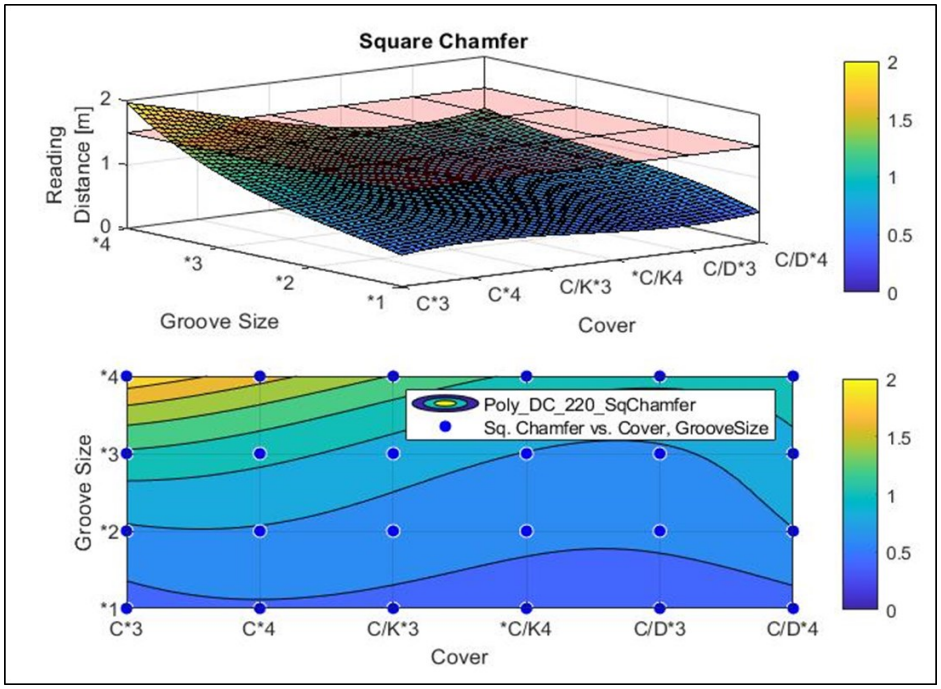

Figure 28 - a) RSM of Fit 220 HT with a square chamfer and DCHP cover, b) Contour plot [21]

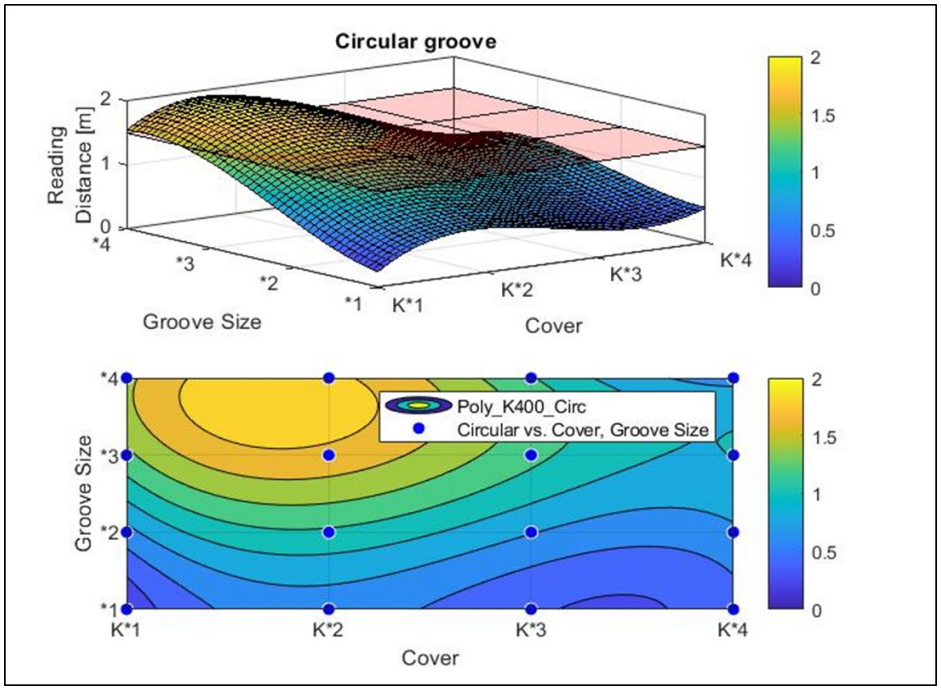

Figure 29 - a) RSM of Fit 400 HT with a circular groove and Kevlar cover, b) Contour plot [21]

In both cases, there is an improvement in the reading distance as the size of the groove increases. In Fig.28, the value of the reading distance exceeds the threshold and is restricted around the Cx3 - x4 groove size, with the peak located at the domain corner. The contour plot shows that the reduction factor is the groove size, which gradually decreases and leads to a decrease in the value obtained. Instead, Fig.29 shows the RSM for the Fit 400 HT tag. The value exceeds the threshold over a sub-domain ranging from cover size x1 to x2 and groove size x3 to x4, with a maximum reading distance close to x2-coverage - x4-groove. Furthermore, from the contour plot, it can be seen that increasing the kevlar groove size led to a significant reduction in signal. So, it was possible to notice an attenuation of the signal in the remaining configurations, i.e., far from our reading threshold.

2.4.2 READING DISTANCE TEST OF CURED RFID TAGS

After defining the first experimental test campaign, the best configurations with the uncured tag, as explained in section 2.2.1.5, the RFID tag has been integrated inside each sample before the lamination phase.

The new case studies can be summarised as follows:

- Fit 400 HT with Kevlar (K) coverage and circular groove, cover K*1.5 and CR*3 (Fig 21a)
- Fit 400 HT with Kevlar (K) coverage and circular groove, cover K*2 and CR*3 (Fig 21b)
- Fit 400 HT with Kevlar (K) coverage and circular groove, cover K*1.5 and CR*4 (Fig 21c)
- Fit 400 HT with Kevlar (K) coverage and circular groove, cover K*2 and CR*4 (Fig 21d)
- Fit 220 HT with die-cut hole pattern (DCHP) and square chamfer groove, C cover DCHP*3 SC*4 (Fig. 21e)

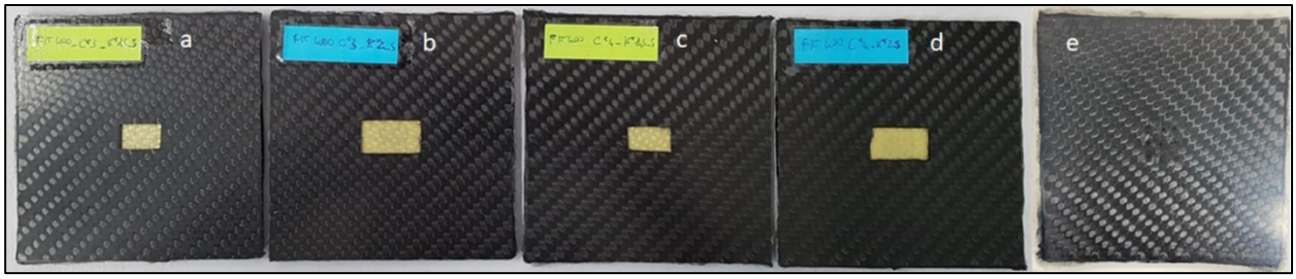

*Figure 30 - Sample with embedded sensor: a) Fit400HT K*1,5_C*3, b) Fit400HT K*2_C*3, c) Fit400HT K*1,5_C*4, d) Fit400HT K*2_C*4, e) Fit220HT DCHP*3_SC*4*

After analysing the data from the first set-up, which helps compare the previously obtained data with the untreated tag samples, it was immediately apparent that the sample containing the Fit 220 HT tag with DCHP coverage was not read. The holes in the die-cut were not perfectly cut, so some fibres fell in during the curing process. The not-perfect trimming of the fibres has potentially caused an additional shielding of electromagnetic waves and has not allowed the activation of the tag below. For this reason, the graphs shown from now on will only refer to the tag Fit 400 HT with the fixed antenna.

Fig.22a-b shows the trend of the readings obtained with the Fit 400 HT tag at 0° and rotated by 90° for the first antenna set-up.

To better evaluate the results obtained, two red lines have been inserted in the same graphs to indicate the base readings obtained with the same tag in the uncured configurations with 3x groove (circular marker) and 4x groove (triangular marker) in nominal position (0°) as explained in the section 2.2.1.3. The readings obtained in the nominal position gave comparable results to the readings of the uncured tag with the cage in the closest position to the antenna. As the presence of metal elements in the environment around the system is reduced, i.e., as the cage is moved further away, there is a significant decrease in the reading distance (Fig.31a). Similarly, the data obtained with the sensor rotated by 90° were compared with the readings of the untreated samples. The samples with the Kevlar x2 window with both grooves (Fig.31b) exceed the baseline reading distance when the cage is 25 and 37.5 cm from the antenna. The rotation of the tag-antenna system and metallic elements in the environment can improve the obtained reading. An opposite trend is observed with the x1.5 window configuration compared to that recorded with the antenna at 0° and the cage in the same position (Fig.31b). At more considerable distances of the metal cage, the reduced trend of the reading distance decreases as in the other cases.

Fig. 32 and Fig.33 show the reading distances obtained with the 2nd antenna set-up. Fig. 32 shows the nominal condition of our sample, i.e., at 0°, while in Fig. 33, the sample is tested rotated by 90°. The reduction of the reading distance obtained in the samples with window x1.5 is related to the antenna height increase. The tag is only read with the antenna 50 cm above the ground, reducing reading distance. This variation leads to the point where no reading is obtained. It is possible that the RFID tag is activated but has problems re-emitting the signal and communicating with the antenna. In the steps where the antenna is positioned 100 and 150 cm above the ground, only the readings of the samples with the kevlar window x2 are collected. Furthermore, with the readings obtained with the tag rotated by 90°, better reading distances are obtained than in the nominal case, with the cage at 25 cm from the antenna.

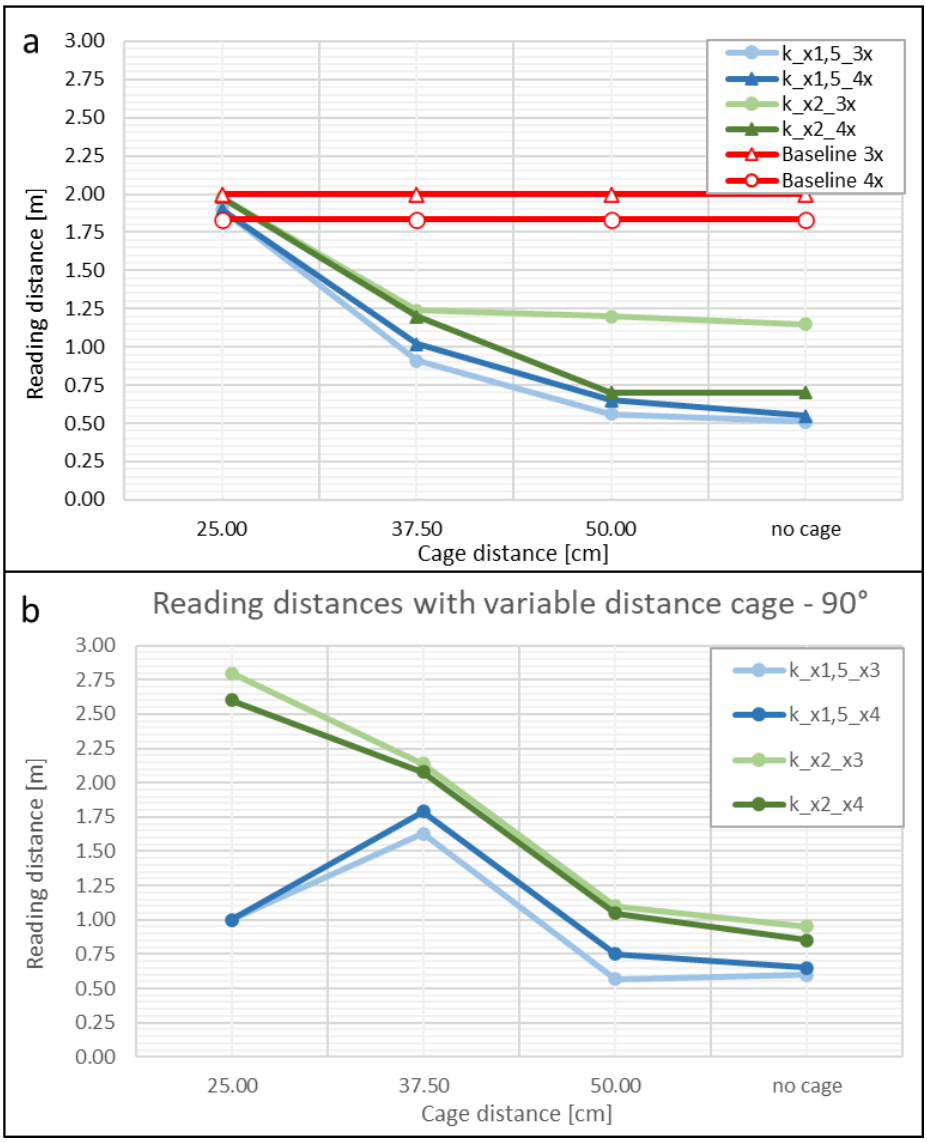

Figure 31 - Reading distance with 1st setup antenna a) 0° indicate the nominal position of the sample, b) 90° a rotation around the tag axis.

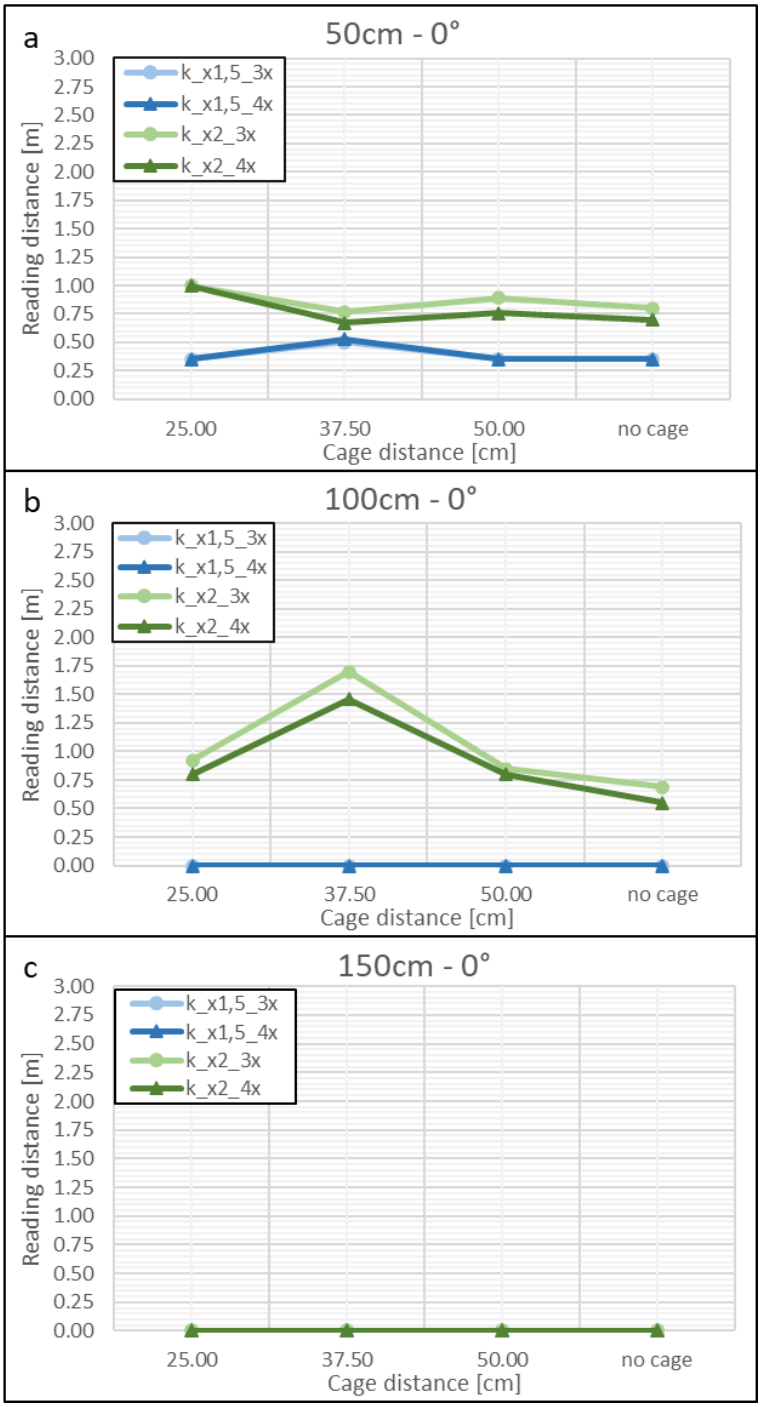

Figure 32 - Reading distance with 2nd setup antenna axis incident to the ground at 45°and sample 0°: a) 50cm, b) 100cm and c) 150cm from the ground

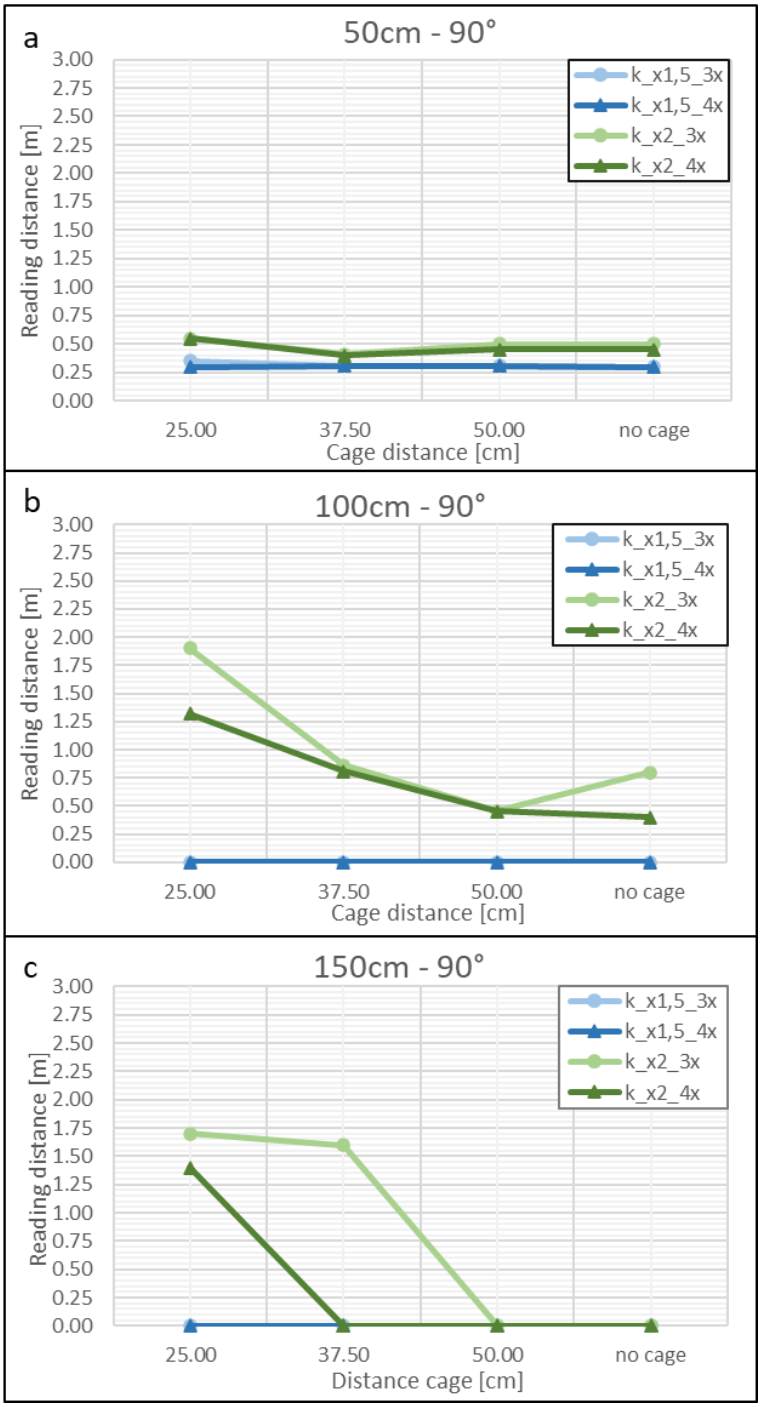

Figure 33 - Reading distance with 2nd setup antenna axis incident to the ground at 45°and sample 90°: a) 50cm, b) 100cm, and c) 150cm from the ground

Consequently, noting the better results just described and obtained with both antenna set-ups, it was decided to investigate further, starting with the sample with K_x2 window and with x3 groove.

The samples shown in Fig.34 a-b were made by fabricating two different shapes of the Rohacell insert from the set-up:

- Fit 400 Kevlar (K) x2 and circular hollow (CR) x3.

The first in Fig.34a mimics the circular insert (CR), while the other in Fig.34b conforms to the rectangular Kevlar window (R).

The same groove of the best configuration was maintained in the first specimen. Whereas in the second, the groove was reduced to a rectangular one.

Thus, both the Kevlar x2 window and the maximum sample size with a square shape of 105mm side were maintained for both samples.

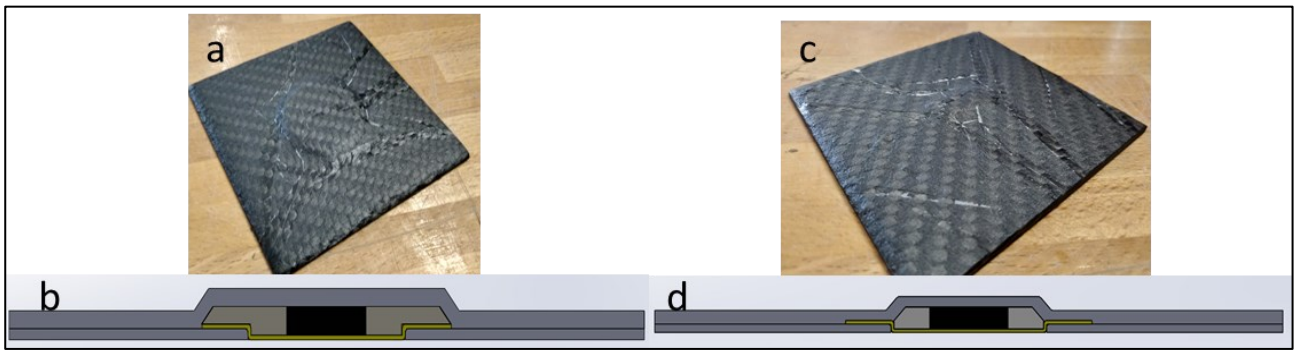

Figure 34 - Coupon with Circular insert a) Backside of the coupon, b) Section of the coupon; Coupon with Rectangular insert a) Backside of the coupon, b) Section of coupon

In addition, a change was made for both cases, namely, to chamfer the sides of the Rohacell®, chosen to reduce the impact on the mechanical behaviour of the CFRP compared to previous inserts with sharp edges (90° angles).

The new samples were tested for the abovementioned tests in section 2.2.1.5, using the antenna with both sets-up described. The following Fig.35-36 have two red lines that, as in the previous case, indicate our reading reference line, referring to the sample K_x2 CR_x3. The circular marker shows the sample readings in the nominal position (0°), whereas the triangular marker indicates the sample rotated by 90°. Fig.35 shows the readings obtained with the antenna of the first set-up, while Fig. 36 shows the readings obtained with the second set-up of the optimized samples.

Both configurations with the optimised insert give better values than in the base case.

The first antenna configuration led to a significant gain in the readings, especially with the samples positioned at 0° and the cage away from the antenna, i.e., at 50cm. On the other hand, with the sample rotated 90°, the constant gain is present as the cage distance varies.

In many cases, the trend is similar but with a significant gain in the distance obtained.

Fig.36 shows the readings achieved with the antenna in the second set-up. As in Fig.35, the highest measurement is reached with the cage at 50 cm.

The samples were tested with the second antenna set-up in the remaining cases (Fig.36a-b-c). As in the case of Fig.36a, the longest distance is reached with a cage at 50cm. Without a cage, there

is a significant decrease in reading. So, we can say that in the cases observed so far, the presence of metallic elements near the antenna can improve the reading obtained.

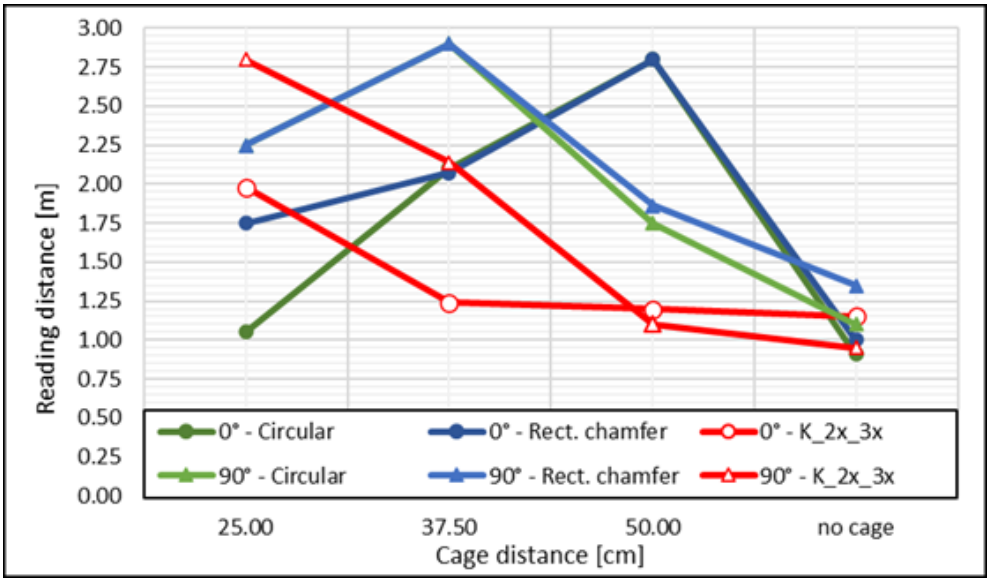

Figure 35 - Reading distance with 1st set-up antenna of the optimised samples 50cm

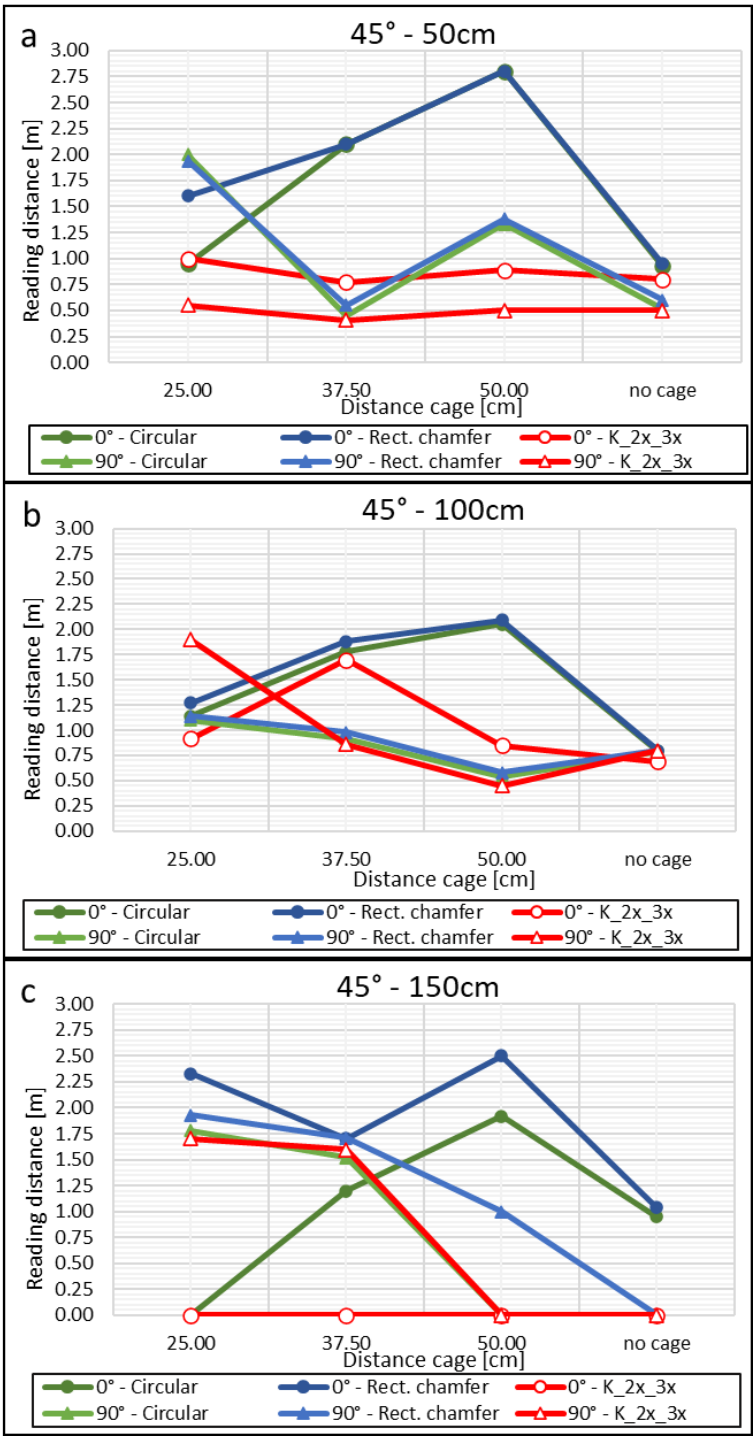

Figure 36 -Reading distance with 2nd set-up antenna of the optimize samples a) 50cm, b) 100cm c) 150cm

In chapter 3, the mechanical test with the help of the SHM tool will be discussed to evaluate the laminate strength better, considering the possible mechanical problems deriving from this discontinuity of the material inherent in the specimen with the optimised configuration that mimics the circular groove, but with chamfered sides.

Therefore, through the design of specimens and an experimental campaign of mechanical tests, it will be possible to better evaluate the effects due to the insertion of the tag in the CFRPs laminate.

3 EFFECT OF RFID ON COMPOSITE STRENGTH

In this section, the second macro-area of interest of this research will be dealt with, i.e., the evaluation of the impact on the mechanical properties of the composite structure using the final configuration chosen in the previous chapter.

Firstly, the FEM modelling tool designed the specimen and predicted the stresses.

The mechanical tests were carried out in the Faculty of Aerospace Engineering facilities at TU Delft, specifically in the Structures & Materials Laboratory.

In the background section, the state-of-art instrumentation used, such as Digital Image Correlation (DIC), C-Scan, Acoustic Emission (AE) and Microscope and Image system.

Subsequently, the methodology, the design in the FEM environment, and the set-ups used for static and quasi-static tests (or interrupted) will be explained and concluded with the results and discussions concerning the data obtained from the mechanical tests.

3.1 BACKGROUND OF TEST MONITORING TECHNOLOGIES

3.1.1 DIC

The birth of the DIC - Digital Image Correlation technique can be traced back to the early 1980s. It is still used to measure geometry, displacement and strain in both a material and a structure [38, 39].

The primary purpose of using DIC is to measure displacements and local strain of the sample's surface during the test. This is done by cameras that track a speckle pattern on the surface. The speckle pattern is sprayed on the surface of the laminates and used for DIC calculation. A dual-camera system (Fig.37) is often used that is calibrated so that they act as a set of "eyes" and can "see" absolute dimension and displacement in X, Y and Z directions as well as strains in X and Y directions. As shown in Fig.37, it is often best to use an angle of 30 degrees between the cameras, recommended by the manufacturer as a starting point for a good combination of in-plane and out-of-plane measurement accuracy. Because of the out-of-plane capability, curved surfaces or other complex shapes can be measured.

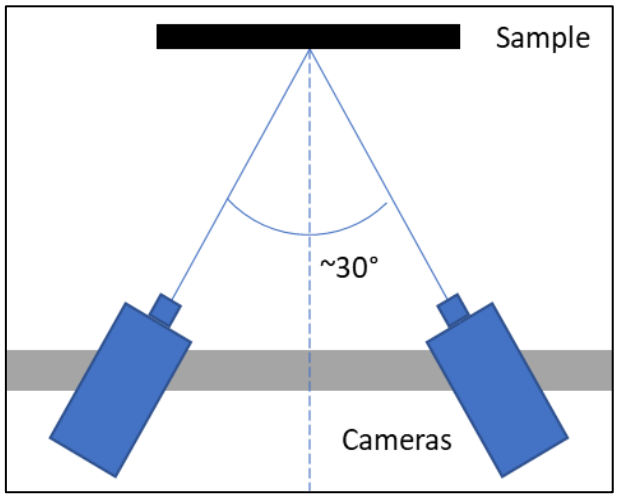

Figure 37 - Set-up DIC camera system

Depending on the speckle requirements, the speckle pattern can be applied in various ways. The most common way to apply the speckle pattern is to use a matte black spray can. This method is typically used for a wide range of specimen sizes.

3.1.1.1 SET-UP SYSTEM

As shown in Fig 38a-b, the DIC system is composed of the DIC car, the tripod where the aluminium profile housing the cameras (Fig. 38a) and the light source is placed on the top (Fig.38b).

Figure 38 - a) DIC camera car (3D), b) light source

Before starting any tests, it is necessary to calibrate the DIC system if a stereo (3D) configuration is used. The calibration process aims to take the image of a calibration grid in various orientations, including tilting the grid forward, backwards and rotating.

Fig. 39 shows the grid used for calibration. Because the rigid calibration grid, these images can perform shape measurements of the grid and determine the camera models and system parameters.

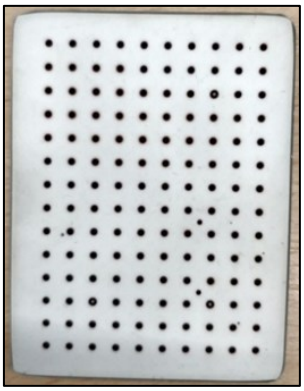

Figure 39 – Calibration panel

3.1.1.2 APPLICATION

The DIC technique has been used in many fields, but in the literature, many studies are focused on the aerospace sector to evaluate displacements and deformations in structures or samples subjected to static loads. Usually, the use of DIC is associated with well-defined tests and small sample sizes. With the improvement of digital imaging and data-analysis techniques, the use of this technology has also increased. It is mainly used to evaluate the field-of-strain developed during tests both in uniaxial tests [40] and for two-dimensional strain [41] and to evaluate the crack evolution [42]. Recently, it has been increasingly used in large-scale composite applications, such as wind turbines [43].

3.1.2 C-SCAN

Composite materials can be produced differently, combining a matrix and fibres. In cases where dry fibre is used, the matrix, i.e., resin, is added before or during the curing phase (resin-infusion). In applications where high quality and strength are required, curing is done by applying pressure and temperature at the correct time during the curing cycle. In general, defects may increase or decrease depending on the production process used during the production process. Smith R. A. [1] explained that different defects could be identified. During the service life cycle, composite components can be subjected to different stresses that degrade the material, triggering different types of damage [44].

Several non-destructive techniques can be applied to composite materials, including C-Scan. The main objective of these techniques is to quantify and evaluate defects generated downstream of the manufacturing process or during service life. The ultrasound technique gives information about the size and location of the defect. C-Scan is the first technique for inspecting damage in composite materials [45].

3.1.2.1 C-SCAN SYSTEM

Ultrasonic waves are produced by PZT - Piezoelectric transducers that convert an electrical signal into a mechanical vibration in the MHz frequency range. The waves emitted by the transducer are transmitted to the material to be tested through a coupling medium, e.g., water.

As shown in Fig.40, the samples are placed in an immersion tank filled with water. The disadvantages of using this technology include the possible contamination of the components with water or the difficulty of immersing structures with complex geometries.

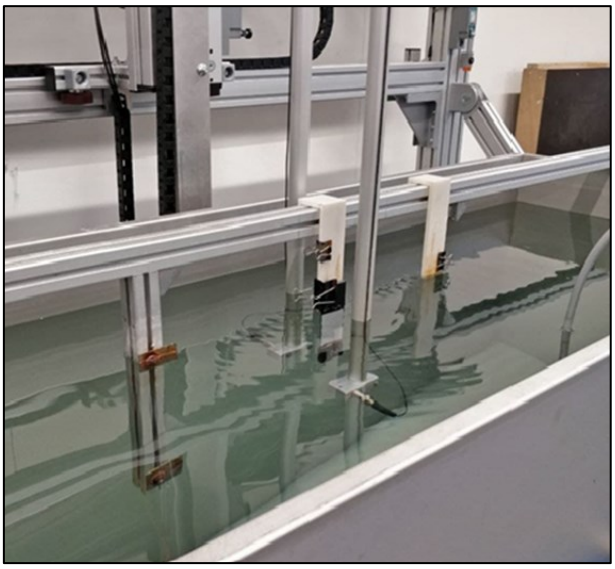

Figure 40 - Immersion tank

When the emitted waves find a defect within the material, one part is transmitted, and the other is reflected. Reflection, attenuation, and absorption within the signal material give rise to attenuation of the emitted energy. The phenomenon of attenuation is significantly present in composite materials.

Fig.40 shows the operation of the C-scan system. Scanning is performed by placing the material checked between the transmitter and the receiver. The transmitter emits an ultrasonic signal which passes through the material and partly reaches the receiver, i.e., a second transducer. High attenuation regions are synonymous with defects, which can be identified by C-scan mapping.

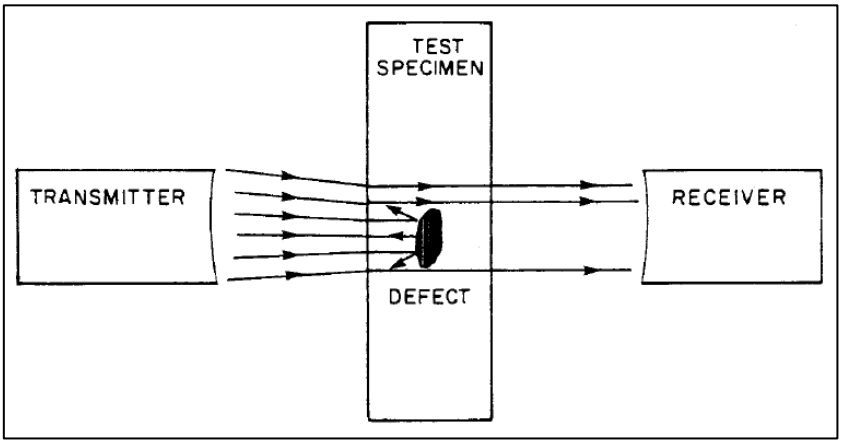

Figure 41 - Test configuration [45]

Several ultrasound-based methods are available for detecting images within composites. All these methods have in common the use of a pair of transmitting transducers. Ultrasound tests are carried out in a medium such as water. For simplicity, not all methods will be described. The methods are A-scan, B-scan, and C-scan. The A-scan transmits the signal's ultrasonic beam and receives a

reflected wave. Time exposure of the ultrasonic beam results in a reflected signal referenced to the desired depth. The B-scan takes place along a fixed direction in the plane. The B-scan shows a cross-section of the sample and gives an estimate of the depth of the defect.

The C-scan records the signal travelling in both X-Y directions in the plane. The C-scan provides an image of the sample's surface and internal defects.

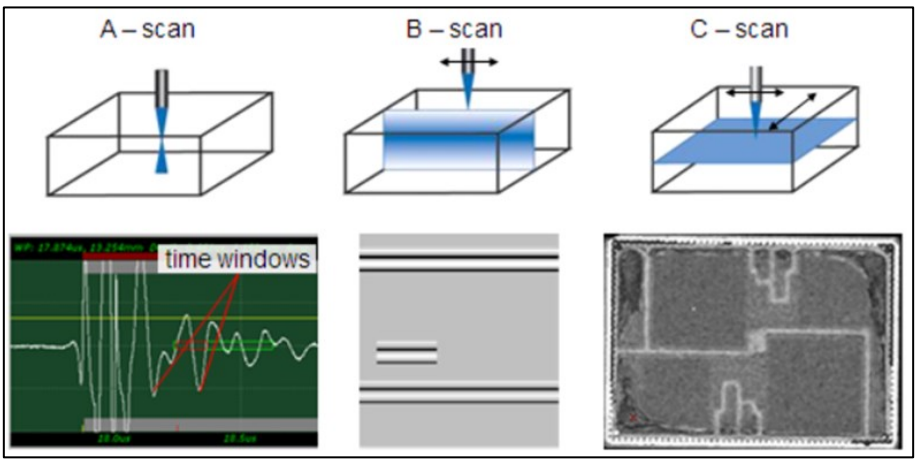

Figure 42 - Possible movements of different scanning methods and the output signal on the software [46]

3.1.2.2 APPLICATION

The increased controls on materials produced and tested using NDT techniques and the consequent improvement in data image processing have made it possible to improve and use checks using ultrasound technologies increasingly.

Each study's common objective remains to evaluate the material's structural integrity after its production [47] or after its stress.

B.C. Rat et al. [48] exploit different NDT techniques, including ultrasound, to better characterise defects in an aircraft's composite, primary or secondary structures to avoid critical damage leading to failure.

In [49], ultrasonic technology was exploited to monitor the growth of the artificial defect placed inside composite laminates. The use of the C-scan made it possible to determine the position and shape of the defect as the shape and thickness of the analysed laminate changed.

3.1.3 ACOUSTIC EMISSION

In the mid-20th century, the Acoustic Emission (AE) technology investigation has begun. Drouillard published two articles [50, 51] and a report on the history of AE [52]. In these texts, the basics and foundations of AE are set out. Specifically, the fundamentals of measurement are

explained, as the development of AE is related to measurement devices [53]. Schofield [54] published his pioneering work entitled "Acoustic Emission". The first time in history the term AE was used was by Schofield.

3.1.3.1 AE METHOD

AET - Acoustic Emission Techniques is part of the NDT testing method [55]. AE is always used during testing, whereas the other NDTs are applied before or after loading the structure. AE is mainly used to detect, identify, locate, and visualise acoustic events resulting from friction in the early phase of the structure in a short time [56, 57]. This technology detects elastic waves radiating from damage within the structure. Therefore, the AE technique can be considered passive and receptive, analysing the pulses of elastic energy released by a defect when it occurs. Defects produce the signals received by the sensors, and each defect growth is a unique event and cannot be reproduced precisely.

A quick release of elastic energy causes a short AE event, i.e., a local dislocation movement. The local dislocation generates the elastic wave that propagates concentric circles and cannot be stopped.

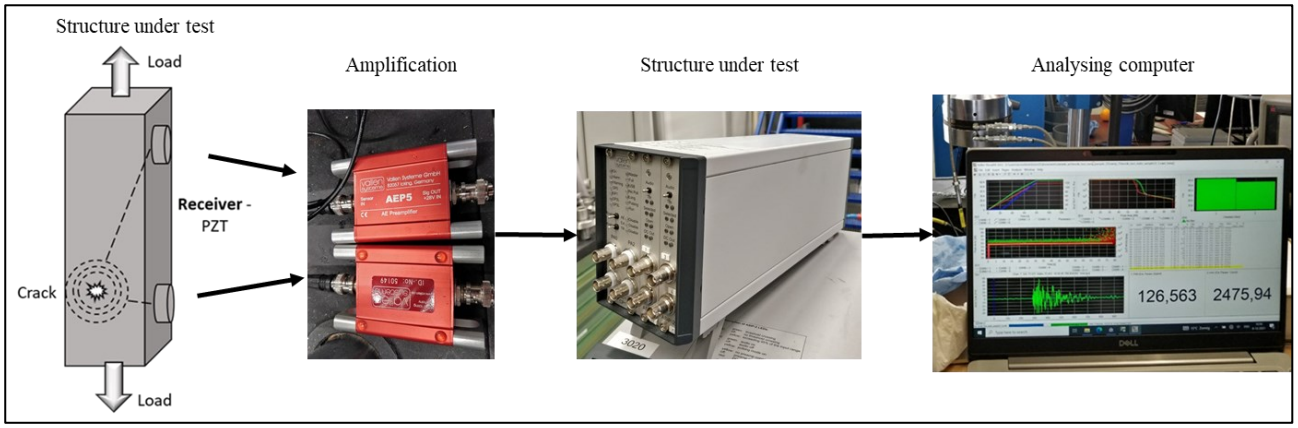

Figure 43 – System of AE

As shown in Fig.43, the AE testing system requires a process chain. It starts with the structure under test to which PZT sensors are coupled to capture the release of elastic energy waves and convert them into an analogue signal. Then, the sensors convert a mechanical wave into an electrical AE signal. Subsequently, pre-amplifiers are connected to amplify the signal intensity coming from the structure. The amplified analogue signal is converted into a digital signal in the following steps, recorded and plotted in diagrams. The analogue signal of the AE waveforms can then be analysed and interpreted for security.

There are mainly two types of AE signals: continuous (emission) and transient (emission). The former is usually produced by external friction or friction within the structure, and it is possible

to see the amplitude and frequency variation. It is an unwanted signal (noise), and the signal never ends. The second AE signal is also called “burst”, and the start and endpoints can be clearly distinguished from the background noise [58].

An example of both types of signals AE is shown in Fig.44.

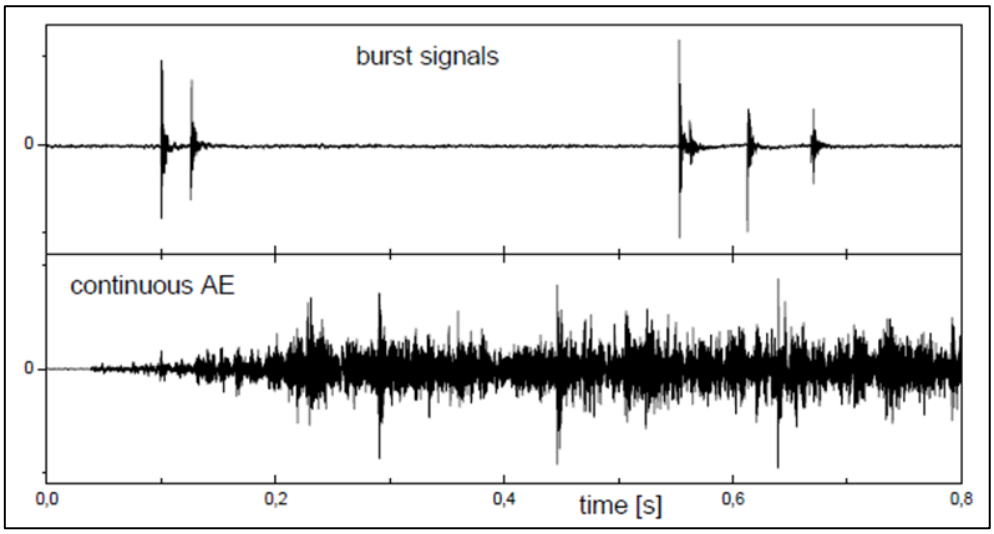

Figure 44 - Example of burst wave signal and continuous wave signal [59]

The task of an AE system is to convert the burst signals into data sets and eliminate the background noise (which can be more or less continuous). For this purpose, a threshold signal must be set to the correct value. If the AE signal exceeds the threshold, a burst is detected (a burst is a detected burst). The moment the signal exceeds the threshold is called the "arrival time" of the burst and is crucial for calculating the event position.

3.1.3.2 AE PARAMETERS

Commonly, the AE signal is analysed using AE waveforms or parameters extracted from them. Fig.45 shows a typical AE waveform. The most essential and used parameters derived from AE waveforms are defined below:

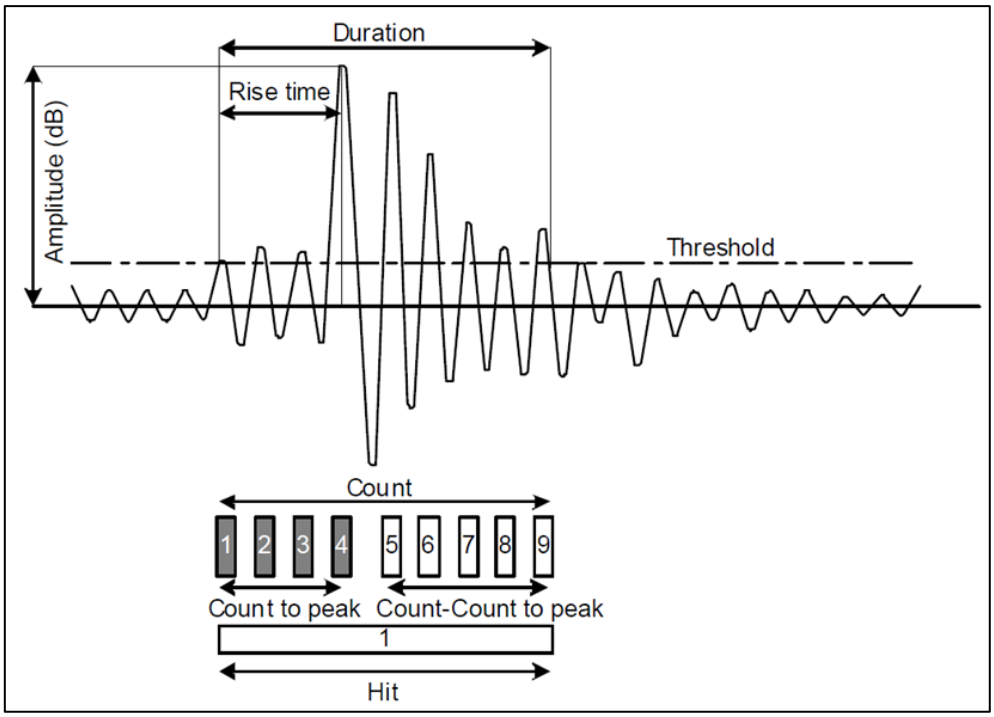

Figure 45 - Waveform typical of AE, including the most important parameters [60]

Threshold: when the AE signal strength exceeds the set threshold, it is recorded by the AE system. The signal is reported in dB units.

- Amplitude: is assigned to the peak voltage of the waveform signal and is reported in dB units.
- Hits: the signal that exceeds the threshold is accumulated in the data set. It is mainly used to evaluate the activity of the AE with the number of counts per period (rate). A waveform is considered a single hit.
- Counts are the number of times the waveform signal exceeds the threshold during the duration.
- Duration: the time interval between the first and last threshold exceedance. Duration is typically expressed in units of µs.
- Rise Time: The time interval between the first exceedance of the threshold and the maximum peak amplitude and is expressed in units of µs.
- Energy: generally defined as the area measured under the signal envelope. Energy is used to interpret the importance of the source event on counts, as it is sensitive to amplitude and duration and less so to threshold and frequencies. It is generally reported in the attoJoule (aJ) unit (1 aJ = 10^{-18}J).

- Peak frequency: corresponds to the point of maximum magnitude in the frequency spectrum obtained from the signal's FFT (Fast Fourier Transform). It is reported in units of kHz.

3.1.3.3 APPLICATION

AE is primarily used to understand structural health by subjecting the material to different types of loading [61, 62, 63, 64] in real-time.

ASTM has also developed a standard for applying AE for Structural Health Monitoring (SHM) [65]. The guide provides definitions and basic principles for applying the AE method used for SHM.

In addition, AE allows the detection, analysis, and clustering of the signal originating from the AE system. Characterising the damage in the structure can bring valuable information, e.g., the damage's type, amount, and location.

Many articles in the literature explain how to proceed with data analysis depending on the objective. In the literature, articles that exploit algorithms for damage characterisation are found. For example, Saeedifar and Zarouchas explain [66]. In [67, 61], they exploit two parameters for the best definition of clusters chosen among nine, and with these, they manage to link the type of damage to related AE events.

3.1.3.4 OVERVIEW OF THE CLASSIFICATION OF AE AND ARTIFICIAL NEURAL NETWORKS

The high number of events recorded during the AE tests can be traced to several characteristic parameters. Different techniques have tried to classify the data obtained from the AEs. Among the methods available in the literature in recent years, machine learning through Artificial Neural Networks (ANNs) [68] has become increasingly popular. This is one of the most current methods. Thanks to the implementation of libraries and toolboxes in commercial and non-commercial software, e.g., Matlab®, it can also be used in this field.

Just as the human brain can learn from the earliest moments of life and define a pattern that depends on various choices and experiences, ANN set themselves the task of artificially reproducing these tasks on machines. ANN has been developed to allow the explanation of physical phenomena that are not well known a priori or too challenging to explain. Neural networks allow the software to mimic the functioning of a brain through a system of nodes called neurons. A single neuron does not have a great capacity, but when combined with other neurons, i.e., with the network, it can perform more complex tasks and achieve great results. The connections or links between neurons are also

called synapses. Each neuron is composed of nodes representing the inputs of the problem and passing through the activation function. Through the synapses, each neuron gives an output. The activation function applies a weighted sum of the input values. It is usually used to normalise the input values in a defined range to avoid possible divergences and that no input exceeds the others.

Each group of neurons with a specific function is called a layer (Fig.46).

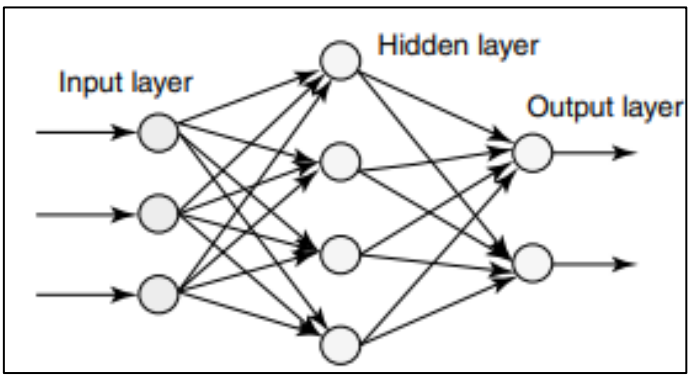

Figure 46 - Multi-layered artificial neural network [68]

Neural network learning can be supervised or unsupervised.

The substantial difference between the two types of learning is that the first one already knows the output of the problem, unlike the second one that does not know a priori the output.

In the case of a supervised network, during the learning process, a model of input is given at the network's input level, propagating up to the network's output. This generates an output model that is then compared with the final model. Therefore, the difference between output and target is calculated through an error. Depending on the error's size, the input values' weight will be modified.

In the second case, the outputs of the problem are not known. Therefore, it will not be possible to define the learning process. In this model, the final objective is to group similar units in contiguous areas of the range of values dependent on input and output. This form is helpful in clustering problems when the nature of the clustering is not known from the beginning.

The Self-Organizing Map (or SOM) is an unsupervised algorithm from the Kohonen Feature Map neural network [69]. This algorithm is based on self-organisation and turns into a map where neural cells with similar functions cluster together. This neural network is mainly used for classification since the outputs are unknown. An example of a structure using the self-organisation algorithm is shown in Fig.47.

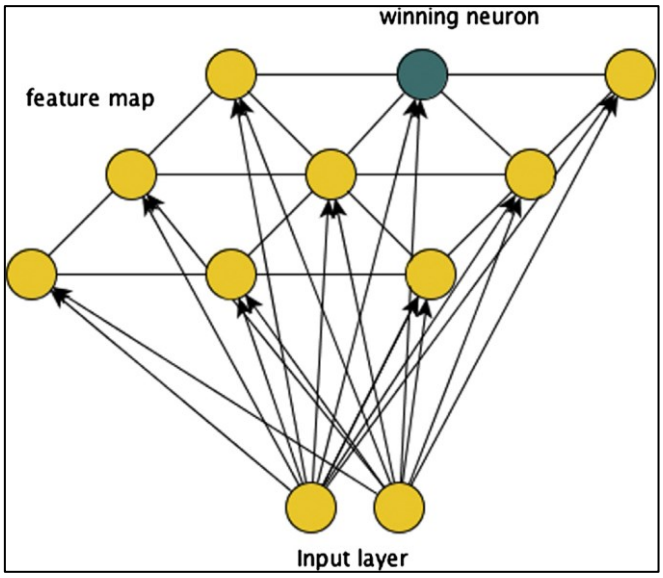

Figure 47 - Self-Organising Map representation [70]

Each neuron on the input layer is connected to each on the map.

The SOM makes it possible to visualise high-dimensional data even in a low-dimensional (2D) space. By classifying the input data, the SOM constructs a hexagonal lattice map with similar data approaching each other and non-similar data receding. The groups are subsequently represented in the U-Matrix, i.e., the 2D topological map using the proximity function based on Euclidean distance [66, 70].

3.1.4 DAMAGE CLASSIFICATION OF COMPOSITE MATERIALS

AE events and their respective waveforms are generated in composite materials while monitoring a structure. The hits produced can give us important information about the type of damage involved in the material, such as matrix cracking, fibre-matrix debonding, fibre breakage, fibre pull-out or delamination and debonding [71]. The extraction of information from signals received by PZTs depends on many factors. Examples are: where the signal is emitted from, its propagation in the structure and the properties of the transducers.

The origins and modes of propagation also vary depending on the wave emitted.

The emitted waves can be of two types: symmetrical (extensional) or antisymmetric (flexural). Matrix cracking and fibre breakage are characterised by symmetrical waves rather than delamination characterised by anti-symmetrical waves. [72, 73].

The various types of damage in a composite are briefly explained below, with examples from the literature. The results for each type of damage depend very much on the material used and the test carried out.

3.1.4.1 MATRIX CRACKING

Usually, matrix cracking occurs at the fibre-matrix interface by shear between two layers. The literature is in accord that places the AE events associated with matrix cracking with medium-high amplitudes and low frequencies [74], but many associates a low amplitude and low frequency [75, 76]

3.1.4.2 FIBRE PULL-OUT

Damage occurs at the interface between the fibres and the matrix. The fibre pull-out causes the separation of the fibres from the matrix. It is widespread in long fibre materials and is present close to breakage. The amplitude emitted by this fracture phenomenon varies greatly depending on the material used and on the test. The amplitude range is between 70-100dB [77] and with frequencies around 180kHz [78] and 300kHz [79].

3.1.4.3 DELAMINATION

Delamination is the separation of two contiguous layers; this damage is hazardous because it develops inside the material without giving any indication outside the structure. This damage tends to include debonding within the same damage class.

Some authors suggest that the signal obtained from damage due to delamination has a generally high duration [80, 79] with high amplitude signals [74].

3.1.4.4 FIBRE FAILURE

As far as fibre breakage is concerned, it is reached when the load is concentrated on a bundle of fibres until eventual breakage. Thus, a high energy release with high amplitudes and a fast rise-time is expected from this phenomenon [81].

3.2 TEST METHODOLOGY

3.2.1 DESIGN OF TENSILE TEST SAMPLES

After identifying the best configuration from the read-out tests, i.e., the specimen with circular slot x3 and Kevlar window x2, stress concentrations caused by the presence of the RFID tag were evaluated using FEM. The objective was to identify a specimen for tensile testing containing a local geometry change caused by the tag. Since the stress concentration is dependent on the ratio of the size of the geometry change to the width and length of the specimen, various sizes were simulated, looking for the minimum size that ensures the same stress distribution of larger sizes.

The following FEM study was based on the reference standard for tensile testing with composite materials [82]. Based on the availability of FEM software, Abaqus 2017® from Dassault was used to perform the necessary calculations. This software made it possible to properly define the properties of the composite materials and Rohacell used in the simulations. In addition, it was also possible to define "Fail Stress" through "Engineering constants" so that simulated load-dependent stress and Failure Indexes, based on theories available in Abaqus, i.e., Tsai-Hill and Tsai-Wu, could be obtained as output. The FEM analysis was developed without including a damage model.

The individual parts of the model were modelled in Dassault's SolidWorks 2020®.

A quarter of the entire model was modelled as it was decided to exploit the geometric symmetries concerning the planes, as shown in Fig.48a-b.

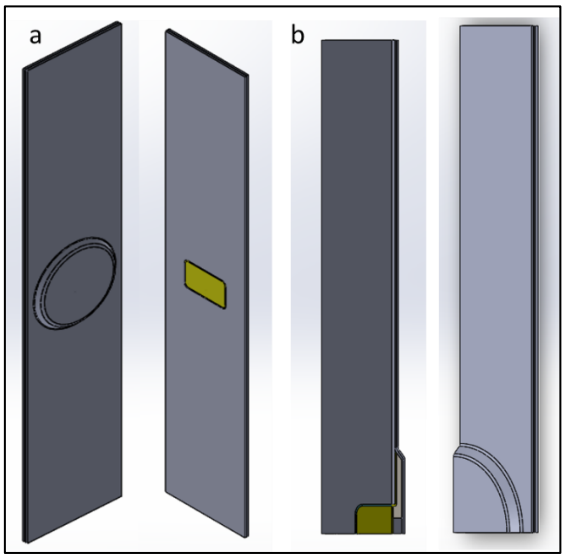

Figure 48 - Tensile test a) whole, b) quarter sample

The model is composed of the following lamination process, chosen in agreement with Dallara company as representative of structural composite skins of their manufactured goods: two plies of CFRPs with the central part drilled and filled with the two Kevlar plies, on top of which the Rohacell insert was placed, and finally wrapped over the whole sample another two pliers of CFRPs.

The complexity of the geometric model led to the further subdivision of the entire model into different parts and importing them individually into the Abaqus environment. This choice was made to discretise better the entire domain of the parts involved. As shown in Fig.49, the model was divided as follows:

a) two frontal plies of CFRPs (Cover),
b) two Kevlar plies,
c) Rohacell insert,
d-e) the two back plies of CFRPs (Back_Ply) were modelled separately.

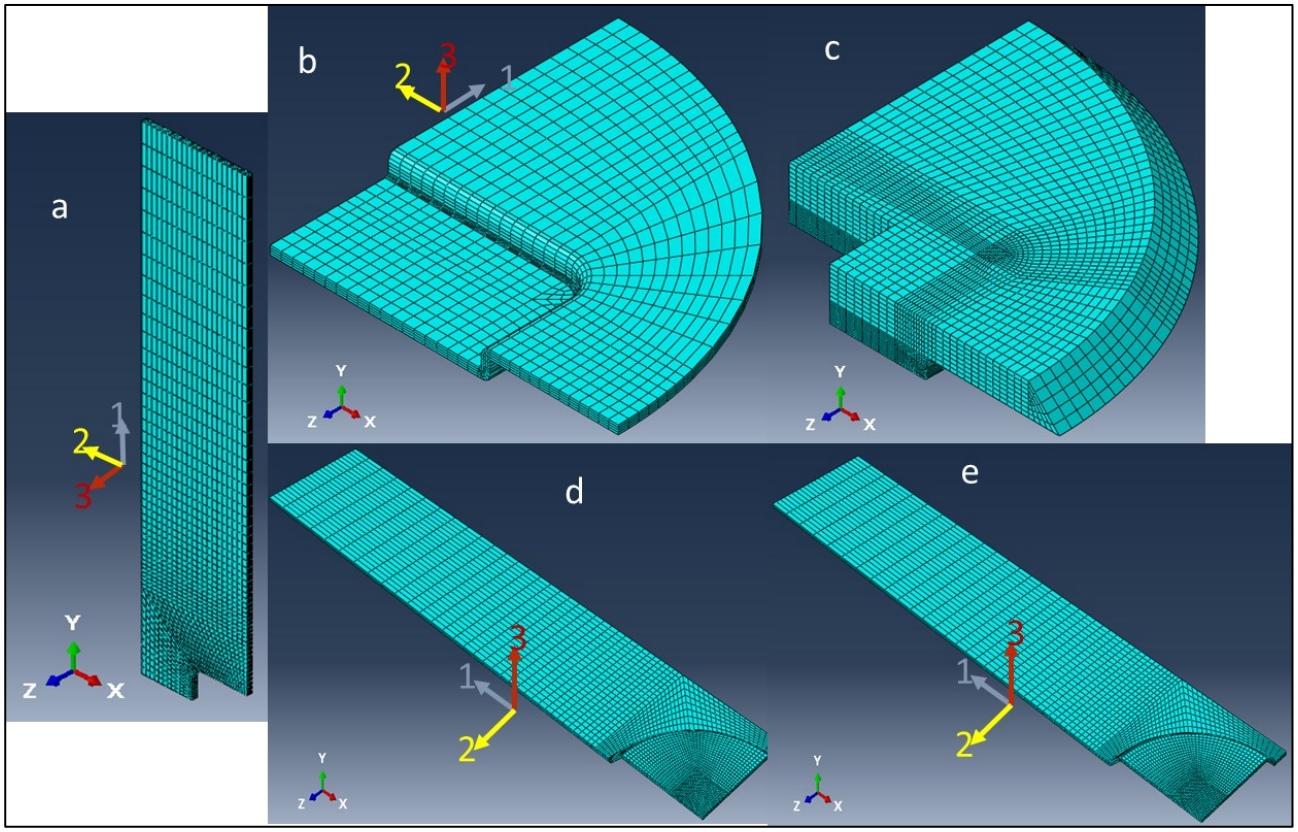

Figure 49 - Meshed parts of the model in Abaqus

In addition, epoxy fillings between the parts were designed. Then, put in the model to connect the parts. The two parts were positioned between the following:

- Kevlar and the cover
- Rohacell and the Back Ply.

Since no damage models were available for the materials used, and to understand the state of tension in the specimen studied, it was decided to use linear elements.

In the meshing phase, the composite parts were associated with Element type: SC8R (Continuum Shell 8-node, reduce integration with hourglass control). On the other hand, the Roahcell was assigned C3D8 (8-node linear brick) and the resin parts C3D4 (4-node linear tetrahedron).

Each part was connected to the previous one using the Tie constraint that binds a slave surface to a master, imposing that there is no relative displacement between the surfaces involved. The ideal conditions for a real uniaxial tensile test were defined through the boundary conditions.

To assess the distribution of the stress distribution in the sample was modelled with different dimensions in length and width.

Each sample was tested with three lengths and widths, based on the basic proportions of 1 time (1), one and half times (1.5) and two times (2). The basic dimensions are equal to 250x50x2.5 mm (LxWxT). Figs.50 a-b-c show the sample with equal length and width variation.

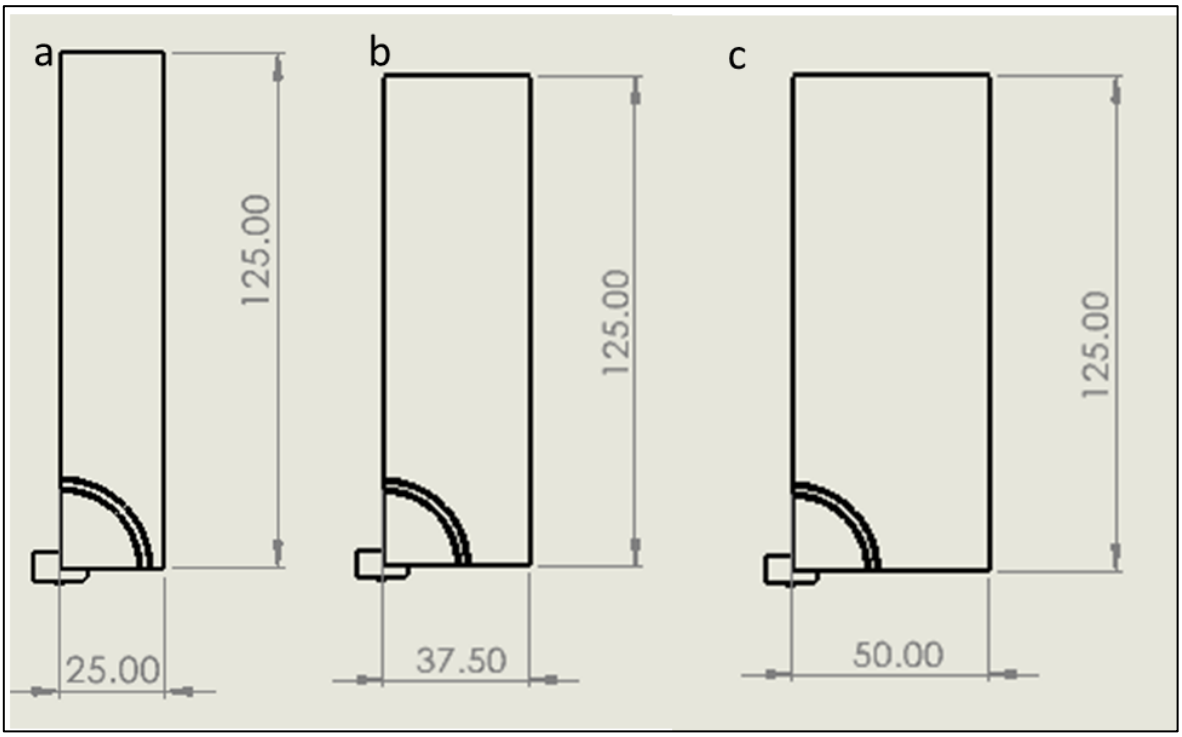

Figure 50 - Design 2D of the tensile test sample with different widths a) 50mm, b)75mm, c)100mm

The simulation outputs contain multiple scenarios of how the parts will be stressed under load. In these simulations, a load of 100MPa was specified. The simulations provided different results based on which scenarios were most likely. The outputs show the stresses in a spectrum of colours. Animations of the simulations are available so that the stresses and movements can be seen over a defined period.

Tab.5 the index failures derived from the Tsai-Hill and Tsai-Wu theories for CFRPs and Kevlar. It is possible to note that with the applied load, the limit of 1 imposed by both theories is not exceeded in any case [83]. As far as CFRPs are concerned, a slight increase in the index can be seen as the length of the specimen increases. On the other hand, the failure index sometimes reaches values close to the limit for Kevlar.

With the same material used, both theories produce similar results.

Table 5 - Failure Index FEM Analysis

Criterion	*Tsai-Hill*					
Material	CFRPs			Kevlar		
Dimension	1	1.5	2	1	1.5	2
25	0.66	0.66	0.67	0.86	0.94	0.84
37.5	0.66	0.69	0.7	0.94	0.78	0.78
50	0.69	0.68	0.62	0.77	0.77	0.77
Criterion	*Tsai-Wu*					
Material	CFRPs			Kevlar		
Dimension	1	1.5	2	1	1.5	2
25	0.66	0.66	0.67	0.83	0.99	0.84
37.5	0.66	0.68	0.7	0.86	0.78	0.79
50	0.69	0.68	0.62	0.77	0.77	0.77

In Fig. 51 a-b-c-d-e-f, the zones in which the maximum simulated stresses referred to the principal directions are obtained in CFRPs and Kevlar. Tab. 6 shows the stress values obtained in the reference zones in CFRPs and Kevlar, respectively.

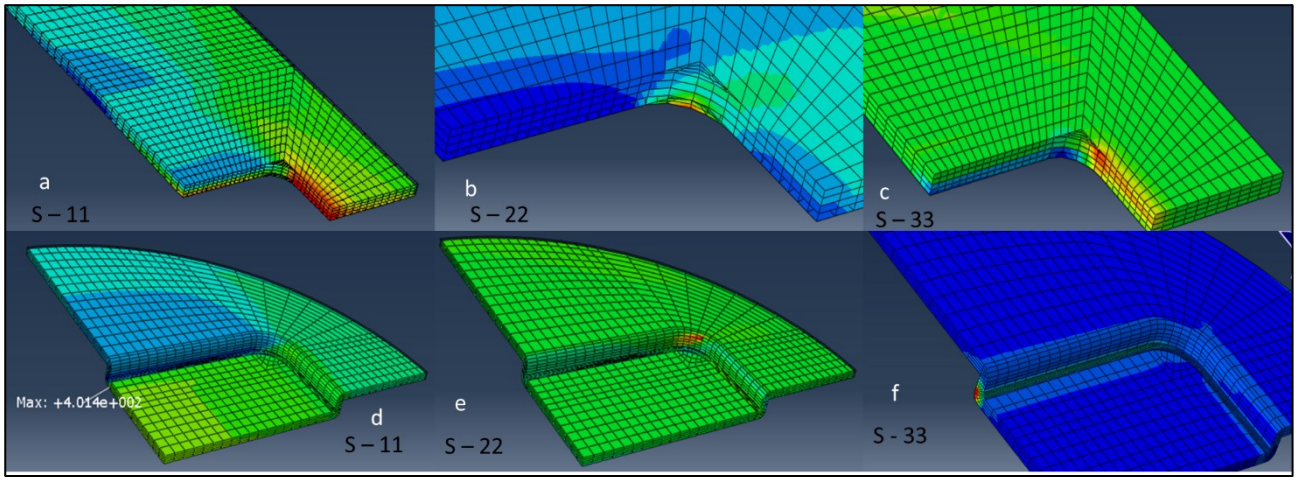

Figure 51 - Stress tensile test simulation a) S11 CFRPs, b) S22 CFRPs, c) S33 CFRPs, a) S11 Kevlar, b) S22 Kevlar, c) S33 Kevlar

From the Index Failure values obtained and the stresses generated by the FEM model, it is possible to note how the values obtained among the various set-ups studied obtain values close to the

base case, i.e., 25_1. This has led to the decision to create a specimen with dimensions of 250mm x 50mm x 2.5 mm (LxWxT) for the actual case.

Table 6 - Stress simulated in FEM analysis

Simulation code Nr	*CFRPs*						*Kevlar*					
	S - 11	S - 22	S - 33	S - 12	S - 13	S - 23	S - 11	S - 22	S - 33	S -12	S - 13	S - 23
25_1	262	94	30	46	32	14	400	140	92	27	16	16
25_1.5	264	79	30	46	36	10	349	133	96	29	8	13
25_2	275	87	32	46	36	12	404	142	89	26	8	16
37.5_1	265	89	30	45	35	12	329	140	83	27	7	13
37.5_1.5	260	79	29	46	35	18	378	133	87	26	8	13
37.5_2	272	94	29	49	35	17	380	138	84	24	7	15
50_1	279	85	28	48	35	22	375	138	83	24	14	15
50_1.5	279	90	28	47	35	22	373	137	83	24	14	15
50_2	246	94	28	43	35	16	372	133	86	26	14	14

3.2.2 TENSILE TEST

Tensile tests are based on ASTM D3039M-14 - Standard Test Method for Tensile Properties of Polymer Matrix Composite Materials. As explained in the previous section, the samples were made with different dimensions to the reference standard. The dimensions of the samples are 250x50x2,5, and on the bump area, it reaches 5mm, due to the insertion of the Rohacell and Kevlar insert. As suggested by the standard, five samples were tested for failure.

The tensile test specimens were produced by a cure cycle in an autoclave at 120°C at 2 bar for 120 min. The composite materials used to produce the test specimens were pre-preg. Following the above cure cycle, the first part produced is the insert composed of Kevlar (K 170 AA285 DT120 50% Deltapreg) and Rohacell WF71. It is then placed in the centre section after creating a central hole in two layers of carbon fibre (C 630 T700 12K 2x2 DT120 37%). After positioning the insert, two more carbon fibre layers are wrapped over it.

A plate containing several test specimens was treated. Finally, the plate with the cured specimens was cut by a waterjet, obtaining specimens with dimensions 250mm x 50mm.

In addition, two more square carbon fibre plates (the same material used for the specimens) with a side of 50 mm were glued to both ends of the specimen to prevent any possible damage due to grasping. Specimens were made for both types of tests.

Fig.52 shows the tensile specimen and an example of a real specimen. In Tab.7, the mechanical properties of the materials used are presented.

Figure 52 - Image of tensile composite specimens a) front and back, b) with the tabs and spackle patter surface for DIC, c)side view with detail of the bump

Table 7 - Mechanical properties of the used materials

Materials property	*Tensile Modulus [MPa]*		*Shear Modulus [MPa]*	*Tensile Strength [MPa]*	*Poisson Ratio [-]*
	E_1	E_2	G_1 G_2 G_{13}	σ_T	ν
C630 (CFRPs)	58500	58150	5000	900	0.03
K 170 (Kevlar)	27500	29900	1900	476	0.08
WF 71 (Rohacell)	105		42	2.2	0.25

In addition, several instruments were used during the tests to monitor the damage and assess the deformation state of the sample. As can be seen, Fig.53 provides a positioning diagram around the test machine.

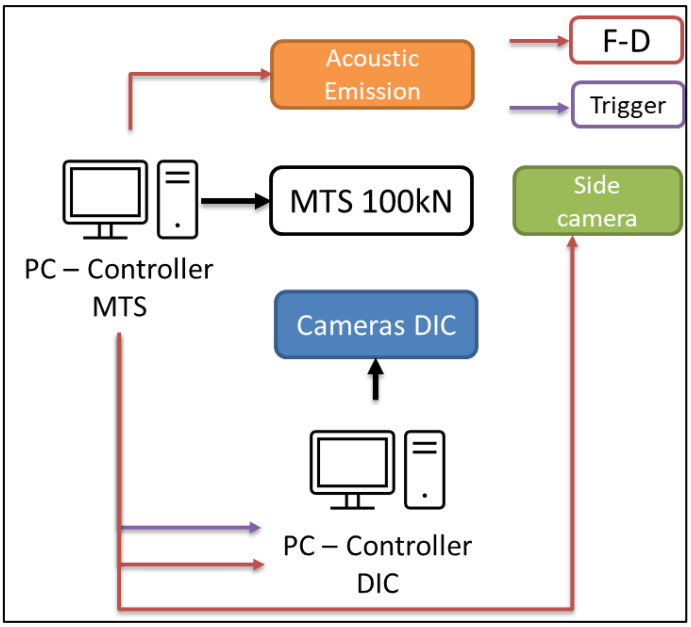

Figure 53 - Set-up instrumentation test

The testing machine used to perform the tensile tests is an MTS electromechanical testing machine with a load cell of a maximum capacity of 100kN. In addition, a test speed of 1mm/min to failure was applied. The test speed was set so that the AE system could not hear too much noise while acquiring data. Moreover, the force and displacement of the machine's crosshead were recorded throughout the test.

The diagram in Fig.51 shows what information had to be provided to the various instruments, i.e., Force - Displacement. Each test was monitored with DIC, the side camera and AE.

The same acquisition software as DIC (VIC-3D) was used to visualise and estimate the deformation field of the first lamina. The DIC measurement system consists of two 9MP resolution mountable cameras, with 25mm lenses and stereo-angle equal to 30°. The cameras were connected to the VIC Gauge acquisition system [84]. In addition, a light source had to be placed behind the cameras to achieve proper light exposures of the sample surface.

Before testing, the DIC system needed to be calibrated. The calibration process was carried out using objective panels (Fig.54), varying the position of the objective panel during the acquisition of the calibration images. The objective panel is rotated within the intended plane where the sample to be tested is positioned.

Figure 54 - Calibration panel a) front, b) back

The DIC acquisition system was synchronised for each frame with the testing machine's corresponding load and displacement value.

The software used for post-processing is VIC-3D. Finally, the specimen was prepared to obtain a speckle pattern on the sample's surface exposed to the DIC cameras. The specimen painting process was carried out in the paint shop within the laboratories of the TU Delft. Then for the analysis for DIC, a fine speckle pattern was applied to the surface with the Kevlar window exposed. First, a base coat with a thin layer of white non-glossy spray paint. Afterwards, all studied samples used black non-glossy spray paint to obtain a similar defined spackle pattern.

Fig.55 shows the cameras' set-up and the light source used, and Fig 56 shows the control PC with which the images acquired by the VIC Gauge 3D system could be configured. The sampling frequency of the acquired images is 2s.

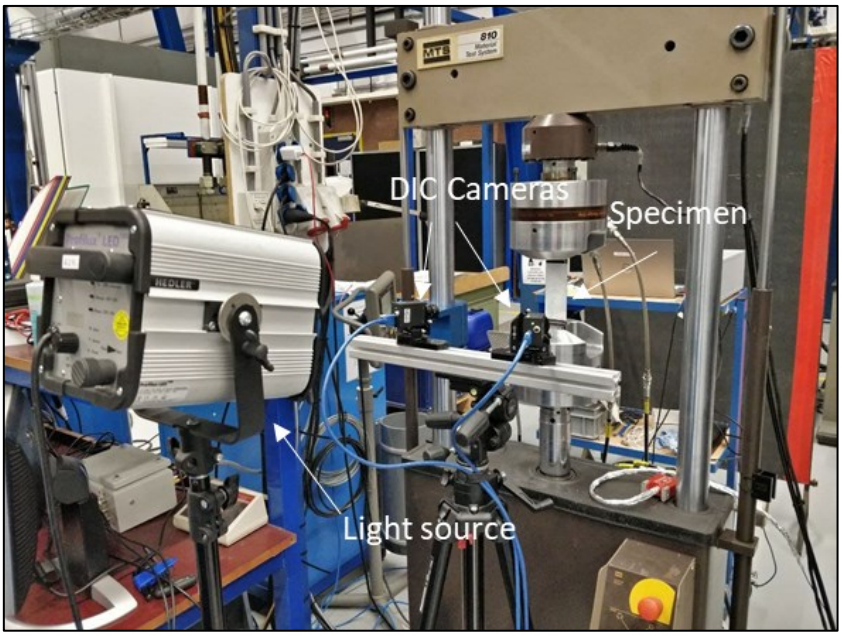

Figure 55 - Set-up DIC cameras and light source

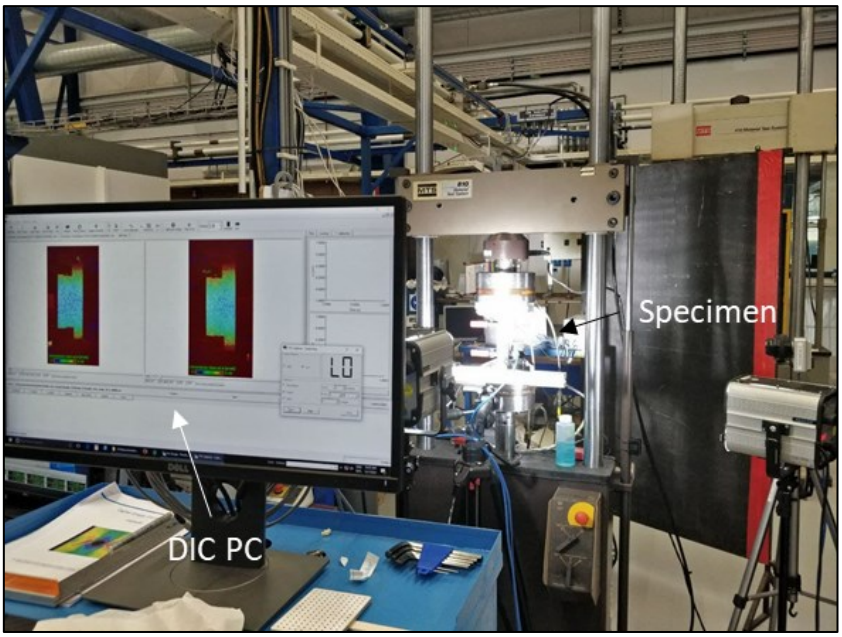

Figure 56 - PC (Controller DIC) with VIC Gauge 3D Software

A camera was placed sideways to evaluate post-processing, when and what damage occurred outside our samples, such as delamination or shear damage. As shown in Fig. 56-57, it was placed next to the machine to focus the side view of the sample. In order to obtain sharper photos, a light source was placed without interfering with the DIC system. The camera is an Optomotive Velociraptor with a 2.2MP resolution of a 50mm lens. Sampling was carried out with image acquisition every 2 seconds.

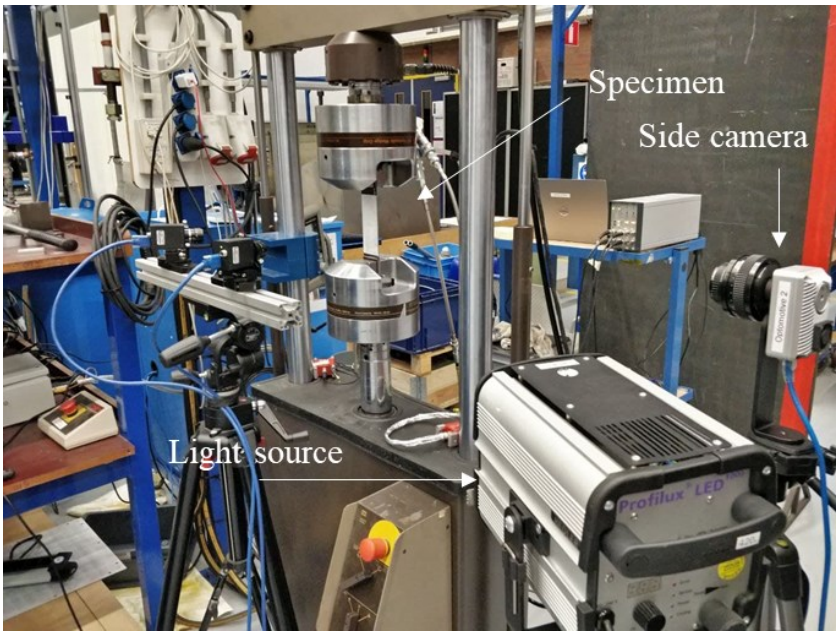

Figure 57 - Set-up side camera and light source

The instruments shown in Fig. 58 were used for the entire AE measurement system during the tensile tests. The system is composed of the two PZT Vallen VS900-M sensors (working in the frequency range 100-900kHz), each sensor connected to a 34dB Vallen AEP5 pre-amplifier and connected to four-channel Vallen ASMY-6 acquisition units through low-noise cables. Furthermore, rules have been defined for acquiring AE events and managing the data obtained from Vallen AE-Suite Software R2020.1124.2.

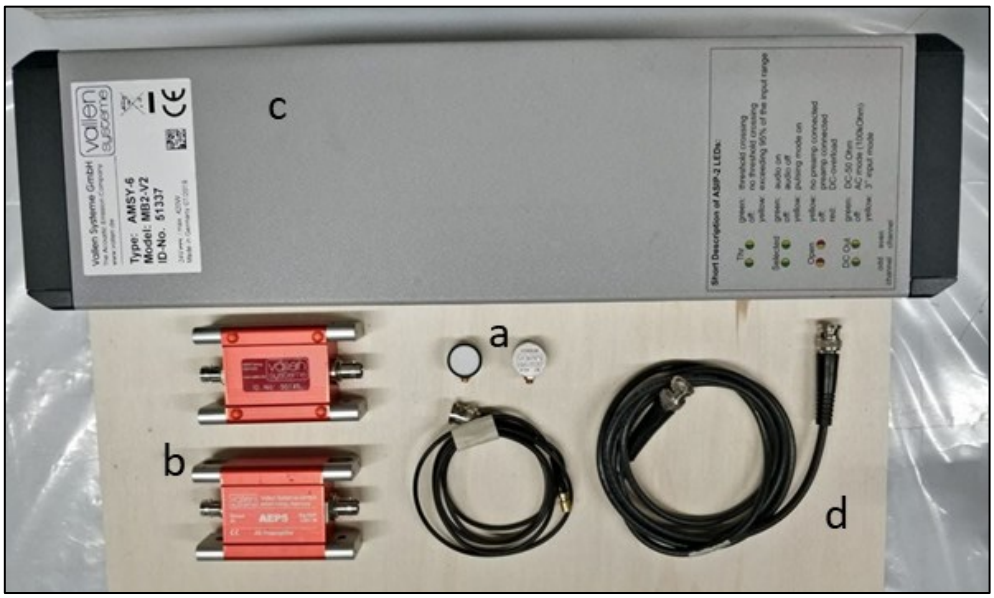

Figure 58 - Vallen System: a) PZT sensor VS900-M, b) pre-amplifier Vallen AEP5, c) four-channel Vallen ASMY-6, d) low-noise cables

The instruments shown in Fig.58 were used for the entire AE measurement system during the tensile tests. As shown in Fig 59-60-61, the system starts from the two PZT Vallen VS900-M sensors (working in the frequency range 100-900kHz); each sensor is connected to a 34dB Vallen AEP5 pre-amplifier and connected to four-channel Vallen ASMY-6 acquisition units through low noise cables. Furthermore, Vallen AE Suite R2020.1124.2. The Magnaflux "Ultragel II" was used to pair the PZT sensors on the sample. It has also ensured the continuous transmission of AE signals between the sample and the sensors. A pencil lead break test was performed to verify the transducer coupling. The AE signal was monitored with the two sensors positioned 100 mm apart (Fig. 61). It can be concluded that most of the AE signals were generated in the section between the two sensors during the tensile test. Finally, Tab.8 shows the parametric characteristics of the transient AE strokes (e.g., amplitude, duration, counts, energy, rise-time) and their complete waveforms recorded during the tests with a given sampling rate.

Table 8 - Acoustic emission acquisition parameters

Parameters	***Value***
Sampling rate for the acquisition of AE features	10 MHz
Sampling rate for the acquisition of AE transient waveforms	2 MHz
Amplitude threshold	55 dB
Rearm time	200 µs
Cut-off-frequency (minimum frequency of acquisition)	25 kHz
Duration discrimination time (time window to register each AE signal)	200 µs
Digital pass-band filter	25kHz – 850kHZ

Figure 59 - Experimental system of tensile test and AE monitoring

Figure 60 - Acoustic emission sensors positioned during the Tensile tests a) back view b) side view

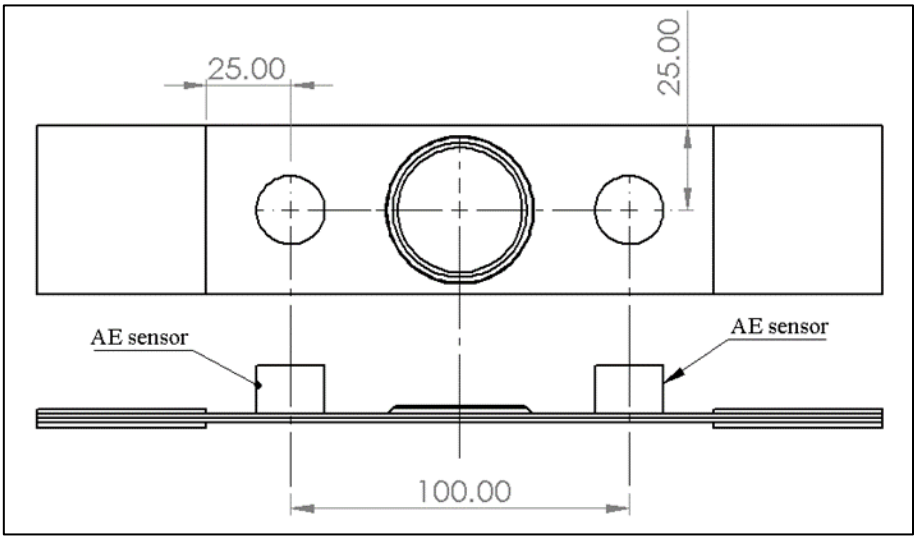

Figure 61 - Acoustic emission sensors positioned during the Tensile tests - scheme

Further monitoring of damage and morphology of the fractured specimen was observed using the C-scan. The tested specimens were analysed using the C-scan by placing them in a tank filled with water (Fig. 40 - 3.2.2.1) to assess the undamaged specimen's state. Finally, each sample was tested until breakage was placed under observation again.

Shows in Fig. 62 were used to evaluate the defects within the sample structure of the Olympus EPOCH 650 [85].

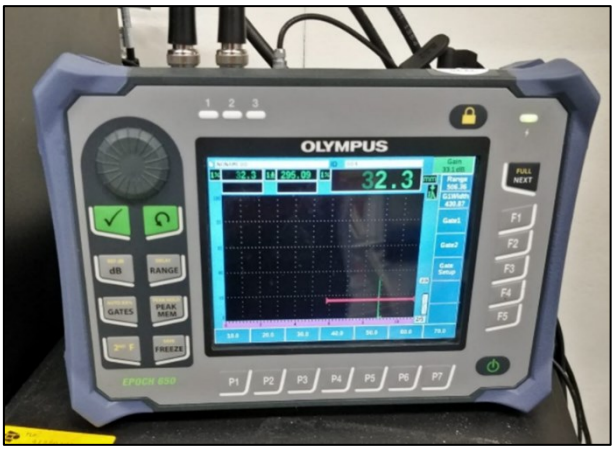

Figure 62 - Ultrasonic flaw detector Olympus EPOCH 650 [85]

3.2.3 INTERRUPTED TENSILE TESTS

To better understand the growth and damage within our sample, it was decided to divide the test into several intervals until the sample broke. Then, the samples were subjected to tensile loads with a load-unload-reload. The specimens used in these tests have the same dimensions as the static tensile tests. As in the previous case, the tests were carried out using the MTS electro-mechanical testing machine with a load cell with a maximum capacity of 100kN. The test was conducted under displacement control of 1mm/min until the imposed limit force was reached. At least three specimens were tested with the same condition. Again, the force and displacement of the machine's moving crosshead were recorded during the test. The instruments used to monitor the damage and understand the deformation state of the specimen are the same as those shown in fig.50. Examples of the ramps made by the specimens during the tests are shown in fig.63.

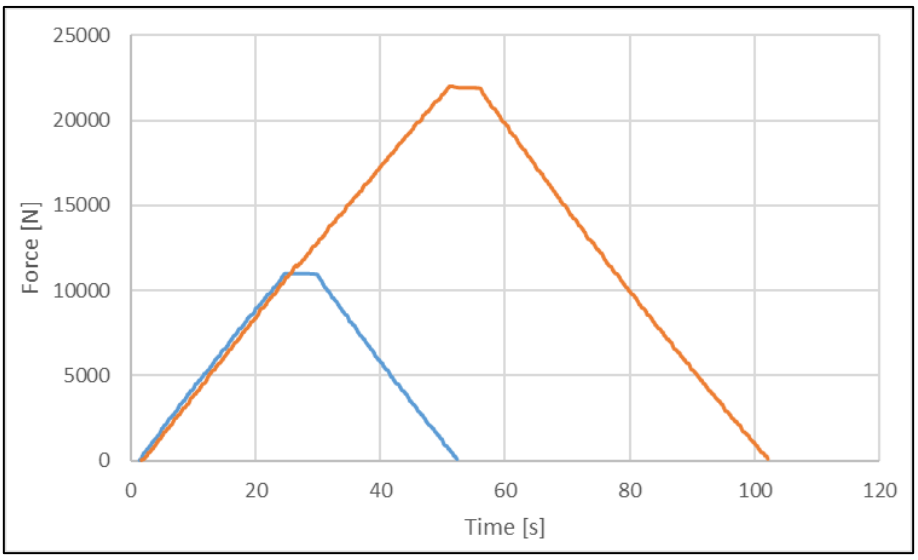

Figure 63 - Example of test ramps at different force levels

The interrupted test can be subdivided into three steps: the first part refers to the loading part up to the imposed force level, the second part is the maintenance (or dwell) of the imposed force level, and finally, the third part is the unloading of the test specimen. The test was performed in displacement control, and the specimen's speed set during loading and unloading is 1mm/min.

In this case, the information acquired with the DIC was only during the loading step section until the end of the holding at the given imposed force level. The cameras and the settings used are the same as those explained for the tensile test. The same applies to the software used during the test and post-processing. Also, in this case, the surface of the samples was prepared to acquire the state of deformation of the first foil, applying a layer of matte white paint and the spackle pattern with black matte paint. In order to achieve greater sensitivity, the sampling rate was increased in this case, i.e., a picture was taken every 800ms.

A camera was placed on the side of the MTS to capture photos of the side of the sample during the test. In contrast to the static tests, the photo sampling was divided into two cases. In this experiment, the specimens were subjected to the ramp-up to failure, and images were acquired every 2 seconds. In the remaining cases, it was decided to take only one picture while maintaining (or dwell) the force level.

The sensors and instruments used for the AE were the same as the static case. Data acquisition was made during the whole test.

As in previous tests, an additional damage monitoring tool, the C-Scan, was used. When the test reached the highest ramps and unload value, the sample was removed from the testing machine, placed inside the tank, and scanned. In this way, it was possible to understand better the evolution of the damage inside the sample at different load levels. Subsequently, being an NDT test, the same sample was placed back into the machine and tested at the next load level. This process was repeated up to the last ramp, i.e., that of sample failure.

Finally, a micrograph was taken under an optical microscope to describe the internal damage of the sample. For this check, different samples were tested at different strength levels. As shown in Fig.64, an example of a tested sample was sectioned in half longitudinally to the direction of loading (Fig. 64a). One of the two halves was divided transversely to the applied load (Fig. 64b).

Before acquiring images of the samples, the sectioned parts were specially prepared by lapping.

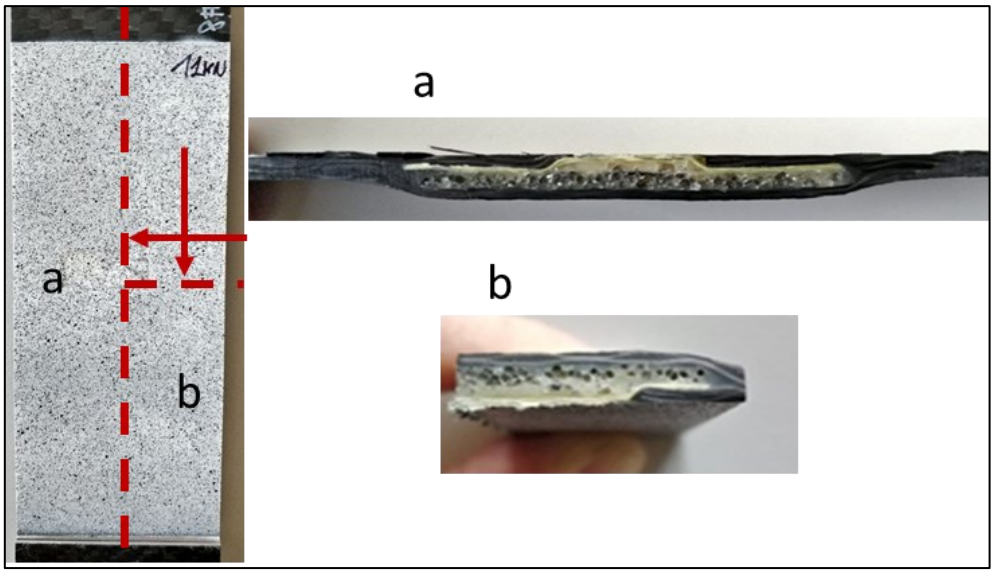

Figure 64 - Example of the sample tested at 11kN, a) longitudinal section, b) cross-section

This procedure was carried out for each force level considered.

The images were acquired with the Leica DMi8 M / C / A (Fig. 65) inverted light microscope for the industry.

Figure 65 - Inverted Microscope for Industrial Applications Leica DMi8 [86]

The optical microscope analysis was carried out in the laboratory of Materials and Metallurgy in the Department of Engineering and Architecture of the University of Parma.

3.3 RESULT AND DISCUSSION MECHANICAL PART

3.3.1 TENSILE TEST

Five tensile tests were conducted to obtain the reproducibility of the experimental results. Fig.66a-b shows the force-time (a) and force-displacement (b) curves obtained with individual specimens until failure. It can be seen that in the first section, all specimens behave similarly, which is almost linear, despite the second and last part, which are inelastic characteristics for hybrid structures failure, as seen by Jalalvand et al. [87, 88], which heralds a significant drop in load and therefore a failure. The drop in load during the test indicates visible delamination in the [89] structure.

Table 9 summarises the values of the failure loads with their mean and standard deviation, 54.89kN and 3.43kN, respectively. In addition, the values extracted from the AEs as total events, average Amplitude and average Peak frequency for the respective tests are listed. When comparing the values obtained, it can be seen that the average amplitude and PF values obtained are similar among the specimens. In agreement with this, the general mechanical behaviour shown by all the specimens is the same.

The failure modes presented by the specimens were similar throughout the set of specimens studied. The main failure modes found were: 1) matrix crack during the whole test, which caused a consequent 2) detachment of the kevlar-carbon polymer and Rohacell-carbon interface (f/m failure interface) since the lowest loads, followed by fibre breakage (kevlar and CFRPs) and catastrophic delamination (or debonding) between the carbon layers.

In order to better understand and correlate all the data obtained from the tests, graphs of AE events as a function of time and force normalised to the maximum load achieved will be shown.

For simplicity, since the specimens' responses were similar to each other, only one specimen will be treated, but the process was replicated in the same way for all specimens. Nevertheless, the types of damage developed in the example specimen were replicated to a greater or lesser extent in the remaining specimens. The damage involved in the samples was analysed not only by AE, which gives us an indication based on the literature and various parameters that will be explained later but also by comparing DIC, side camera and C-Scan.

Moreover, the pencil-lead break (PLB) test [90] was carried out to assess the correct functioning of the sensors, as recommended by standard ASTM E750.

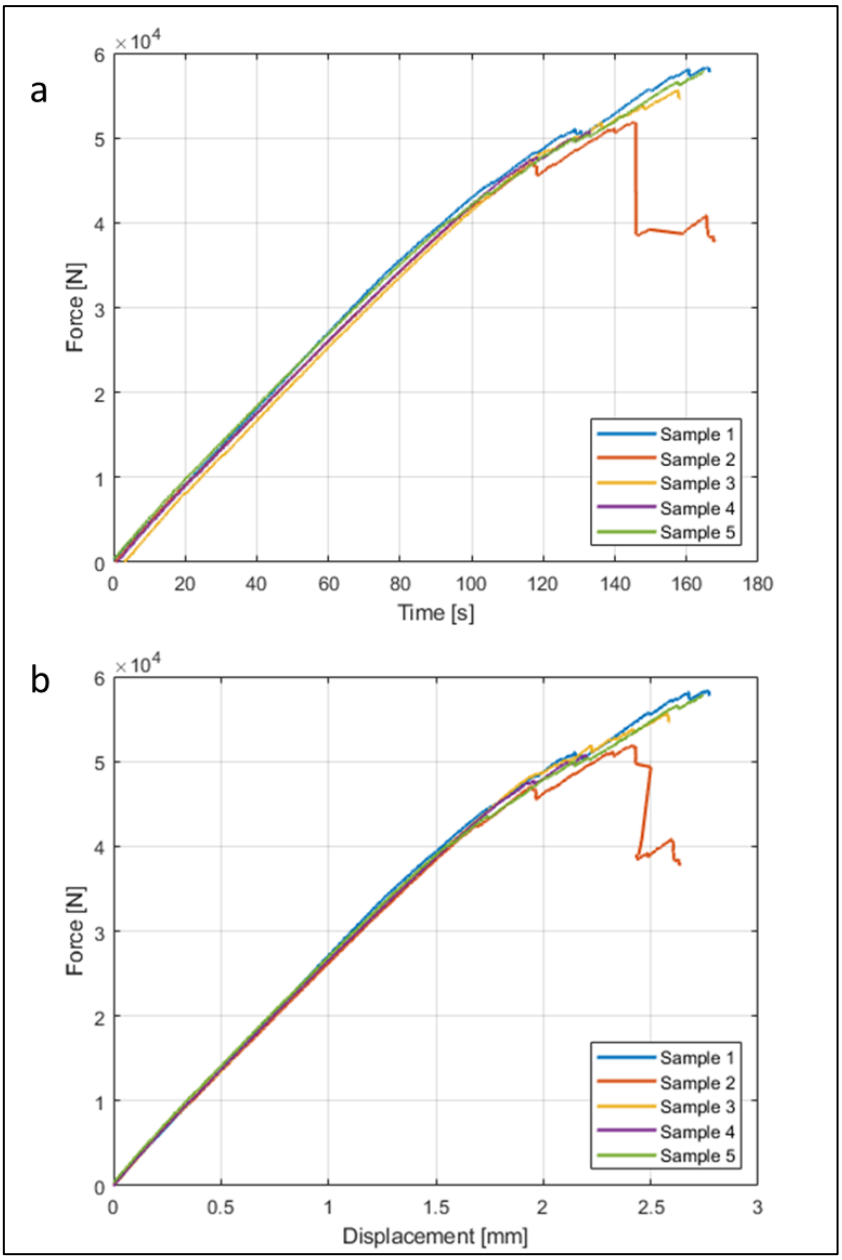

Figure 66 - Tensile Load curve a) Force vs Time b) Force vs Displacement for the composite sample

Table 9 - Summary of measured mechanical properties and corresponding AE characteristics

Material	*Failure Load*			*AE Parameter*		
	Failure Load [kN]	*Mean value [kN]*	*Standard Deviation*	*AE Events*	*Average Amplitude [dB]*	*Average Frequency [kHz]*
Sample 1	58.32	54.89	3.43	180368	80.9	91.95
Sample 2	51.85			195290	78.6	94.68
Sample 3	55.69			155207	79.98	96.61
Sample 4	50.8			120483	80.14	96.64
Sample 5	57.83			148945	80.42	106.08

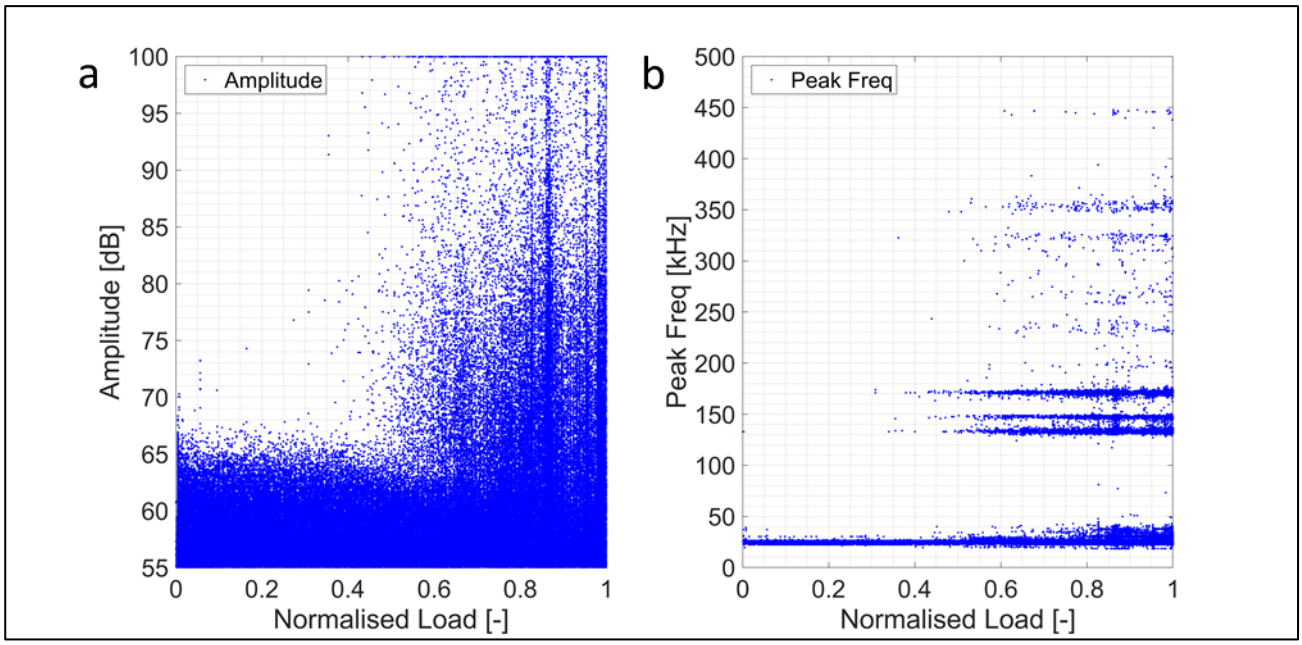

Figure 67 – Events of AE vs Normalised load a) Amplitude, b) Peak Frequency during the tensile test of sample number 1

After carrying out the tensile tests, the raw data obtained from the AEs were analysed. Therefore, will be shown the data concerning sample number one. The types of damage involved and the individual AE responses will be shown in detail rather than images representing the actual damage state at that instant.

Fig.67 shows the dispersion of the raw data obtained from the reference test as a function of amplitude Fig. 67a and the distribution as a function of peak frequency in Fig. 67b. The data will be represented as a function of time and energy. This has been adopted as it allows the first case to evaluate a correct evolution of the damage by correlating it visually with the visual monitoring tools. On the other hand, energy, especially for composite materials, is a significant datum and allows us to anticipate the understanding of rupture. The energy release rate and the accumulated energy will be considered during the results and the counts and cumulative counts.

Before starting the tests and placing the samples in the MTS, they were C-scanned to assess their structural integrity. Fig.68a depicts the sample image obtained from the C-scan analysis, and it is then compared with the sample's image after total failure. Fig.68b-c show the DIC and the lateral camera images.

It can be seen sudden that the image obtained at the C-scan (Fig 68a) recognises the presence of the void created by the rectangular-shaped Rohacell insert.

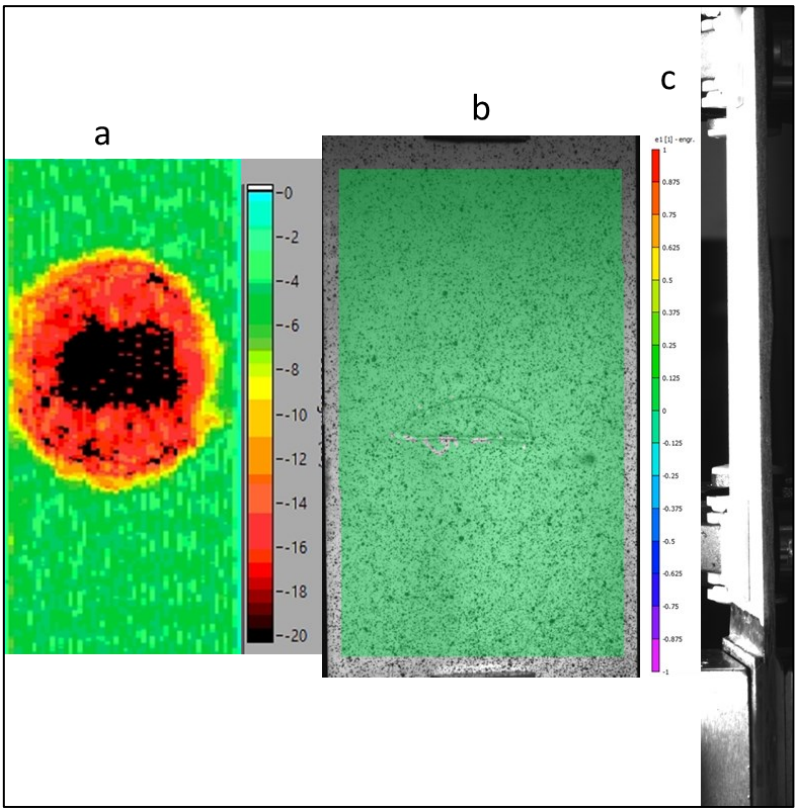

Figure 68 - Sample state at the beginning of the test a) C-scan b) DIC c) Side camera

3.3.1.1 PARAMETRIC CLASSIFICATION OF AE EVENTS

As mentioned above, the raw data obtained during the test were analysed, so the totality of events will most likely also consist of AE events due to the background noise of the testing machine. Therefore, it is challenging to establish further conclusions regarding the tensile tests of AE waveforms and damage types. Therefore, a well-defined data analysis procedure based on unsupervised ANNs was used to best describe the events.

From the single events, the main parameters that helped to describe the AE waveforms better were extracted, such as:

- Amplitude, in dB (logarithmic scale regarding the 1mV voltage at the sensor output),
- Duration in μs,
- Energy in eu (1 eu = $10^{-14}V^2s$),
- Counts is the number of oscillations of the waveform (in μs),
- Rise-Time in μs,
- Decay Angle (in μs, the angle of the slope from signal maximum to the last threshold crossing),
- Variance (the amplitude variability of the acoustic emission signals)

- Frequency of the centroid: helpful to characterize the overall frequency content of an acoustic emission signal.

The described parameters were extracted, related, and finally given a meaning.

Before the parameters can be given meaning, it is necessary to understand their relationship. As seen in [91], the parallel coordinate graph (PCP) comes into play here.

With PCP, it is possible to represent the n-dimensional correlation between the various parameters in a 2D graph. Each dimension, or parameter, is represented by an axis, and the axes are represented as equally spaced vertical lines. To understand the meaning of the various parameters are grouped into a range of values from 0 to 1. Each line represented in the 2D graph proceeding from one axis to the other represents a single value of the AE event dataset and refers to the relationship existing at the two parameters (axes) it connects. Therefore, it is sufficient to plot all events on the same graph to display the entire AE dataset. The values were normalised in a range from 0 to 1 to avoid incorrect display and evaluation.

Each axis was equally divided into a range of 0.25 to highlight the correlation or otherwise between the parameters. The division allows us to understand whether or not there are overlaps between the lines and how they are distributed between adjacent vertical axes. The distribution of the lines shows us the possible relationship and correlation between the parameters.

Explaining the possible cases of representation of parallel coordinates briefly, if the lines between two axes are parallel, there is a strong and positive correlation; if there is a disordered overlap between the lines, there is no correlation. Finally, if the lines converge at one point without excessively overlapping, there is a strong negative correlation (inverse). In order not to distort the parameters, the last case is chosen.

In this direction, and as shown in Fig.70, the parameters with the reasonable correlation are ***amplitude*** and ***duration***, and the lines overlap relatively little. We also note that the distributions are different along the axes of the parameters considered.

At this point, the SOM is used. Then, after having inserted the two parameters as input, the matrix U is created with the help of the algorithm k-means using a certain number of clusters. Nevertheless, to determine the optimal number of clusters, the evaluation procedure was based on the use of three indexing criteria, described by Crivelli et al. [70]:

1. Silhouette [92]
2. Davies-Bouldin [93]
3. Calinski-Harabasz [94].

In order to better understand the values obtained from the three indexing algorithms, a brief definition is given for each algorithm:

1. Silhouette for good clustering from high values;
2. Davies-Bouldin for good clustering from small values;
3. Calinski-Harabasz for good clustering from high values.

The evaluation of several algorithms allows overcoming the limits set by each.

In our case, the minimum and the maximum number of clusters considered are 2 (c_{min}) and 10 (c_{max}), respectively.

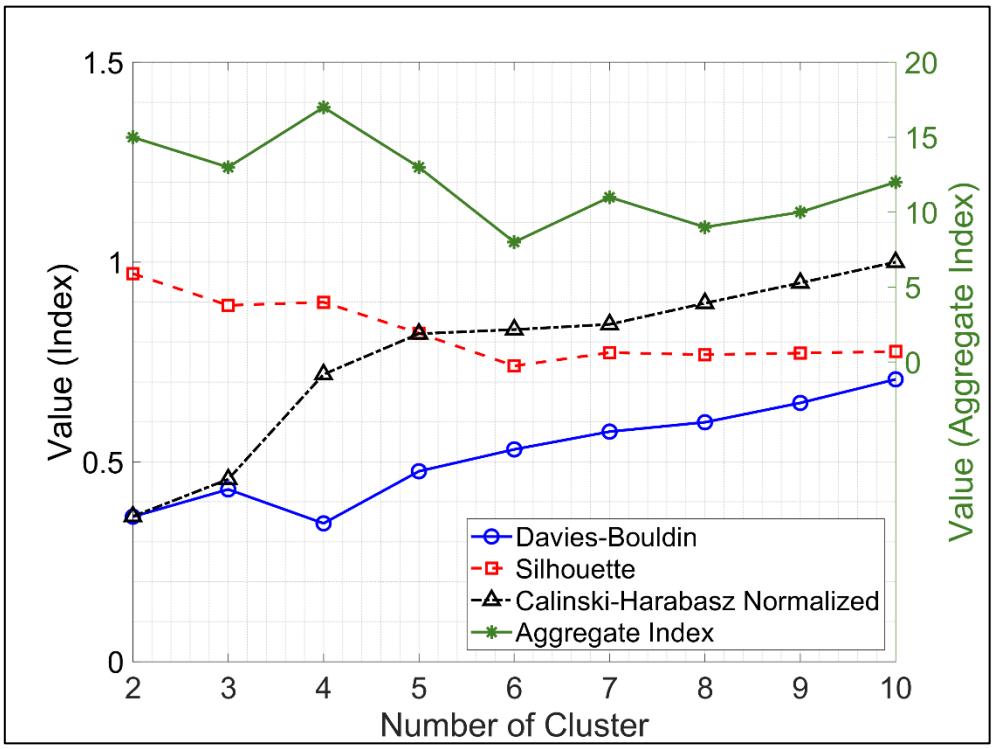

Figure 69 - Index values for each criterion (Value - Index) and aggregate index value to predict the optimal cluster

The extraction of the optimal number of clusters for the reference sample is 4, as shown by the aggregate index value (Fig. 70).

As explained above, the process described was performed for each sample examined. The classification provides similar results using a different sample and identifies the optimal clustering with 4 clusters. Therefore, the remaining samples were clustered using the same procedure as the SOM algorithm and k-means with 4 clusters.

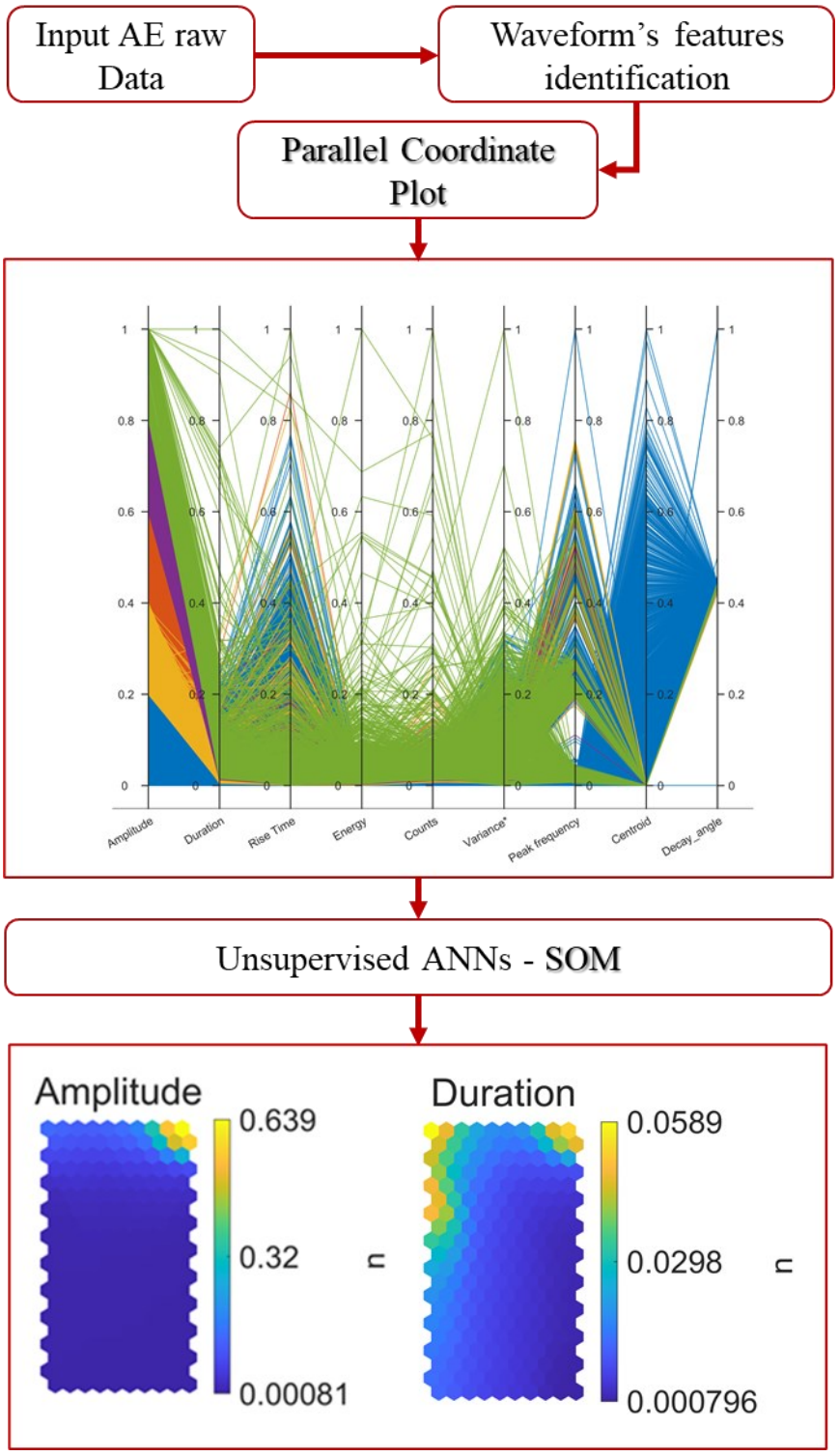

Figure 70 - Process for the recognition of the parameters of the reference sample

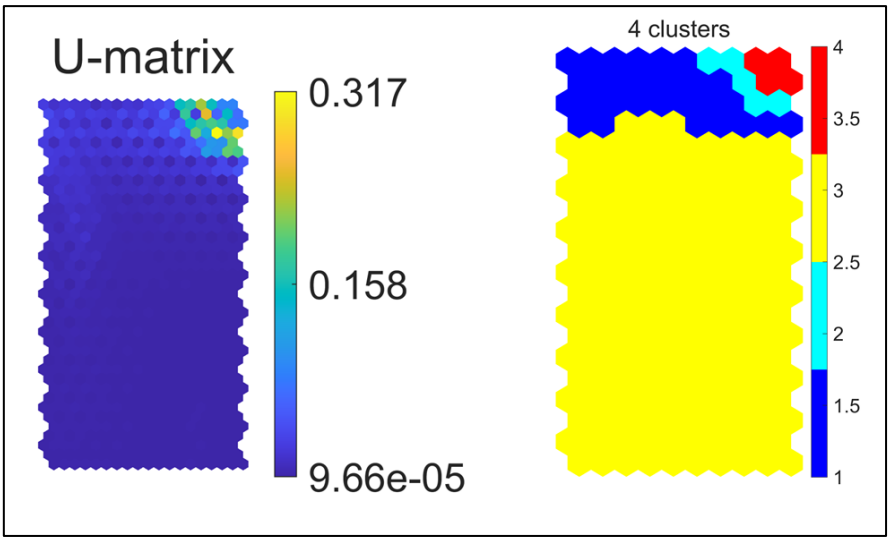

Figure 71 - Original and clustered U-matrix of the reference sample

3.3.1.2 AE DAMAGE EVOLUTION PATTERN

Evaluating the indexing criteria determined the optimal number of clusters be 4. Subsequently, the K-means-based algorithm, i.e., SOM, was applied and, using the quadratic error minimization process [95], created the 4 clusters (Fig.71).

In Fig. 72, the dispersion of the AE events according to amplitude per cluster is shown. Based on the amplitude ranges and the literature, it is possible to associate each cluster with a damage type. Furthermore, the accumulated energy per cluster was graphed together to evaluate the damage even better as a function of the test trend.

Fig. 72 shows that each cluster presents different trends and energy levels reached during the test. In addition, it was known that damage within structures produces clusters with different energy levels. On the other hand, background noise produces waves with lower energy levels that are constant over time.

Further assessments of the type of physical damage of each cluster are made by analysing the morphology of each shape. In Fig. 73, the individual waveforms are grouped, and it can be seen that cluster number 1 has continuous waveforms. This required an additional step of filtering out the background noise.

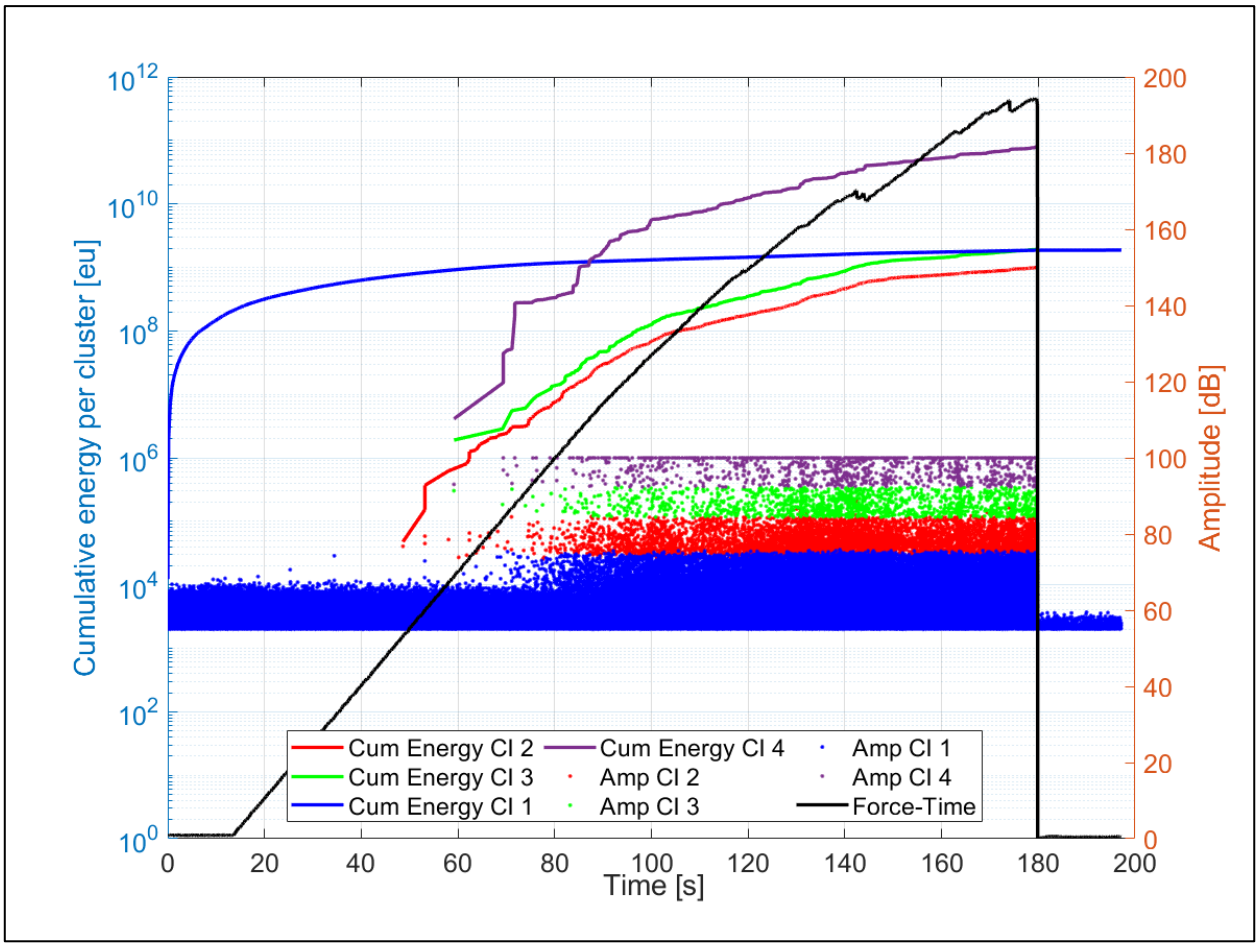

Figure 72 - AE event groups cumulative for each raw cluster data

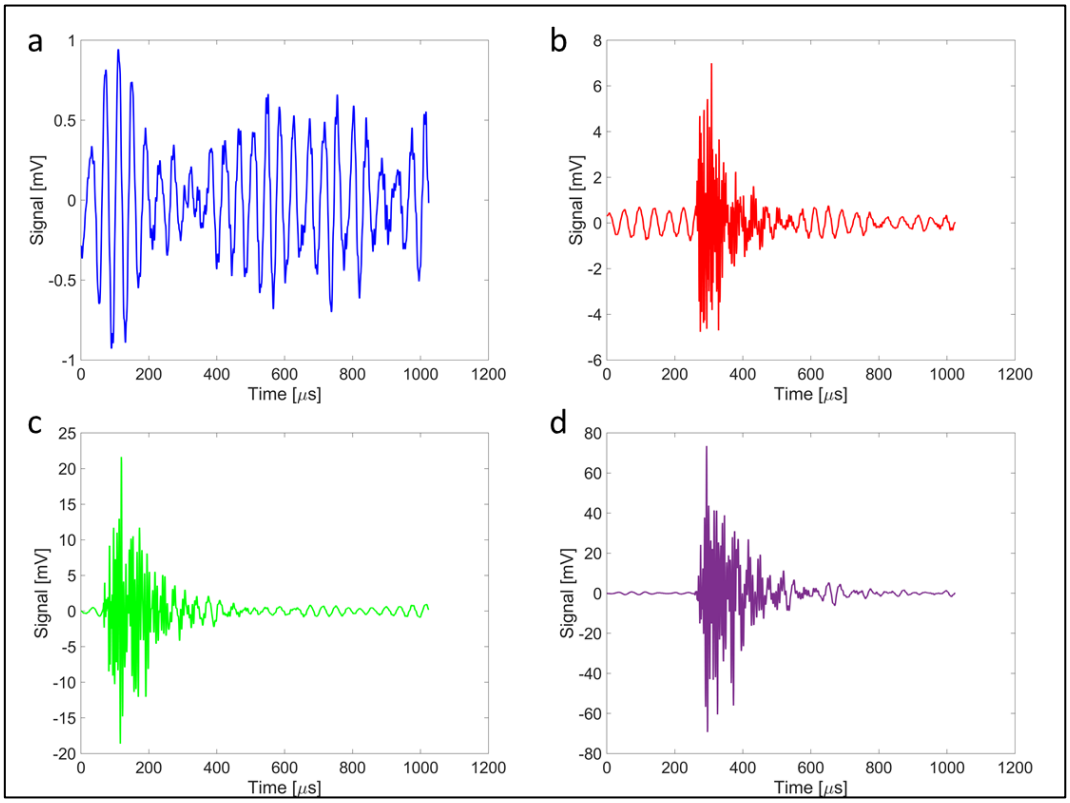

Figure 73 - Representative waveforms of each cluster a) Cluster 1, b) Cluster 2, c) Cluster 3, d) Cluster 4

Therefore, a new specimen was placed under a zero load for approximately 500 seconds to discern the presence of background noise. The visual analysis of the waveforms below the 65dB amplitude, shown in Fig.74, contains continuous waves related to noise from the test machine.

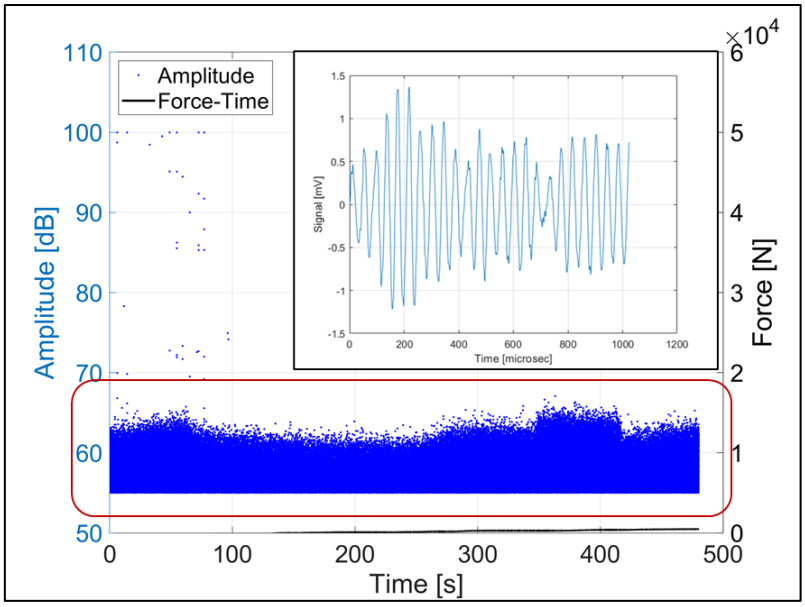

Figure 74 - AE events of pencil-lead brake under zero loading with a representative waveform of the domain

So as in [96, 97], It was decided to remove all events below 65dB from the AE dataset.

The application of this filter made it possible, as shown in Tab.10, to reduce the number of events analysed and reduce the time taken to analyse them.

Table 10 - Data analysed after removing the noise

Samples		*CL1*	*CL2*	*CL3*	*CL4*	*Tot events after filter*	*Tot events*
1	*# Hits*	13334	7840	2105	1491	24770	180368
	# Hits [%]	53.83	31.65	8.50	6.02	13.73	100
2	*# Hits*	10963	5874	1875	1747	20459	195290
	# Hits [%]	53.59	28.71	9.16	8.54	10.48	100
3	*# Hits*	14210	9162	2776	2115	28263	155207
	# Hits [%]	50.28	32.42	9.82	7.48	18.21	100
4	*# Hits*	7132	4049	1461	1412	14054	120483
	# Hits [%]	50.75	28.81	10.40	10.05	11.66	100
5	*# Hits*	15346	9495	2889	2222	29952	148955
	# Hits [%]	51.24	31.70	9.65	7.42	20.11	100

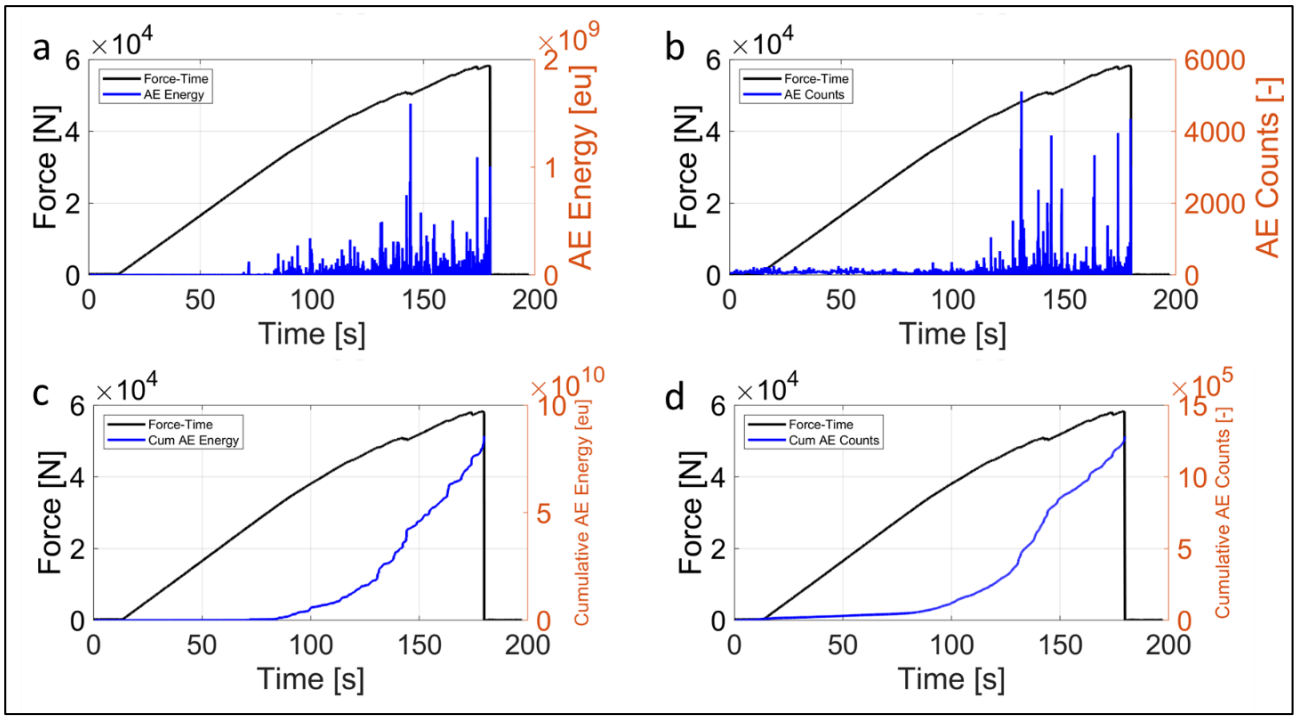

Figure 75 – AE events response for reference specimen a) peak energy-time, b) counts-time, c) cumulative energy-time, d) cumulative counts

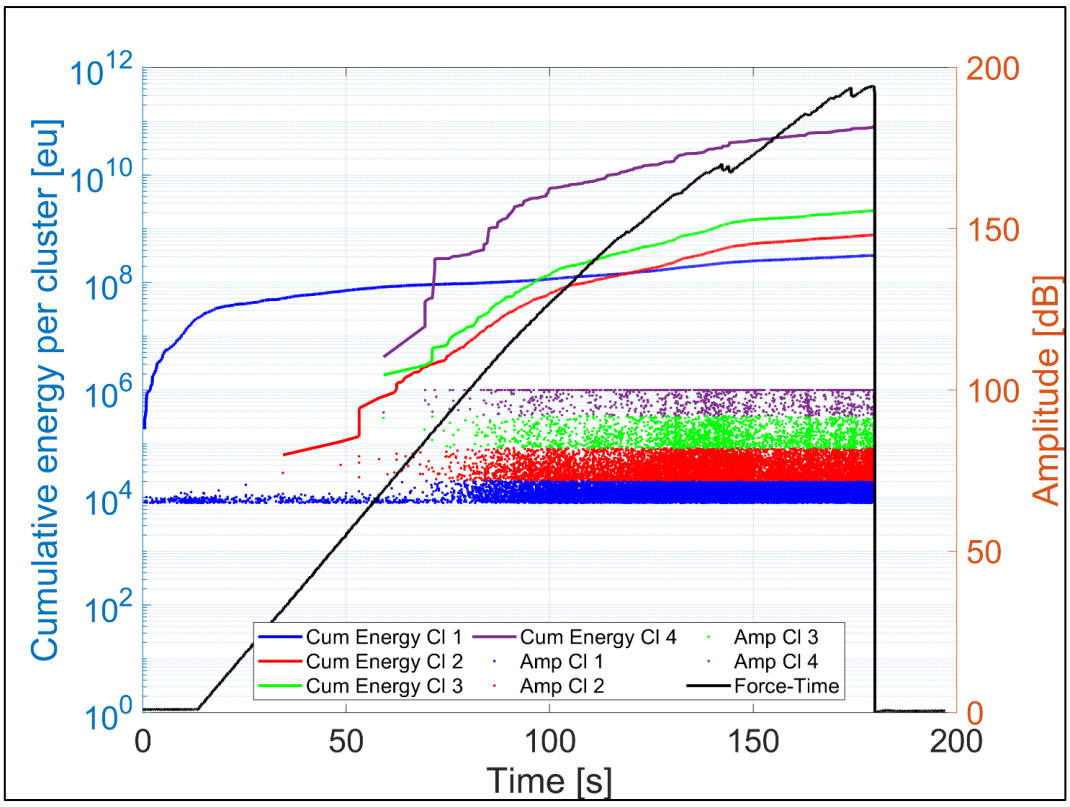

Figure 76 -Cumulative AE energy for each cluster and AE amplitude clustering result after filtering

Next, the waveforms of cluster one were evaluated. Fig.76 shows us the new waveform present in cluster one.

Table 11 shows some parameters found for each cluster that help better understand the type of damage referred to each cluster. Instead, in Tab.12, it is possible to notice the number of events present in each cluster and their percentage on the total after applying the filter. Moreover, it can be appreciated that the reduction of the events obtained after removing the background noise has been remarkable, and the total number of analysed waveforms has been drastically reduced up to about 13%. The clusters considered after filtering can also be associated with a type of damage because, as seen from the waveforms in Fig. 73 a-b-c and Fig. 76, they are mainly formed by burst waveforms. As explained in the background section, burst waves are associated with a type of damage evolution. As can be easily seen, the signal achieved by each waveform varies as the cluster varies, with a higher signal for cluster four (Fig 73d) up to cluster one (Fig.76).

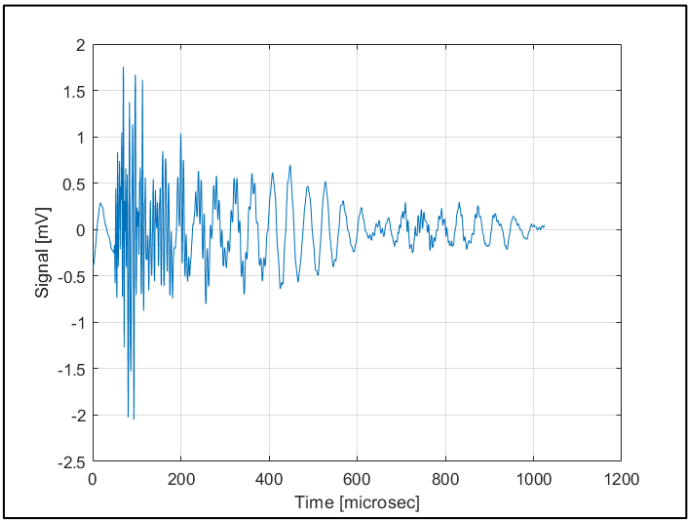

Figure 77 - New representative waveforms of cluster one

Table 11 - Parameter values per cluster

#Cluster	*CL1*	*CL2*	*CL3*	*CL4*
Ampl_min [dB]	65	72	82	92
Ampl_avg [dB]	68	76	86	98
Ampl_max [dB]	72	82	92	100
Energy_min [eu]	1.65E+03	7.43E+03	7.59E+04	1.21E+06
Energy_avg [eu]	2.41E+04	9.98E+04	1.05E+06	5.53E+07
Energy_max [eu]	6.14E+05	2.34E+06	1.70E+07	1.59E+09
Duration_min [µs]	27.3	99	206	335
Duration_avg [µs]	624.0168	793	1425	3371
Duration_max [µs]	12550.9	10285	16582	51384
RT_min [µs]	1	1	3	2
RT_avg [µs]	230	230	396	533
RT_max [µs]	9039	6903	10315	12450

Table 12 - Events for each cluster

#Cluster	*CL1*	*CL2*	*CL3*	*CL4*	*Tot events after filtering*	*Tot events*
# Hits	13334	7840	2105	1491	24770	180368
# Hits [%]	53.83	31.65	8.50	6.02	13.73	100

The test can be divided into two stages. In the initial instants up to 60/70s, there is an accumulation of energy, counts and low amplitude signals. The next part is characterised by the presence of all the damage involved in the structure. Fig.75 shows us the general behaviour of the test, and it can be seen that the energy and the number of events present and, finally, the signal from the AE is small (Fig 76). This roughly corresponds to the behaviour associated with deformation in a linear field. The mechanical properties of the sample are stable at a few signals. The damage begins to develop more intensely towards 70s after the start of the test. Around 120/130s there is a sharp increase in the accumulation of energy and consequently in the number of counts accumulated until, after successive jumps in the energy released, the specimen failure occurs.

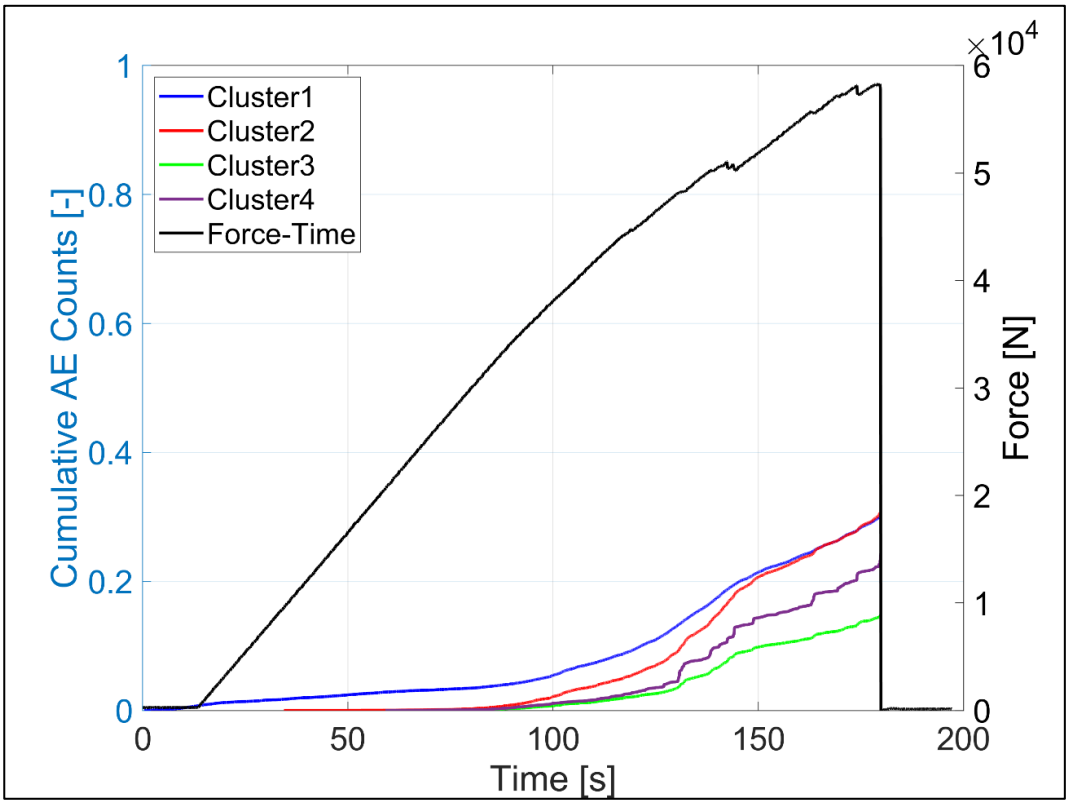

Figure 78 - Cumulative AE counts of each cluster normalised to the maximum counts during the tensile test of the reference sample

In detail, the trends of accumulated energy and cumulative counts per cluster, respectively, in the graphs in Figures 76 and 78, help us better understand the development of the various damages involved. As far as cluster 1 is concerned, both figures show the presence of its activity since the first

moments of the test, with an accumulation of energy and counts. Subsequently, in the second phase of the test, i.e., after 60/70s, damages from the three remaining clusters start to be noticed.

Then there is a continuous existence of the main damage by cluster one, which then develops to the remaining three. Considering Tab.11 and precisely the amplitude intervals in which the different clusters act, it suggests that the first cluster can be associated with the matrix cracks [75] and is within the 65-72dB [75] amplitude range. As noted by [98], increasing load cracks arise at the longitudinal and transverse fibre/matrix interface with amplitudes in the 72-82dB range. With the slight increase in load and the growth of the first two damage clusters, stress is placed on the fibres, which begin to break. The fibre break is 82-92dB [75, 98]. The last cluster, i.e., the four with the sharpest energy release and activities that follow almost the same test trend, is a delamination phenomenon (92-100dB) [74, 99]. Javalal et al. [87, 88] note that the instantaneous load drop heralds a delamination phenomenon and, therefore, a failure.

The substantial difference between clusters three and four is also due to two reference parameters of the respective clusters, namely the duration and the average rise time of each, which can be seen in Tab.10. Therefore, by comparing the two average values, it can be seen that the duration and the rise time of cluster four are longer than that of cluster three. Yuris et al. [80] suggest that damage due to delamination has a longer duration than fibre failure. On the other hand, [81], claims that the rise time in fibre failure is low.

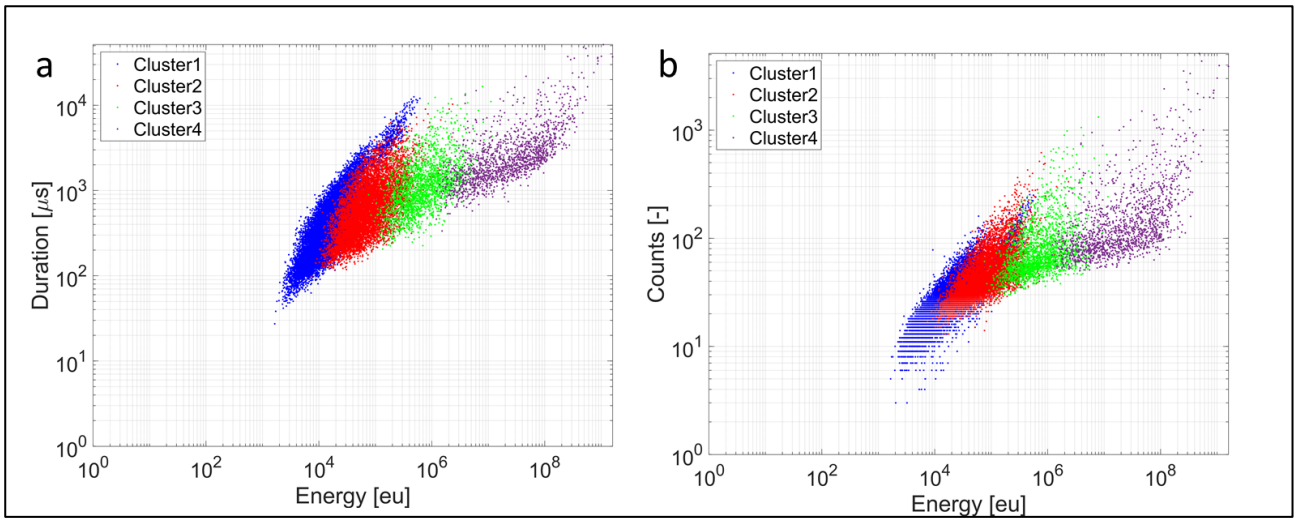

Figure 79 - Comparison between a) the energy released and the duration, b) the energy released and the number of counts per event for each cluster

Fig. 79 shows that the duration and counts increase as the energy release increases. Concerning the duration of cluster four, the phenomena associated with delamination develop with

high durations and, consequently, high counts. It can be seen that the minimum duration increases and, in addition, events with a minimum duration already release higher levels of energy.

3.3.1.3 DIC DAMAGE EVOLUTION PATTERN

The images shown in Fig. 80 refer to the deformation developed along the longitudinal axis of the test specimen. Therefore, the strain field obtained from the analysis of the images taken with the DIC, in Fig. 80, shows us the evolution of the longitudinal strain distribution of the first lamina during the test. At low loads, around 25% of the test, a local strain concentration arises at the carbon/kevlar (C/K) interface (Fig. 80a). The resulting increase in load causes transverse cracking and subsequent detachment of the C/K interface. From this point onwards, the load is completely transferred to the carbon at the sides of the insert. As the test continues, the concentration of deformations moves to the corners of the C/K interface (Fig.80d).

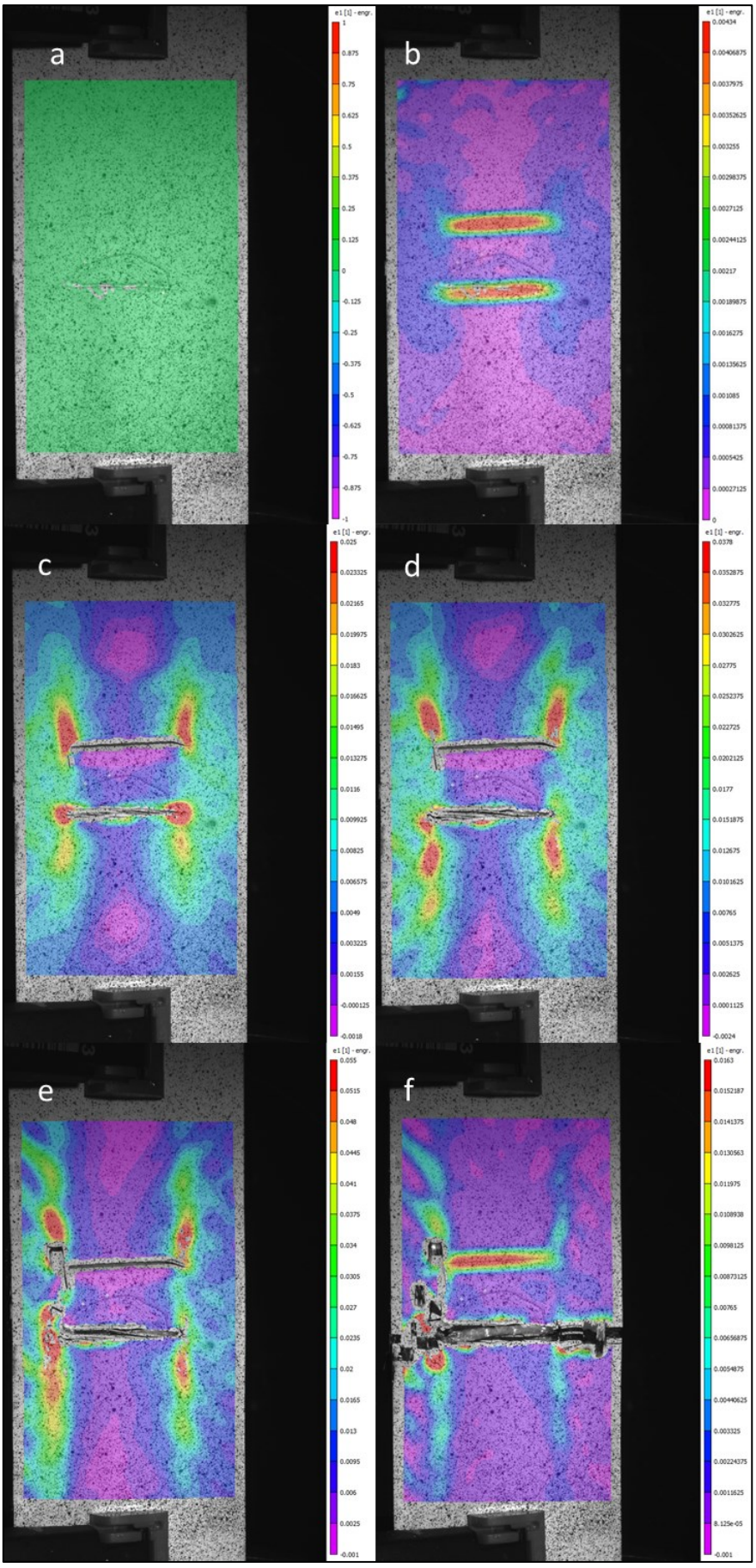

Figure 80 - Strain field acquired with DIC at force levels: a) 0 kN, b)15kN, c)36kN, d)50kN, e)58kN, f) after failure.

In the last stages of the test, noticeable damage due to fibre brake along the areas at more significant deformation is evaluated (Fig. 80 d-e). Fig. 80f is the instant of failure of the specimen where the clean-break of the carbon fibres along the sections outside the Kevlar window and the complete detachment of the C/K interface can be seen.

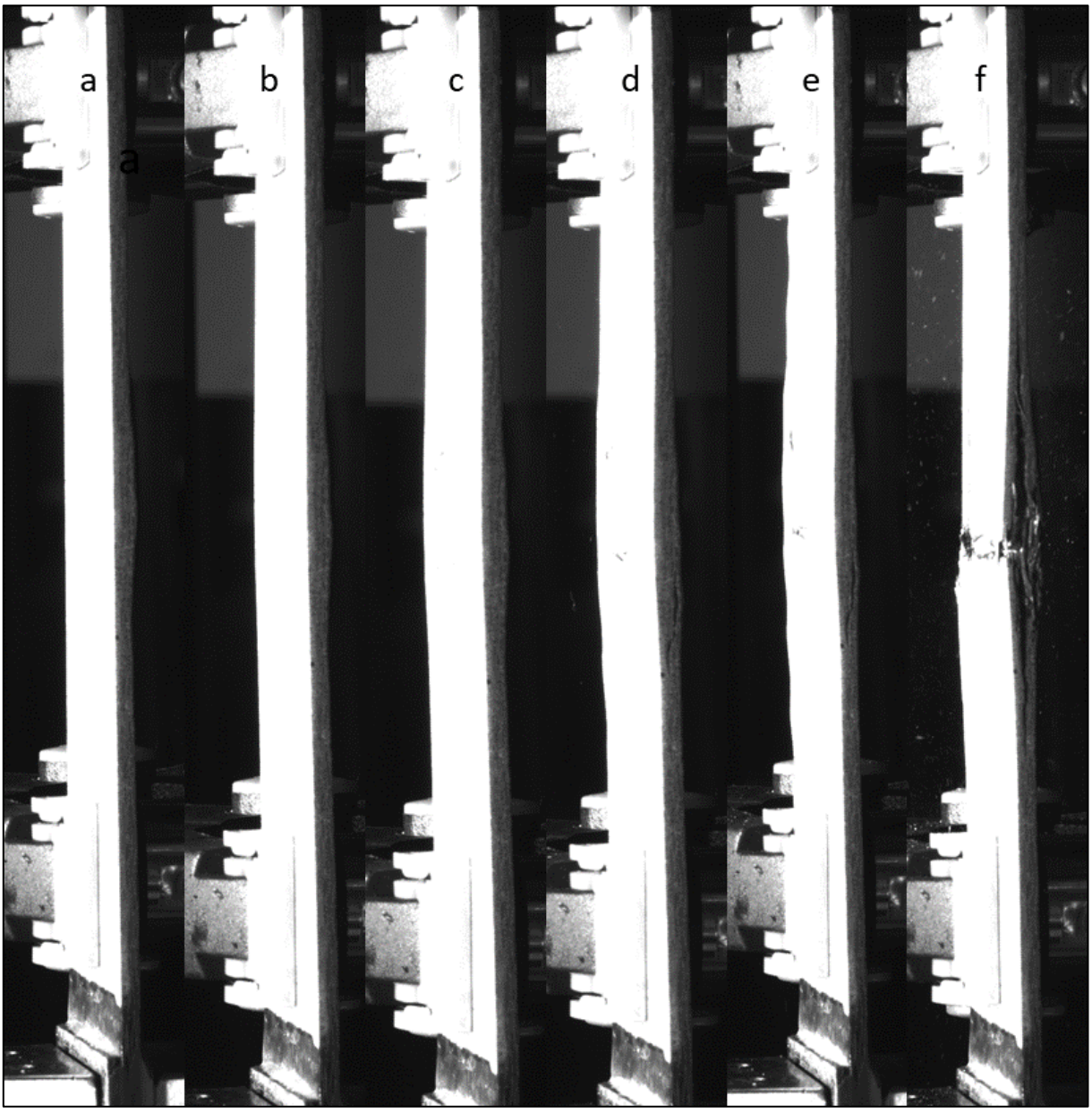

Figure 81 - Photo of the side of the sample at force levels: a) 0kN, b)15kN, c)36kN, d)50kN, e)58kN, d) after failure.

Fig.81 shows us various shots taken with the lateral camera during the entire left test of the specimen, as seen in the methodology section. As far as the reference specimen is concerned, on the other hand, it is immediately apparent that the damage due to delamination manifests itself externally in the final phases of the test. Fig.81d shows how the delamination reaches both sides; in detail, a slight swelling can be seen on the opposite side in the test specimen's lower part, which subsequently

propagates (Fig. 81e). The same reasoning but in a much more obvious way can be seen in Fig.80d, where cracking of the side of the specimen between the two front and rear layers can be seen, remaining constant until an instant before the failure, where a remarkable propagation in both longitudinal directions of the specimen can be seen, as shown in Fig.81f.

3.3.1.4 C-SCAN DAMAGE EVOLUTION PATTERN

Finally, Fig.82a and b show the damage explained above with DIC and side camera, respectively. Furthermore, Fig. 82c shows us the scan obtained at the end of the test with the C-scan. This shows the propagation over the whole area where the delamination insert is present.

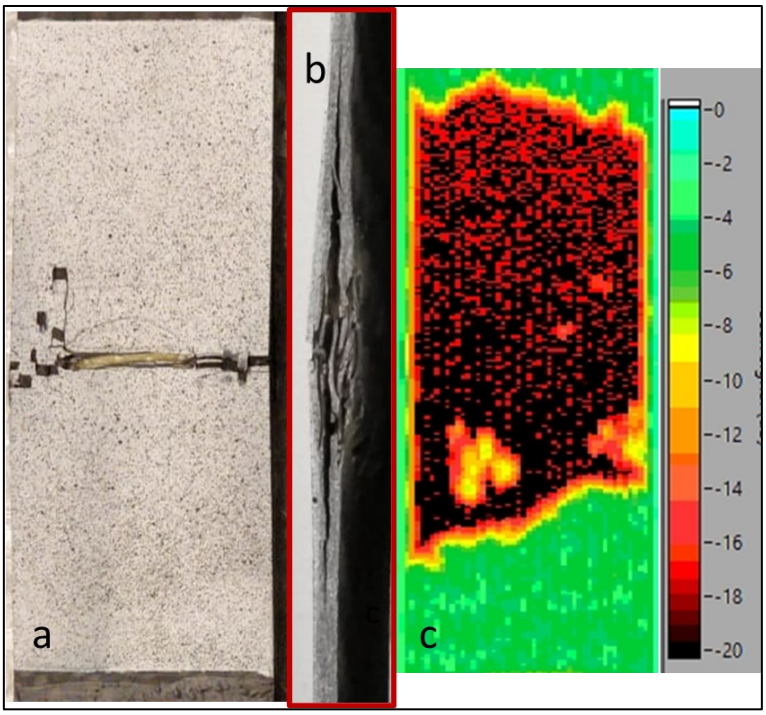

Figure 82 - Reference sample after breakage a) front view, b) side view, c) C-Scan

So, to conclude the section on quasi-static testing, we can say that the use of visual monitoring tools such as DIC, lateral camera and C-scan allowed us to validate the damage illustrated with the AEs (Tab.13) visually but did not allow us to fully understand the parts affected by the damage during the test.

Table 13 - Type of damage of each cluster

	CL1	*CL2*	*CL3*	*CL4*
Amplitude range [dB]	65-72	72-82	82-92	92-100
Type of damage	Matrix-crack	f/m interface	Fibre failure	Delamination

Therefore, in the next section, quasi-static tests will be exposed based on the data obtained from the previous ones.

It was decided to divide the test interval into several ramps reaching certain load levels. Furthermore, knowing the damages involved and the amplitude ranges in which they evolve, it was decided to keep them constant for all ramps.

3.3.2 INTERRUPTED TENSILE TESTS

The interval of each ramp was divided according to the average maximum load found by the quasi-static tests. The entire test was first divided into five intervals, i.e., every 11kN until the sample broke. However, when analysing C-scan images at first, it was noted that delamination damage occurred noticeably in the final moments before the failure. Therefore, it was decided to include a different interval in the region of 50kN, i.e., just before the specimen breaks. As we shall see in the results, it allowed a better resolution of the growth of damage to the specimen, specifically delamination.

Moreover, the data analysis obtained with the AEs of the quasi-static tests subdivided by ramps kept the previously found cluster intervals unchanged. The procedure was adopted because, as seen in the tests set out above, all types of damage are present from the low loads of the test.

Therefore, assessing the damage growth within the studied specimen will be better.

For simplicity, the results obtained from one specimen will be shown, but the procedure was used the same way for the rest.

The tensile test to failure of the single specimen was divided into six intervals: 11kN, 22kN, 33kN, 44kN, 50kN and failure load.

The general evolution of the specimen will not be explained, but step by step, the impactful effect of the individual damage will be seen for each ramp carried out.

3.3.2.1 AE DAMAGE EVOLUTION PATTERN

As mentioned above, the range of clusters remained the same, as shown in Table 11. Instead, it is interesting to understand the activity of each cluster per ramp level after noise removal. Table 14 summarises the number and percentage of AE hits for each cluster and ramp. Moreover, the percentage of events studied after removing noise-related events is present. Note that the most significant number of events is during ramp 5, at loads close to the sample failure.

In Tab.15-16, the values of some fundamental parameters for every cluster and every studied ramp are shown, that they help better to understand the presence and the type of damage.

Table 14 - Events for each cluster per ramps

Ramp#		*CL1*	*CL2*	*CL3*	*CL4*	*Tot events after filtering*	*Total events*
Ramp_1	*# Hits*	329	198	84	88	699	82793
	# Hits [%]	47.07	28.33	12.02	12.59	0.84	100
Ramp_2	*# Hits*	1024	589	206	220	2039	137287
	# Hits [%]	50.22	28.89	10.10	10.79	1.49	100
Ramp_3	*# Hits*	835	508	183	223	1749	204781
	# Hits [%]	47.74	29.05	10.46	12.75	0.85	100
Ramp_4	*# Hits*	3080	1168	366	347	4961	206853
	# Hits [%]	62.08	23.54	7.38	6.99	2.4	100
Ramp_5	*# Hits*	9999	2067	526	349	12941	180470
	# Hits [%]	77.27	15.97	4.06	2.70	7.17	100
Ramp_6	*# Hits*	5203	2892	826	531	9452	156426
	# Hits [%]	55.05	30.6	8.74	5.62	6.04	100

Table 15 - Parameter values per cluster for ramp: 1-2-3

	#Cluster	*CL1*	*CL2*	*CL3*	*CL4*
	Ampl_min [dB]	65	72	82	92
	Ampl_avg [dB]	68	76	86	98
	Ampl_max [dB]	72	82	92	100
Ramp 1	*Energy_min [eu]*	3.37E+03	1.33E+04	1.15E+05	1.56E+06
	Energy_avg [eu]	3.51E+04	9.05E+04	7.24E+05	4.27E+07
	Energy_max [eu]	2.00E+05	5.25E+05	2.98E+06	1.43E+08
	Duration_min [µs]	77	124	211	452
	Duration_avg [µs]	852	776	854	2093
	Duration_max [µs]	4617	5573	3111	5928
	RT_min [µs]	3	5	8	3
	RT_avg [µs]	358	245	173	168
	RT_max [µs]	3229	2708	1719	2970
Ramp 2	*Energy_min [eu]*	2.71E+03	1.46E+04	1.31E+05	1.17E+06
	Energy_avg [eu]	2.73E+04	9.67E+04	7.93E+05	4.46E+07
	Energy_max [eu]	1.48E+05	5.08E+05	3.52E+06	2.70E+08
	Duration_min [µs]	75	130	220	589
	Duration_avg [µs]	783	931	1171	2305
	Duration_max [µs]	4805	5829	9423	12191
	RT_min [µs]	4	4	6	3
	RT_avg [µs]	299	305	323	271
	RT_max [µs]	4609	4036	4873	3558
Ramp 3	*Energy_min [eu]*	2.72E+03	1.25E+04	1.98E+05	1.36E+06
	Energy_avg [eu]	1.65E+04	9.19E+04	9.01E+05	3.31E+07
	Energy_max [eu]	8.15E+04	4.18E+05	5.04E+06	1.75E+08
	Duration_min [µs]	63	116	195	483
	Duration_avg [µs]	407	618	893	1767
	Duration_max [µs]	2610	4048	2644	6099
	RT_min [µs]	2	4	6	4
	RT_avg [µs]	125	156	163	171
	RT_max [µs]	1351	3333	1406	3409

Table 16 - Parameter values per cluster for ramp: 4-5-6

	#Cluster	CL1	CL2	CL3	CL4
Ramp 4	Energy_min [eu]	2.19E+03	9.58E+03	7.80E+04	1.72E+06
	Energy_avg [eu]	3.89E+04	8.26E+04	9.28E+05	3.63E+07
	Energy_max [eu]	4.26E+05	8.63E+05	7.94E+06	2.67E+08
	Duration_min [µs]	53	90	178	282
	Duration_avg [µs]	913	452	773	1771
	Duration_max [µs]	11310	3383	3453	12536
	RT_min [µs]	1	2	5	3
	RT_avg [µs]	405	102	106	147
	RT_max [µs]	8833	2851	1161	2568
Ramp 5	Energy_min [eu]	1.80E+03	8.92E+03	1.07E+05	1.01E+06
	Energy_avg [eu]	1.00E+05	8.75E+04	8.62E+05	4.12E+07
	Energy_max [eu]	1.01E+06	8.67E+05	6.93E+06	5.48E+08
	Duration_min [µs]	39	84	213	433
	Duration_avg [µs]	2123	705	1233	2811
	Duration_max [µs]	21526	9529	18704	27852
	RT_min [µs]	1	2	4	3
	RT_avg [µs]	1026	208	313	456
	RT_max [µs]	13064	6825	5779	6174
Ramp 6	Energy_min [eu]	1.50E+03	7.99E+03	1.01E+05	1.06E+06
	Energy_avg [eu]	2.46E+04	1.01E+05	1.01E+06	6.39E+07
	Energy_max [eu]	4.27E+05	1.66E+06	1.57E+07	1.43E+09
	Duration_min [µs]	29	102	210	454
	Duration_avg [µs]	644	755	1461	4330
	Duration_max [µs]	12939	7628	20185	103842
	RT_min [µs]	1	1	5	2
	RT_avg [µs]	254	219	383	725
	RT_max [µs]	7578	5516	5650	19326

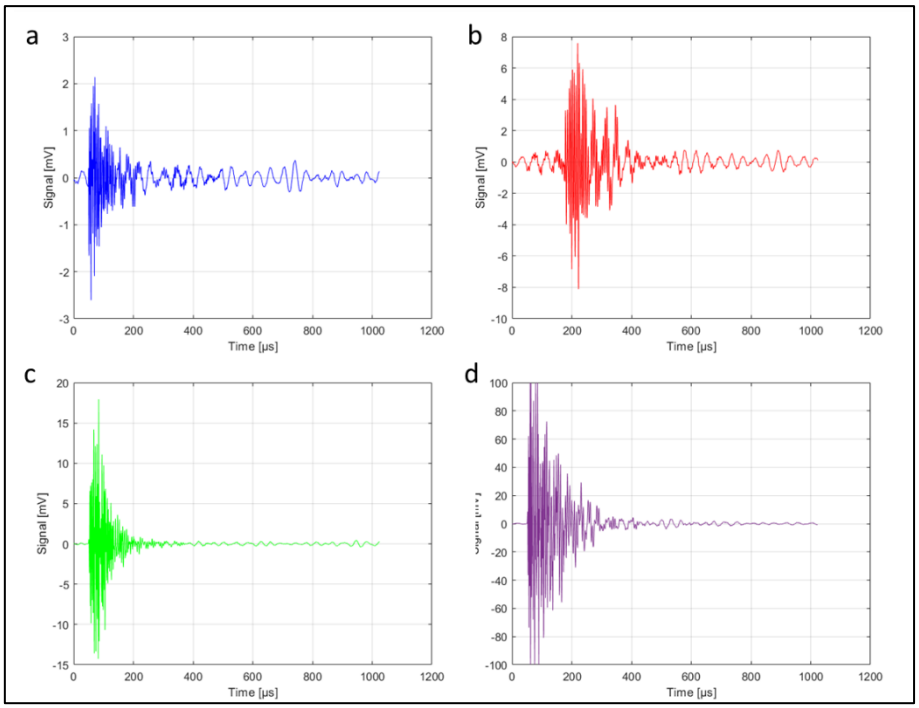

Figure 83 . Representative waveforms of each cluster a) Cluster 1, b) Cluster 2, c) Cluster 3, d) Cluster 4 for ramp 1

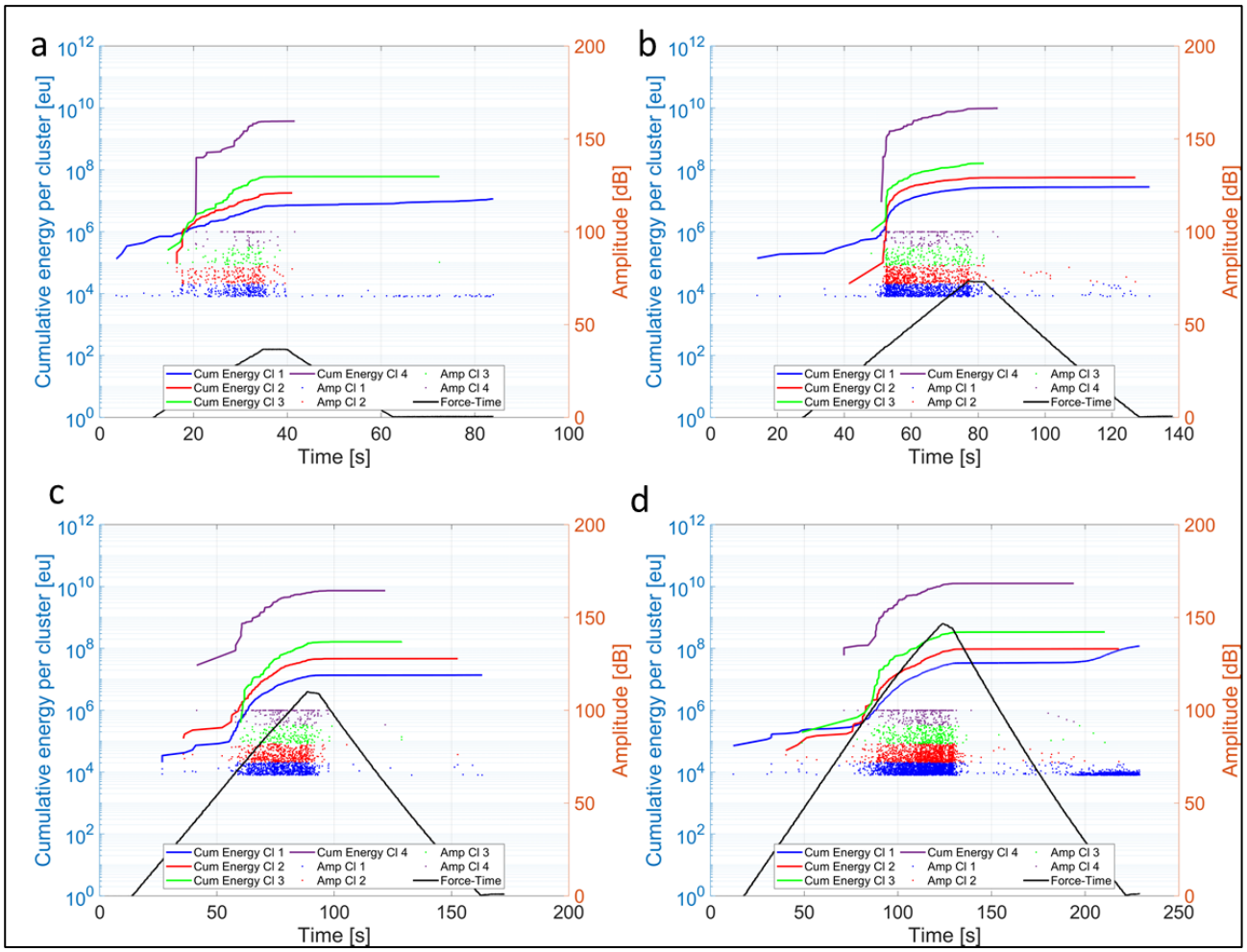

Figure 84 - Cumulative AE energy for each cluster and AE amplitude clustering result after filtering per load level of a)11kN, b)22kN, c)33kN, and d)44kN

From Figs. 84-85, in some ramps, there is an activity from the AEs even during the unloading phase, especially towards the end. As seen in [100], this phenomenon is associable with the push-in fibres phenomenon, which dominates during the unloading phase. The phenomenon is because the tests are in displacement control, so the samples, when arriving at zero displacements, have internally residual stresses, so they are not unloaded and could cause a switch to a compression condition.

This phenomenon is also called the “effective plasticity” of the material and is very common in materials composed of carbon fibre [100].

Fig.83 shows examples of waveforms for each cluster referring to the first ramp.

However, as seen above, it is difficult to determine with certainty when given damage starts. It derives from assumptions that imposed the same intervals obtained in the static case, assuming that all the damages were active since the lowest loads.

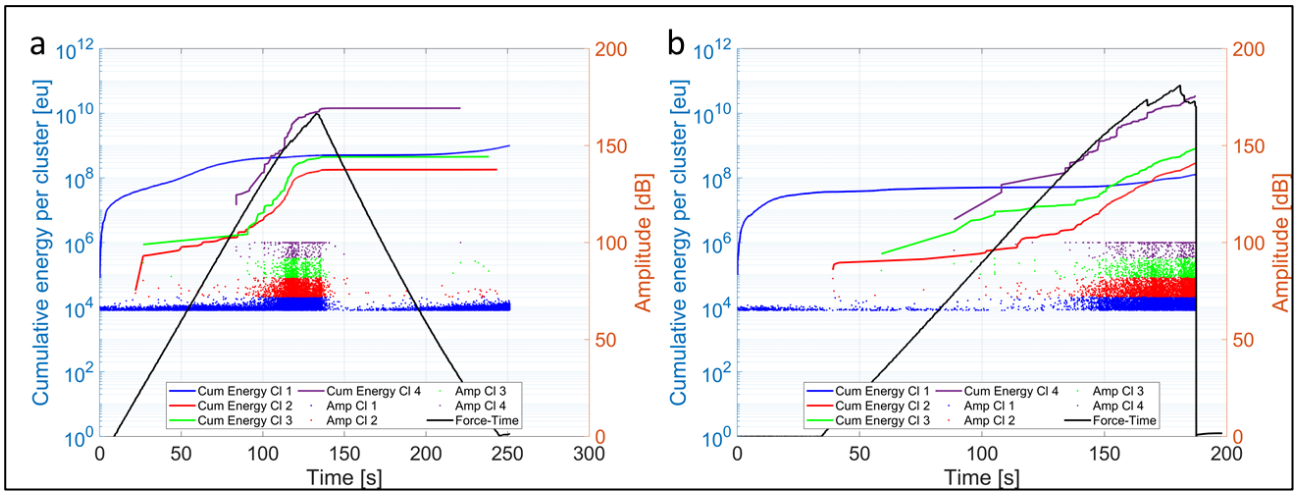

Figure 85 - Cumulative AE energy for each cluster and AE amplitude clustering result after filtering per load level of a)50kN, b) until failure load

Cluster 1, as shown in Tab. 14, again confirms the most significant presence during all ramps.

In Fig.84a-86a, matrix-cracking confirms that the activity starts at the beginning of the test. Subsequently, we see that the other three clusters, 20s begin to accumulate activity.

In the following ramps, it is clear that the activity of the other three clusters starts again as soon as the load reached in the last ramp is reached. The only difference is present in the penultimate ramps (Fig.87a-b), where in the first case, the cumulative matrix-cracking counts increase from the very first moments. This activity can be associated with high matrix cracking since, simultaneously, the knee in the force-time curve is present (a phenomenon that can only be associated with high matrix cracking). Furthermore, it can be seen that its activity starts before any cluster, so it will necessarily be associated with matrix cracking.

Already from the first ramp, in Fig.84a, some events associated with delamination/debonding are present. Its presence can be confirmed by the data shown in Tab.15. Cluster 4 has signals with a longer average duration than cluster 3, even if with a similar RT. This may be due to the presence in cluster 4 of signals due to fiber failure. Moreover, we note that the waveforms in Fig.83c-d are similar to the static case.

In Fig.85b, the energy released during delamination follows the trend of the Force-Time plot. When there is a sudden decrease in load in the subsequent ramps (Fig.85a-b), there is a jump in energy at the delamination cluster.

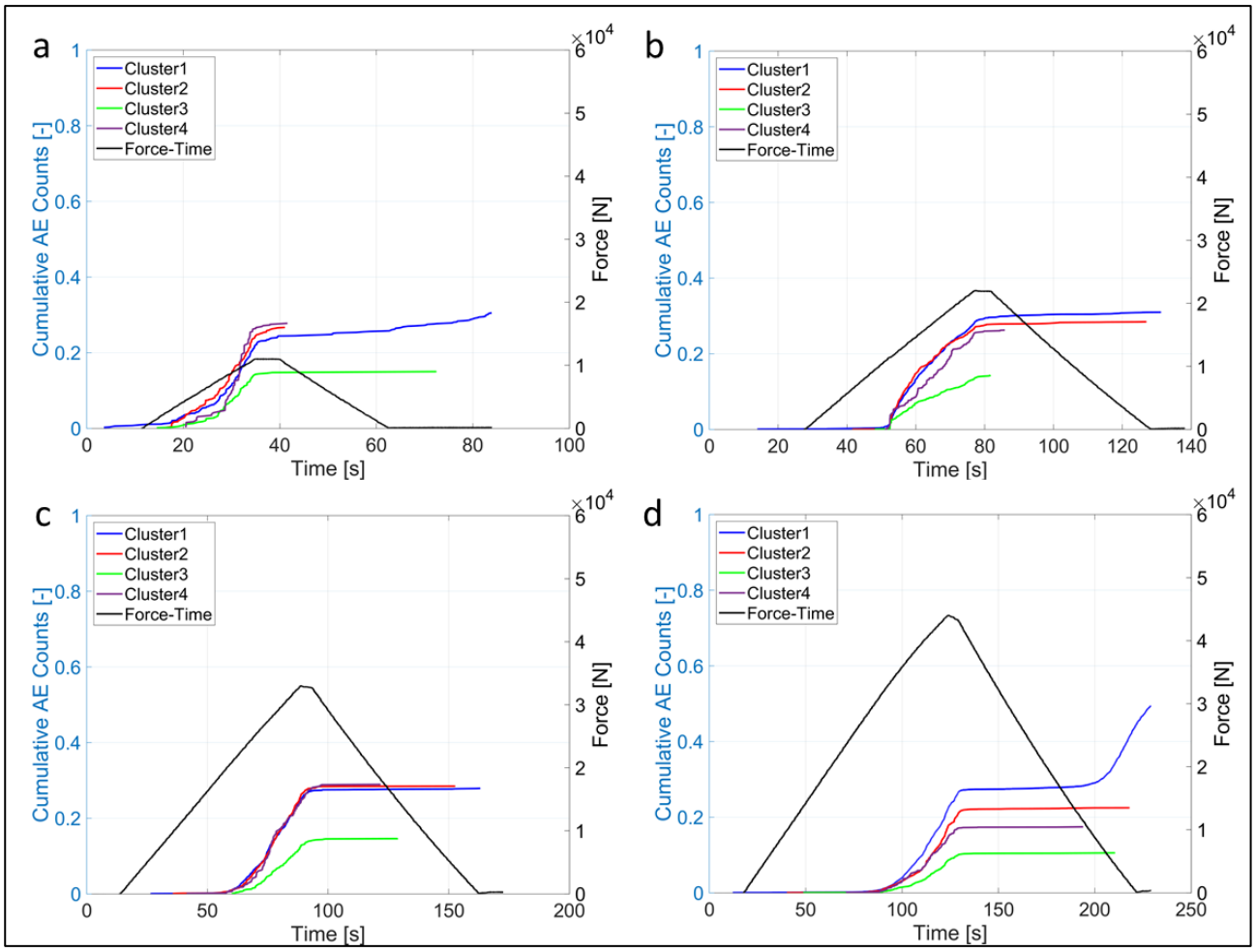

Figure 86 - Cumulative AE counts of each cluster normalised to the maximum counts during the tensile test per load level of a)11kN, b)22kN, c)33kN, d)44kN

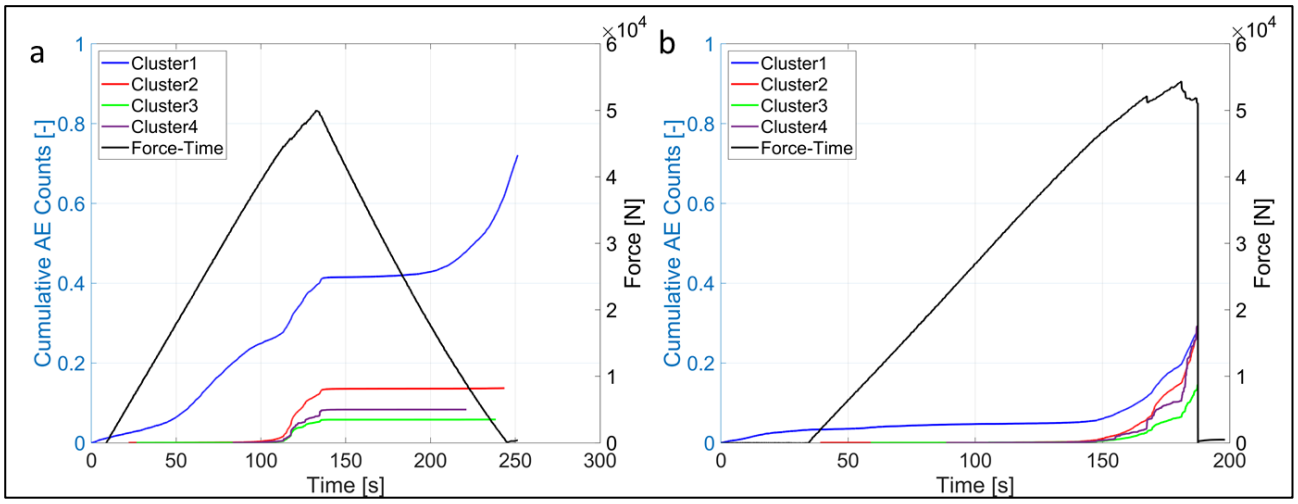

Figure 87 - Cumulative AE counts of each cluster normalised to the maximum counts during the tensile test per load level of a)50kN, b) until failure load

Fig.88 shows, as in the previous section, the relationship between energy vs duration and energy vs counts of the last ramp only. The reduction of current events is related to the fact that, as explained above, they start to accumulate activity again when the load of the previous ramp is

exceeded. It can be seen once again that delamination damage already releases more energy at low durations, and as the phenomenon's duration and counts increase, the energy released increases.

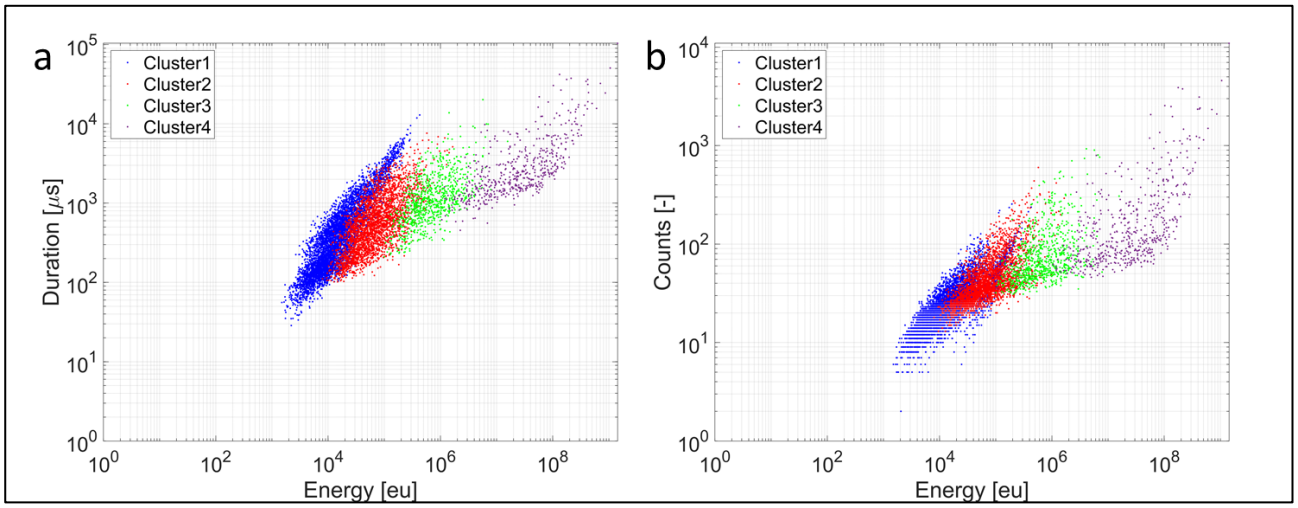

Figure 88 - Comparison between a) the energy released and the duration, b) the energy released, and the number of counts per event for each cluster for the last level of force (until failure)

3.3.2.2 DIC DAMAGE EVOLUTION PATTERN

The activity related to matrix cracking is confirmed at low loads, as shown in Fig.89a, where there is a deformation concentration at the C/K interface (on the edge of the Kevlar window). As the load increases (Fig. 89 b-c-d-e), the gap at the C/K transverse interface at the load gradually increases. Consequently, the concentration of the first-lamina deformations also shifts to the corners, and in particular, Fig 89e succeeds in anticipating the first failure zone of the carbon fibres (Fig.90a). The fibre failure in the ply seen with the DIC is due, as shown in Fig.91, to a movement of the back carbon layers (Back_ply) in an out-of-plane direction creating a flexural movement.

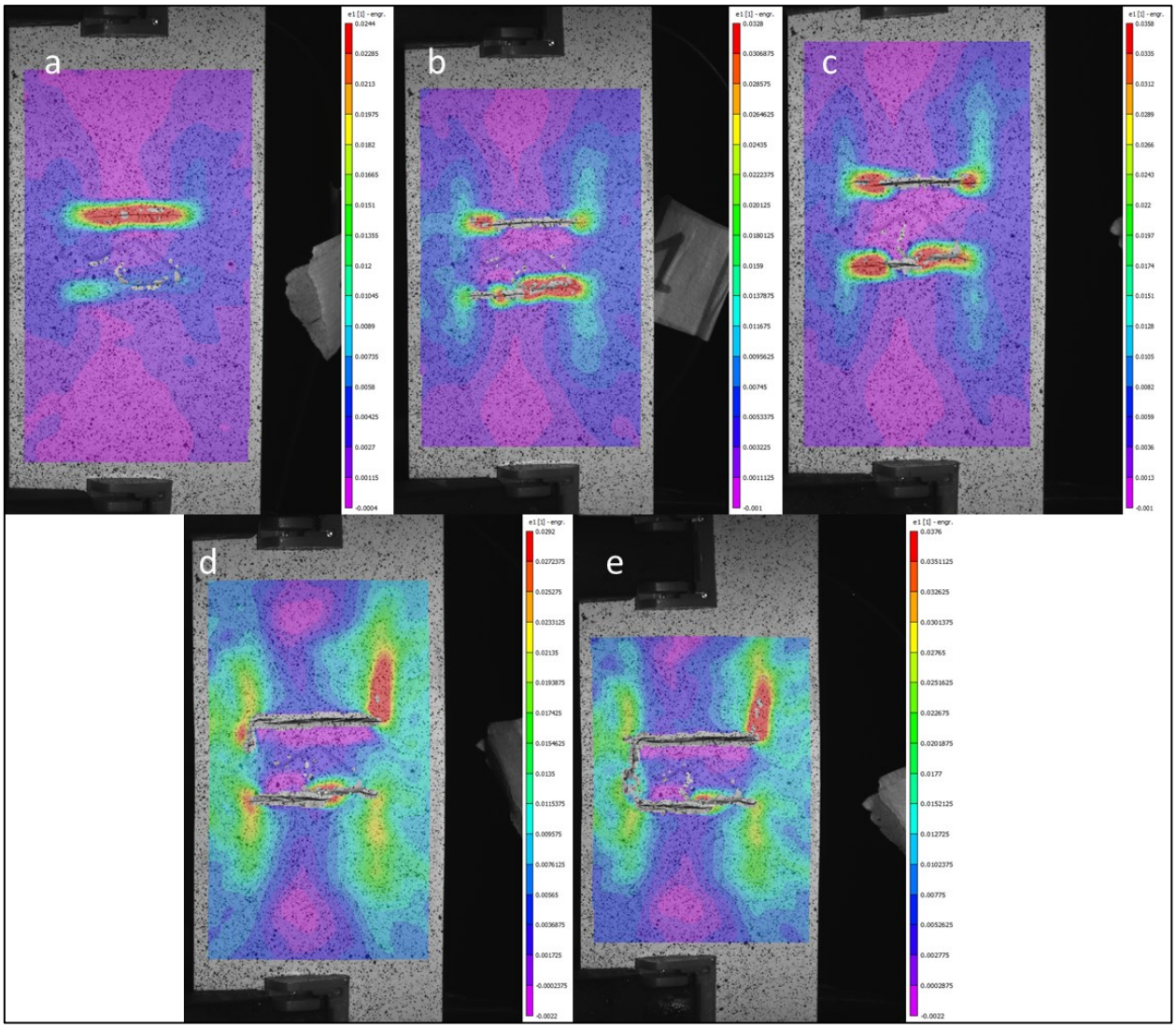

Figure 89 -Strain field acquired with DIC at force levels: a) 11 kN, b)22kN, c)33kN, d)44kN, e)50kN.

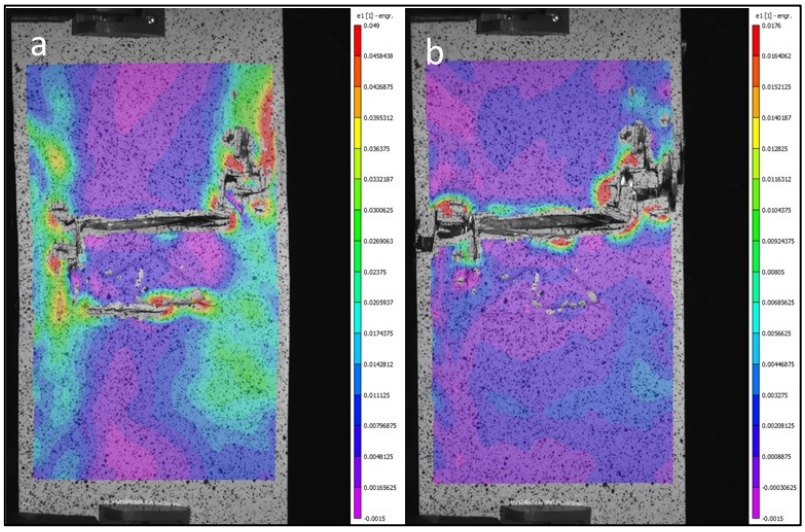

Figure 90 - Strain field acquired with DIC at force levels: a) 54kN, b) after failure load

This may be due to a redistribution of loads, following the detachment of the C/R interface, on the back plies.

In addition, this flexural movement achieved in the latter stages of the test also contributed to the delamination.

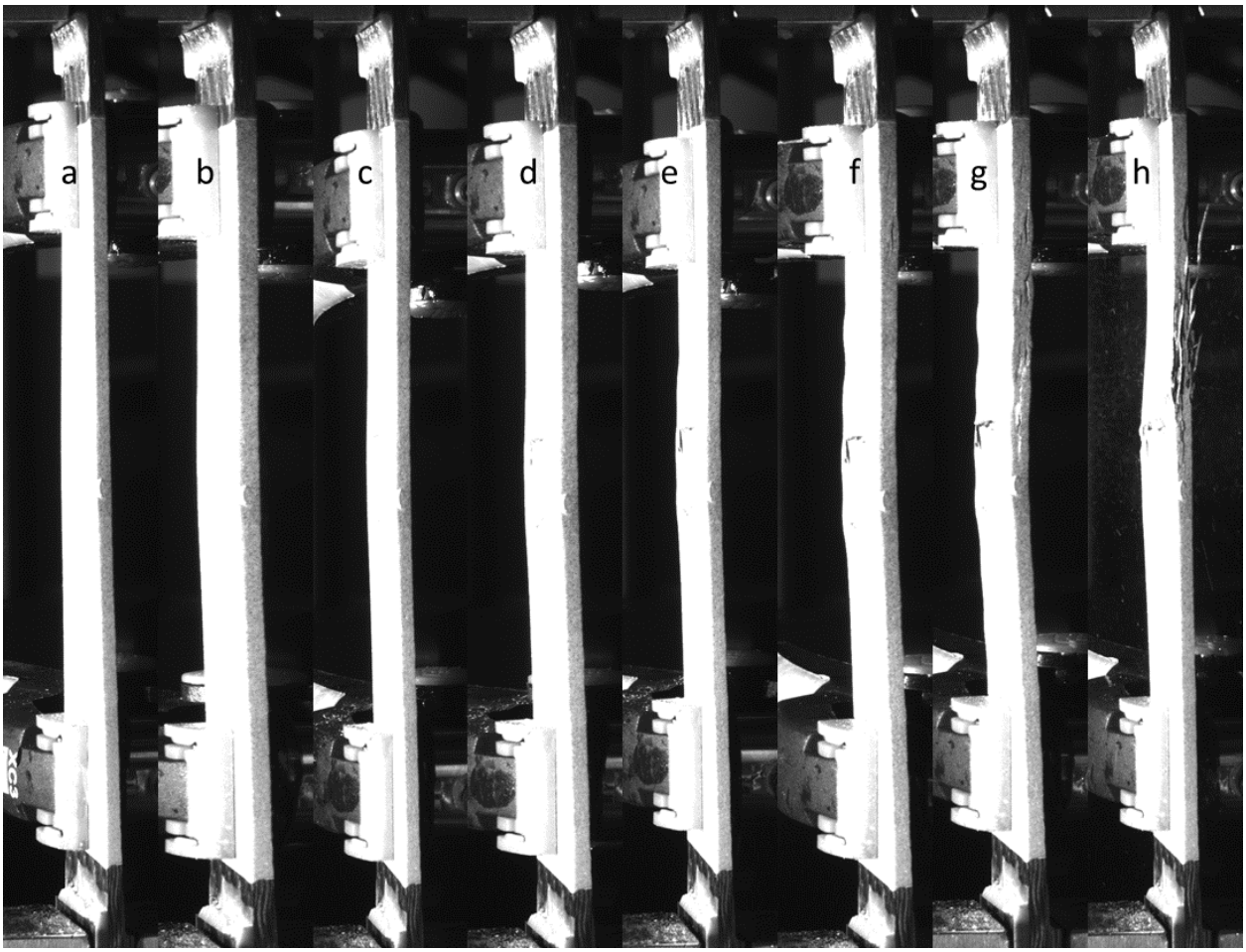

Figure 91 - Photos of the side of the sample at force levels: a) 11kN, b)22kN, c)33kN, d)44kN, e)50kN, f)52kN, g)54kN, h) after failure load.

3.3.2.3 C-SCAN DAMAGE EVOLUTION PATTERN

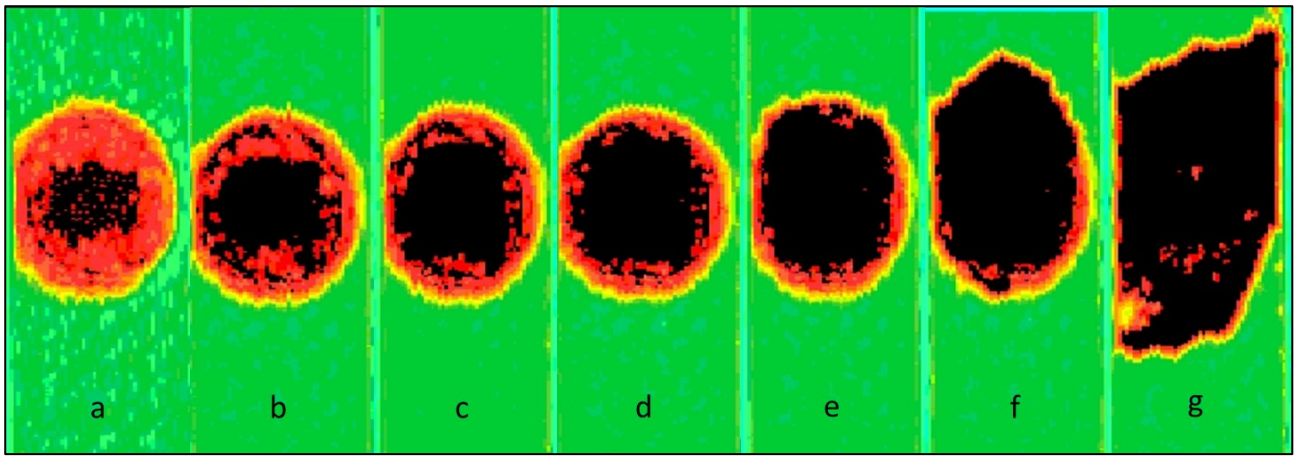

Figure 92 – Pictures gave back from C-scan of the force levels: a)0kN, b)11kN, c)22kN, d)33kN, e)44kN, f)50kN, g) after failure load.

Fig. 92 shows us the evolution of the delamination within our specimen. The C-scan recognises the Roahcell insert and Kevlar patch at zero loads. Subsequently, a localised debonding occurs within the Kevlar patch area as each load step is reached. Upon reaching 44kN, the debonding reaches the edges of the insert. At 50kN, the delamination starts to affect the carbon layers with some small cracks on the edge of the specimen. In fact, at the 50kN ramp (Fig.84a and 86a), a series of small drops in the force-time curve and consequent jumps in the cumulative energy and cumulative counts can be seen.

In Fig.93, the zones of failure of the specimen are shown. In Fig 93b-c, the fiber failure is shown, as in Fig 93d, there is a clear view of the detachment between the two front and rear layers, which led to the delamination.

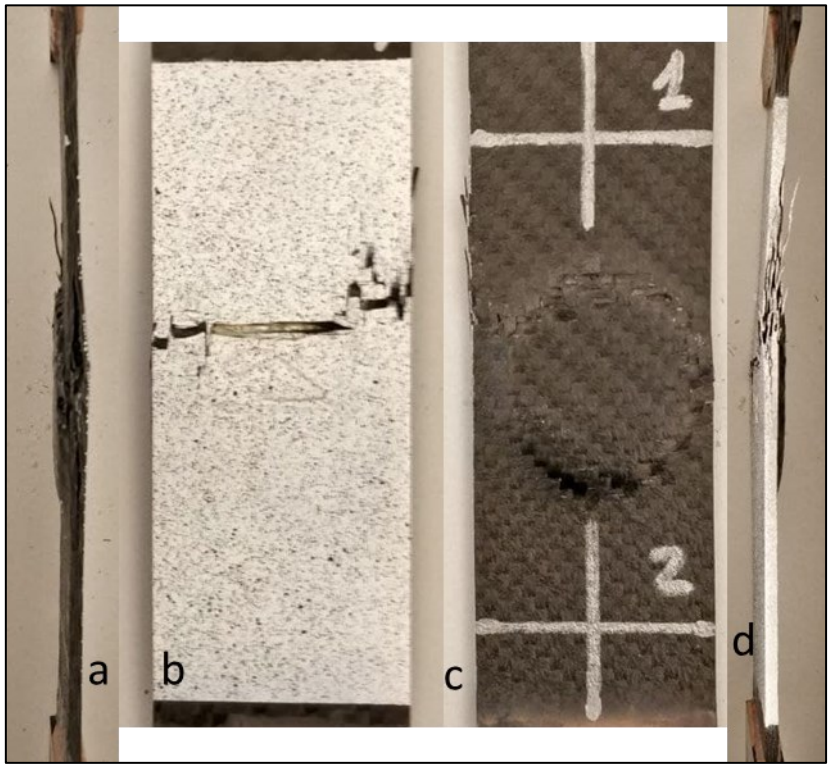

Figure 93 - Reference sample after breakage a) left side view, b) front view, c) back view, d) right side view

To better understand the materials involved in the damage, five specimens were tested again at a constant speed of 1mm/min at loads of 11kN, 22kN, 33kN, 44kN and 50kN. Instead, the reference specimen for the ramps was taken as the specimen for the failure load. Once tested, they were cut (Fig.64a-b) and lapped as explained in the methodology section.

Fig.94 to Fig.105 shows the images taken under the optical microscope for each load level up to failure. Fig.94-99 show the specimens cut in the longitudinal direction of the load (a), while Fig.100-105 show the cuts made along the transverse direction of the load (b).

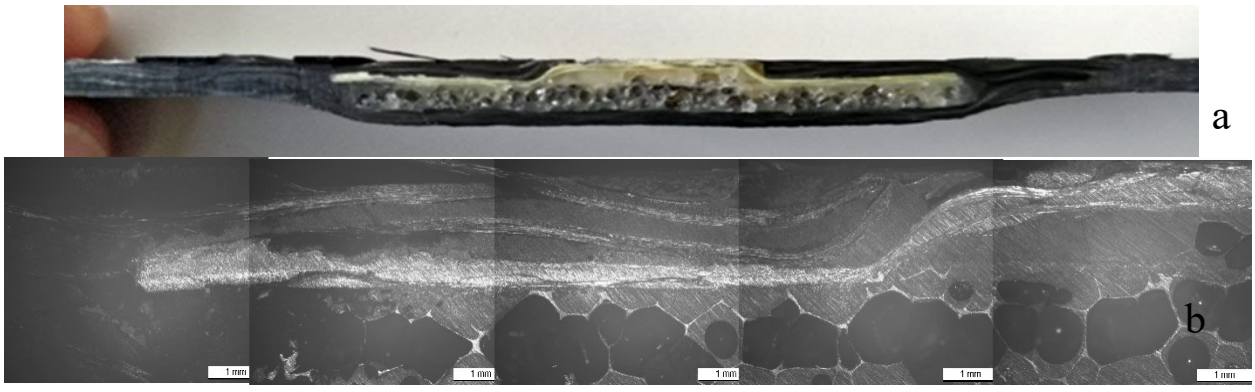

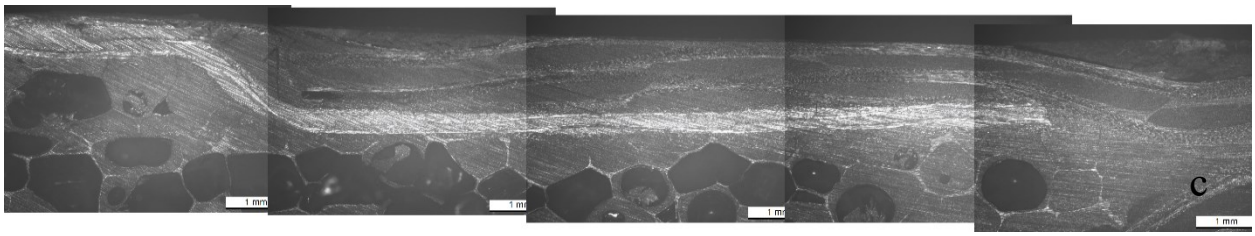

Figure 94 - a) Specimen sectioned along the longitudinal direction at load, b) optical microscope images left section, c) optical microscope images right section at 11kN load

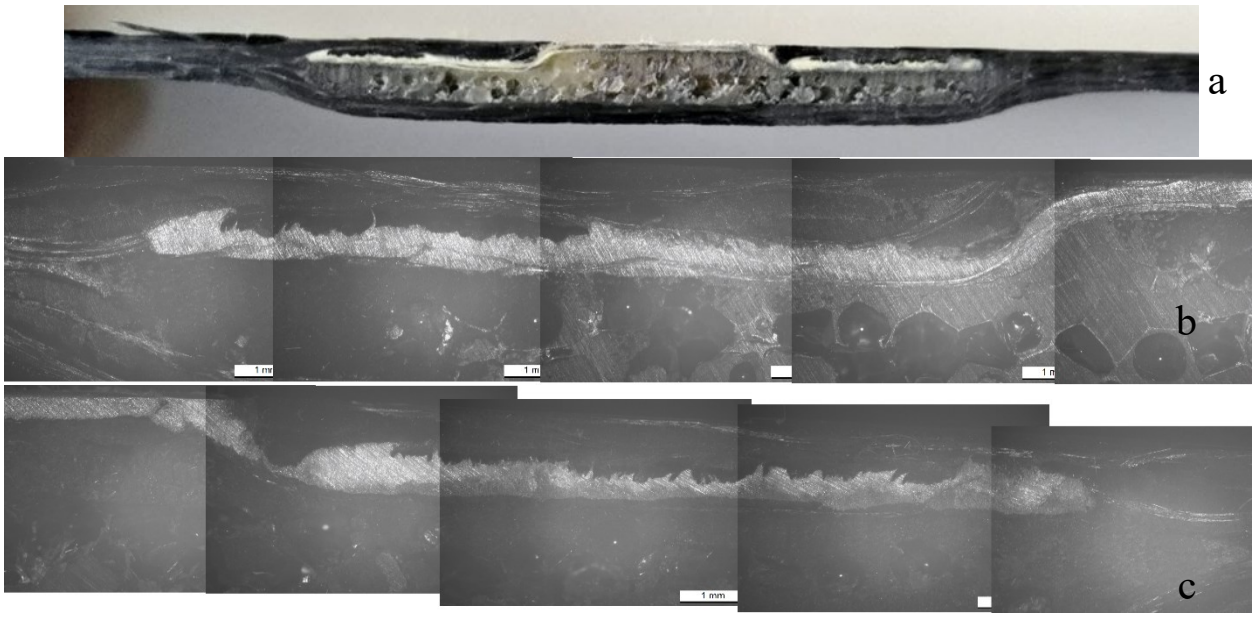

Figure 95 - a) Specimen sectioned along the longitudinal direction at load, b) optical microscope images left section, c) optical microscope images right section at 22kN load

Fig. 94-95 concerning the examined cutting section is difficult to determine the presence of damage due to the resolution used with the microscope.

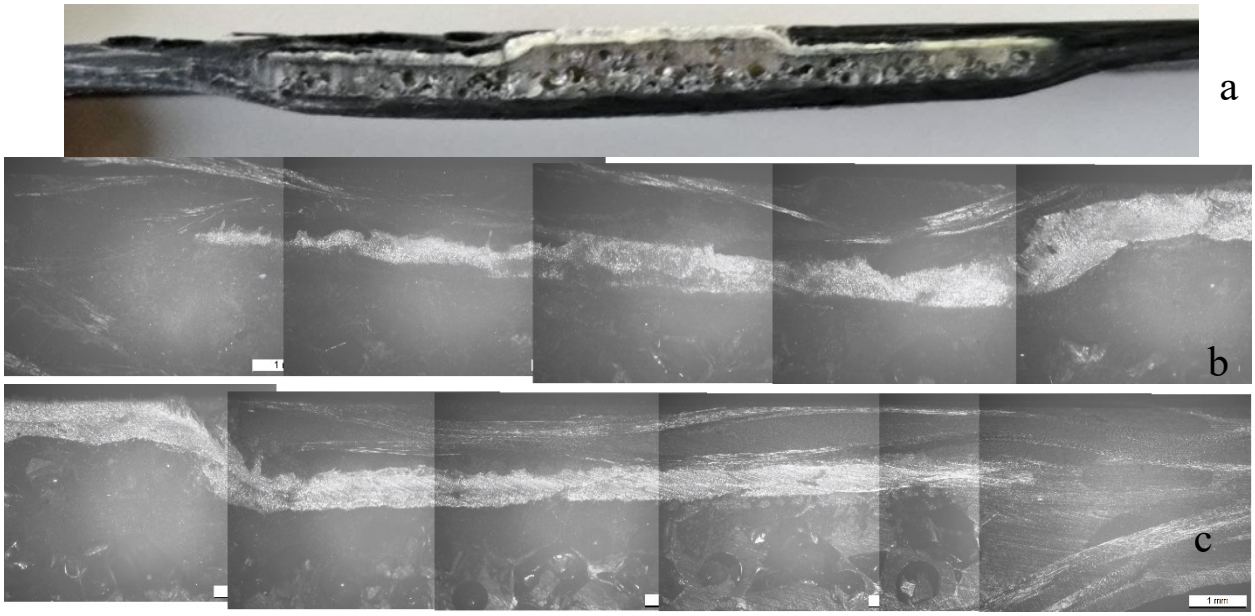

Figure 96 - a) Specimen sectioned along the longitudinal direction at load, b) optical microscope images left section, c) optical microscope images right section at 33kN load

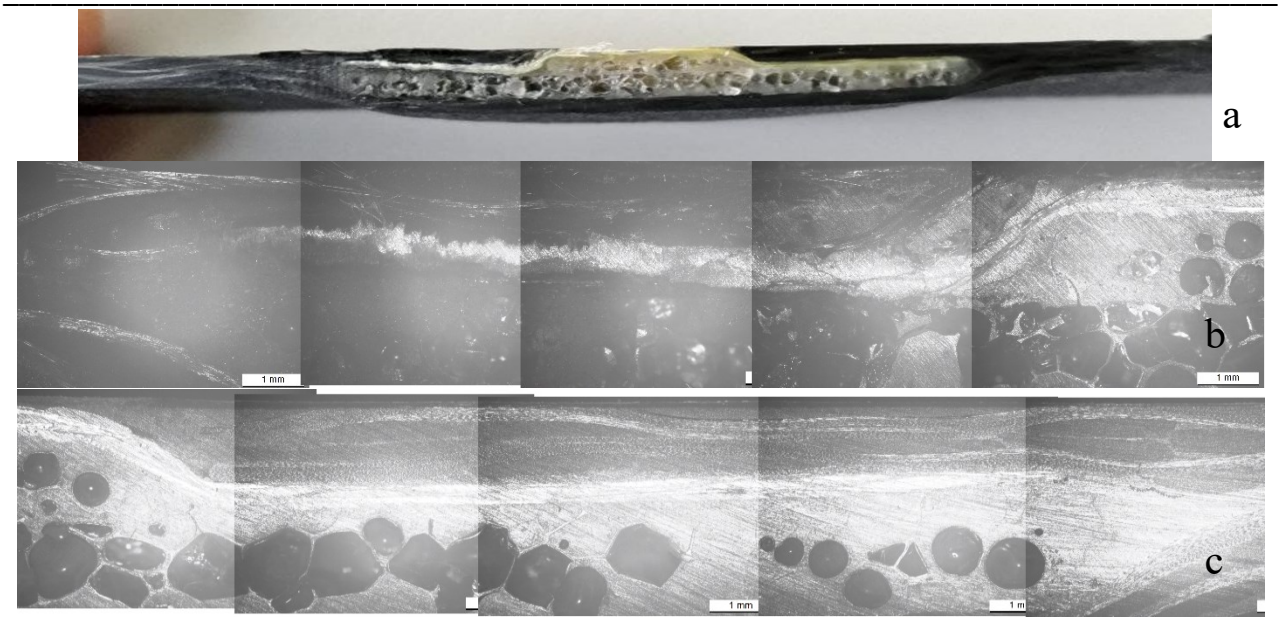

Figure 97 - a) Specimen sectioned along the longitudinal direction at load, b) optical microscope images left section, c) optical microscope images right section at 44kN load

Fig.96, referring to the third ramp in the section under consideration, shows no damage visible under the light microscope. Concerning Fig.97c, a small crack can be seen at the interface between C/K on the connection below the carbon fibre layers.

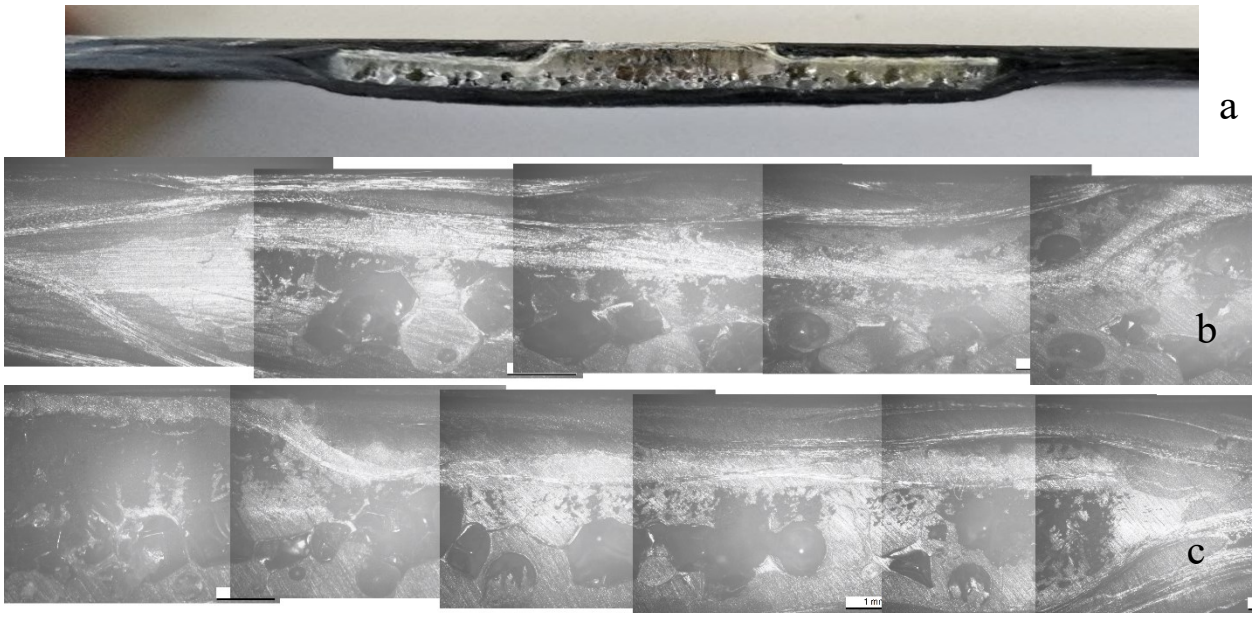

Figure 98 - a) Specimen sectioned along the longitudinal direction at load, b) optical microscope images left section, c) optical microscope images right section at 50kN load

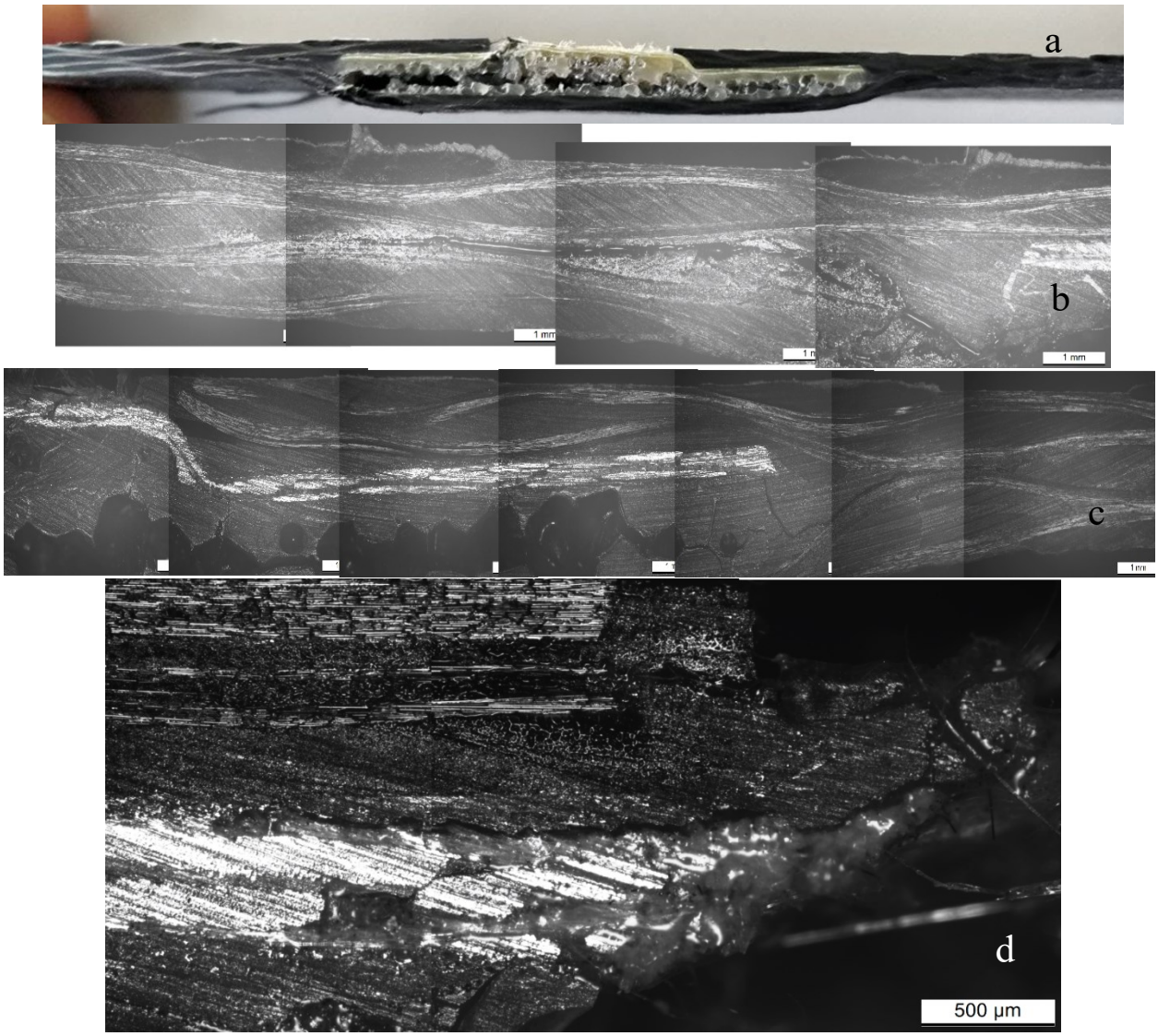

Figure 99 - a) Specimen sectioned along the longitudinal direction at load, b) optical microscope images left section at the end of kevlar patch, c) optical microscope image at the end of kevlar patch, d) K/C interface left side "window" right section after failure

In contrast, in Fig. 98b, damage to the Kevlar can be seen due to some fibre breakage or fibre pull-out. 97b shows cracks at the Rohacell/carbon interface.

The damage in Fig.99 on the section under consideration is visible, even to the naked eye (Fig.99a). In Fig.98b, the delamination proceeds between the two frontal and rear layers of CFRPs, coming from the rear plies. In Fig. 99c, on the other hand, we can see how the delamination arrives from the end of the kevlar patch and then proceeds inside the Roachell®, and as soon as it meets the carbon layers (back ply), it follows again until it crosses the posterior and front layers. Finally, Fig.99d shows the detachment of the K/C interface under the front skins (to the left of the kevlar window in Fig.99a) to continue until the fibres of the kevlar patch are damaged.

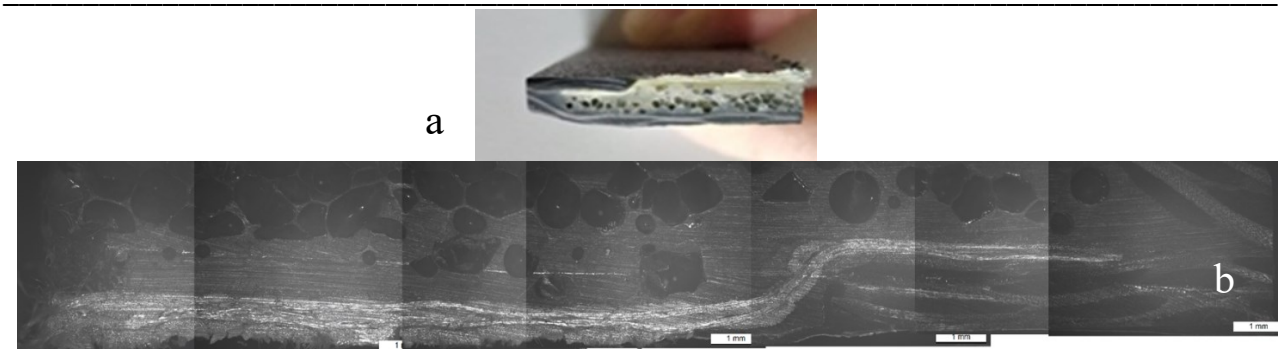

Figure 100 -a) Specimen sectioned along the transverse direction at load, b) optical microscope images at 11kN load

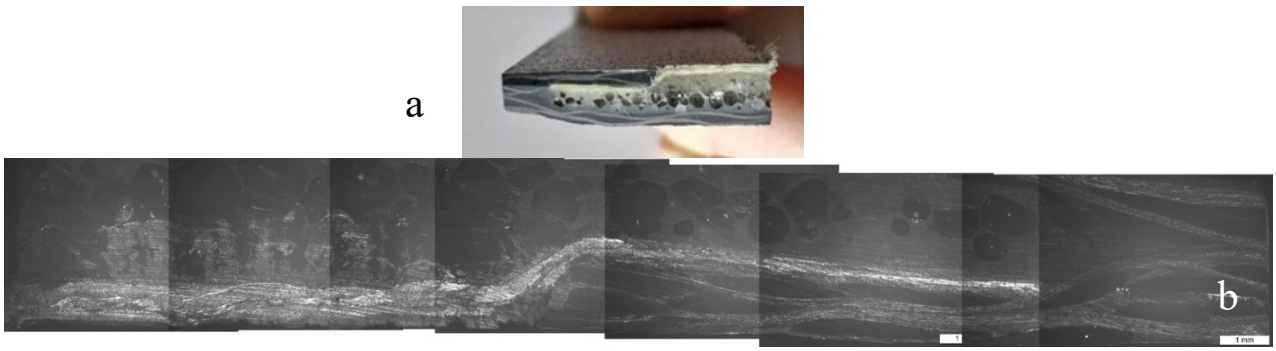

Figure 101 - a) Specimen sectioned along the transverse direction at load, b) optical microscope images at 22kN load

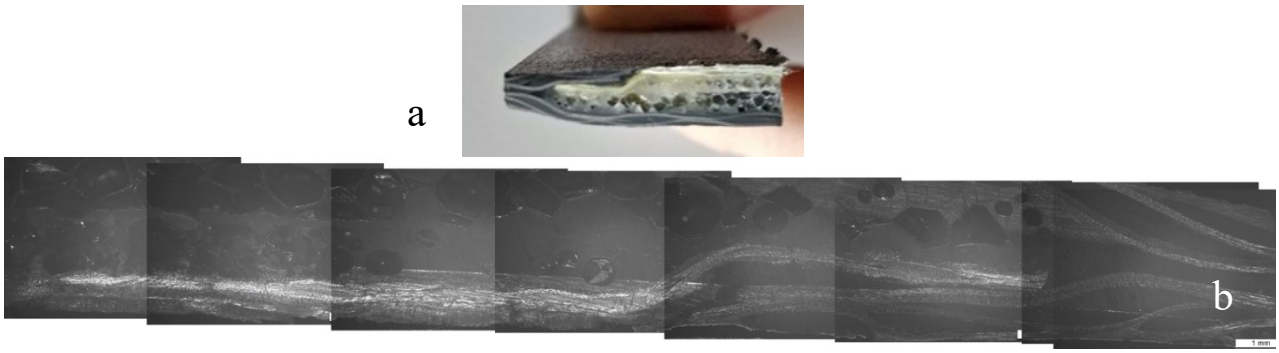

Figure 102 - a) Specimen sectioned along the transverse direction at load, b) optical microscope images at 33kN load

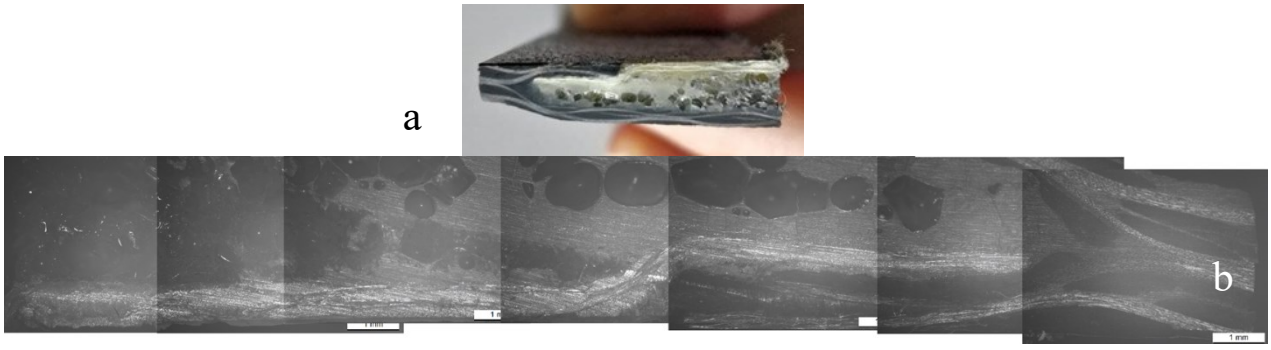

Figure 103 - a) Specimen sectioned along the transverse direction at load, b) optical microscope images at 44kN load

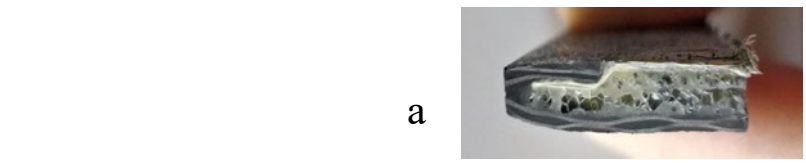

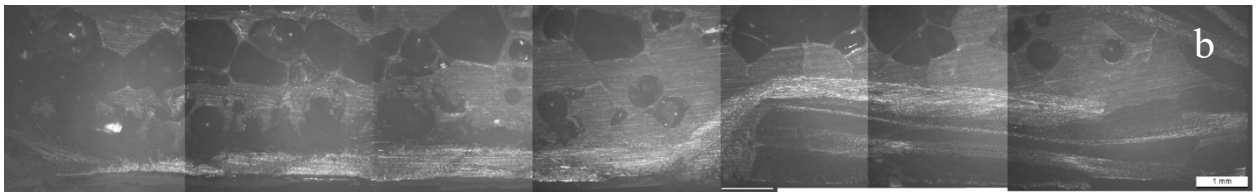

Figure 104 - a) Specimen sectioned along the transverse direction at load, b) optical microscope images at 50kN load

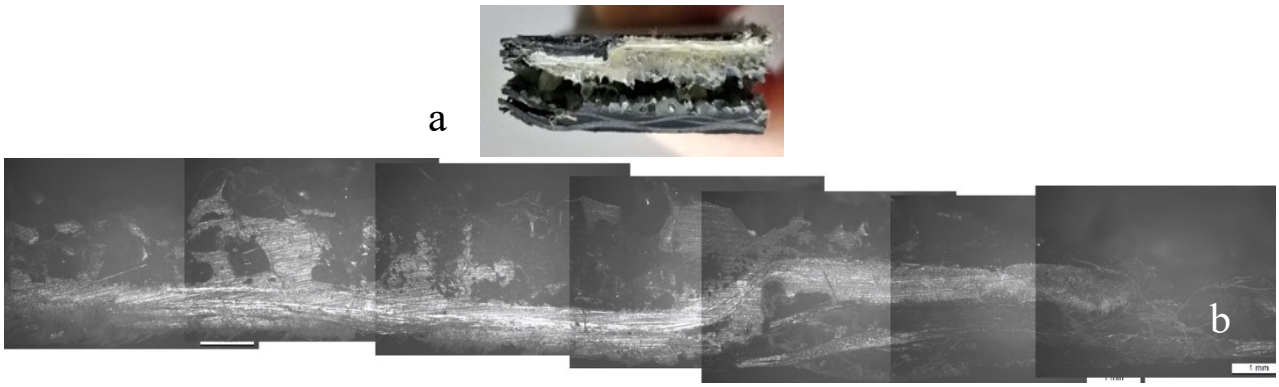

Figure 105 - a) Specimen sectioned along the transverse direction at load, b) optical microscope images at failure load

As might be expected, it is difficult to see any damage at low loads from the cross-section figures. However, when it comes to the failure (Fig.105a), the main source of damage is denoted by delamination, i.e., the detachment between Roachell and the two rear layers of CFRPs.

.

4 CONCLUSION

The results presented in this thesis will be divided according to the two macro-areas of reference. Some aspects that are key to the technology and had weaknesses in the application presented in this work will be highlighted.

4.1 RFID TECHNOLOGY

The study of implementing RFID technology within a composite material provided insight into some of its limitations.

Two commercial on-metal tags were studied and found within the imposed design constraints for this study. It was noticed early on that the readability of the tags is affected by embedding within a composite material, especially CFRPs.

The first step in understanding tag readability was designing and building mock-ups simulating different embedding conditions. Different covers were designed to be grouped into two areas: shielding and non-shielding material.

The next step was understanding the feasibility of embedding one of the two tags inside a coupon by reading each configuration individually.

The analysis of the RSMs allowed the reduction of the results domain, one configuration per tag. The configurations that had the most negligible effect on signal attenuation were: Fit 220 HT tag with a square chamfered groove and DCHP carbon (C) fibre cover and the Fit 400 HT tag in a circular groove with Kevlar (K) cover.

The coupons with the tag inside were then tested after the curing process.

The coupon with the Fit220HT tag and the carbon cover attenuated the signal completely. The coupon with the Fit400HT tag, on the other hand, was put under closer scrutiny and showed promising results for future applications. Distances close to 3m have been achieved.

The last step in this implementation study was to modify the groove where the tag is housed to prevent discontinuity problems in the material. With these modified coupons, better results were obtained than in their previous condition.

This feasibility study on the incorporation of an RFID tag allowed us to understand the limitations and merits of this case study.

Indeed, incorporating this technology within CFRPs is challenging to find in the literature. In this work, we wanted to go further. From a testing point of view, different possibilities of embedding a passive UHF RFID tag in a CFRPs component and being activated with an external antenna and, thus, communicating were considered. Despite the embedding, it was possible to achieve significant reading distances for several real-world scenarios.

4.2 MECHANICAL TESTING AND EFFECT OF THE EMBEDDED RFID

The design of the test specimens was based on the maximum dimensions given in the ASTM reference standard for tensile tests. The constraints imposed by our insert from the previous study were added. So, the maximum sample size was defined. The sample design is an additional piece of information compared to the experimental tests. Furthermore, to understand the variation of stress distribution on the specimen, specimens were obtained with lengths and widths 1, 1.5 and 2 times the base length.

Then, the T-H and T-W index failures in the test specimens were evaluated and allowed to understand which was the optimal specimen for future mechanical tests.

Furthermore, the position identified by the simulations as failure is very close to the actual failures in the mechanical tests.

The specimens' simulations will only show the maximum stress reached in the simulated part but will never simulate the real failure scenario.

The combined study of different tools for SHM and visual monitoring of the structural condition of a component under tensile stress showed outstanding potential but with some limitations.

The combined study of different tools for SHM and visual monitoring of the structural condition of a tensile component has shown exceptional potential but with certain limitations. Using AE allowed us to understand the possible damage involved during the tensile test. The parameters and data obtained were compared with data found in the literature. Subsequently, the types of damage

developed during the test were confirmed by visual tools, such as DIC, side camera and C-Scan. All damage was assessed considering the entirety of the test specimen, thus not discerning the damage involved per individual material.

The AE technology during quasi-static tensile testing through ANNs allowed identifying the types of damage involved in the component at a general level. Nevertheless, without the support of an advanced signal processing technique, it is difficult to establish and give information about the source of the noise a priori. Furthermore, it is difficult to establish a priori in a structure composed of several materials involved in the damage through AE if no studies are present in the literature or done on the matter. It must be noted that classification techniques require much knowledge and, therefore, a significant input.

Through the proposed ANNs, i.e., the SOM, remembering that it is an unsupervised classification technique, it was possible to define the signals received at different damage groups in a general way. These were then confirmed through visual systems such as DIC, C-scan and a side camera. By merging the information received from these instruments, it was possible to validate and quantify the damage involved in the structure. Moreover, subsequently, with the quasi-static tests divided into several ramps, the evolution of the damage was also determined.

Thus, through the support of the various instruments, it was possible to identify the different damages:

1. The ***quasi-static tensile test*** helped to understand which damages were affecting the structure.
2. The ***quasi-static tensile–interrupted tests***: showed and confirmed what had been seen previously. In addition, it allowed a better understanding of the evolution of the damages involved in the structure, particularly the delamination damage, which was subsequently confirmed first with the C-Scan and then with the optical microscope.

4.3 FUTURE WORKS AND FURTHER IMPROVEMENTS

Much more work could be done in both macro areas.

Having established the possibility of embedding RFID sensors in CFRPs, a first step is to investigate this further with gates in both an anechoic and industrial environment.

A second step is to expand with other methods of producing the specimens by modifying the grooves' geometries. This could give a better idea of the usability of this technology, being able to expand its adoption to different real-world situations. A further insight would be to understand how it affects the mechanical properties of the structure being mechanically different.

A third step is using ANNs, which in this study provided a general understanding of the damage involved in the structure. It is difficult to determine which materials are involved through damage classification. Therefore, further analysis will focus on studying individual materials undergoing tensile testing. Going even further into studying AE signals, understanding the speed of wave propagation within the specimen will allow us to proceed with the study of damage location. This analysis would make it possible to understand, without prior knowledge of the waveforms of individual materials, to assess where the event occurs during the test.

5 ACKNOWLEDGEMENTS

The work presented in this thesis would not have been possible without the help and support of several individuals, institutes and companies.

I would like to gratefully acknowledge the support, supervision and constant help of Prof. Alessandro Pirondi throughout the experimental work. I would also like to thank the research team and the University of Parma for their availability and facilities.

A second thank goes to Dallara Automobili, and a special appreciation to all the people who have accompanied me along this course: Vescovi Luca, Arbucci Fabrizio, Pernechele Chiara, Arturo Gaita and the entire DARC team. Without them, exploring new topics outside mechanical engineering would not have been possible.

A third thanks go to the Faculty of Aerospace Engineering of the TU Delft and Prof. Dimitrios Zarouchas for their hospitality and help since, without them, it would not have been possible to present part of the work in this thesis.

Also, immense gratitude goes to my whole family for their constant support during these three years.

Finally, I would like to thank all the people I have met during this journey in Italy and abroad. I want to thank all the guys I met and know at TU Delft that made me feel at home. Thank you to Davide, Gioele, Silvia, Eva, Abhas, Huub, Ferda, Wenjie, Morteza, Silvia and Dulcis in Fundo, the best officemate colleague I could ever meet…Rosy.

6 REFERENCES

[1] R. A. Smith, «Composite defects and their detection,» in *Materials science and engineering 3.1*, 2009, pp. 103-143.

[2] M. B. F. O. J. H. D. G. T. K. D. &. L. W. Brink, «Challenges and Opportunities of RFID Sensortags Integration by Fibre-Reinforced Plastic Components Production,» vol. 24, pp. 54-59, 2018.

[3] M. V. M. K. A. H. M. F. E. Hardi, «Use of RFID tags for monitoring resin flow and investigation of their influence on the mechanical properties of the composite,» *Procedia Manufacturing,* vol. 24, pp. 305-310, 2018.

[4] M. H. E. K. M. H. A. S. &. F. M. Veigt, «Curing Transponder – Integrating RFID transponder into glass fiber-reinforced composites to monitor the curing of the component,» *Procedia Manufacturing,* vol. 24, pp. 94-99, 2018.

[5] B. T. U. L. R. P. S. L. Merilampi S., «Embedded wireless strain sensors based on printed RFID tag,» *Sensor Review,* vol. 31, n. 1, pp. 32-40, 2011.

[6] F. P. B. E. Dewynter-Marty V, «Embedded Fiber Bragg Grating Sensors for Industrial Composite Cure Monitoring,» *Journal of Intelligent Material Systems and Structures,* vol. 9, n. 10, pp. 785-787, 1998.

[7] J. S. D. J.-A. M. Jung-Ting Tsai, «Cure strain monitoring in composite laminates with distributed optical sensor,» *Composites Part A: Applied Science and Manufacturing,* vol. 125, 2019.

[8] M. R. T. v. T. G. &. d. T. G. Blanchet, «Industry 4.0: The new industrial revolution. How Europe will succeed.,» In Think act. Munich: Roland Berger Strategy Consultants GmbH., 2014.

[9] V. T. G. C. a. G. C. d. S. J. Victor da Rocha Pasqualeto, «Industry 4.0 and RFID in the automotive sector a case study on the implementation of RFID technology in automaker's supply,» *Journal of Automation,* vol. 1, n. 2, pp. 78-92, 2018.

[10] L. S. V. Y. S. B. G. Arronche L., «Impact damage sensing of multiscale composites through epoxy matrix containing carbon nanotubes,» *Journal of Applied Polymer Science,* vol. 5, n. 128, pp. 2797-2806, 2013.

[11] US Dept. of Energy - Energy Efficiency & Renowable, «Fiber Reinforced Polymer Composite Manufacturing Workshop; Summary reoport,» Arlington, VA, 2014.

[12] F. E. Strassner M., «The Promise of Auto-ID in the Automotive Industry. Auto-ID-Labs,» 2003.

[13] S. K. P. K. B. Sumita Chaturvedi, «Study & Evaluation of Just-in-Time in Automobile Manufacturing Company,» *International Journal of Technical Research and Applications,* vol. 3, n. 4, 2015.

[14] P. Y.-Y. L. W.-M. Shi Y.-D., «The RFID Application in logistic and supply chain management,» *Research Journal of Applied Sciences,* vol. 4, n. 1, pp. 57-61, 2009.

[15] M. Z. M. Q. Paolo Andrea Carraro, «Health monitoring of cross-ply laminates: Modelling the correlation between damage evolution and electrical resistance change,,» *Composites Part A: Applied Science and Manufacturing,* vol. 82, pp. 151-158, 2016.

[16] Z. X. F. C. Wen Jie, «Damage detection of carbon fiber reinforced polymer composites via electrical resistance measurement,» *Composite: Part B,* vol. 42, n. 1, pp. 77-86, 2011.

[17] B. E. P. T. Zhang Han, «The use of carbon nanotubes for damage sensing and structural health monitoring in laminated composites: a review,» *Nanocomposites,* vol. 1, n. 4, pp. 167-184, 2015.

[18] W. &. T. L. Obitayo, «A Review: Carbon Nanotube-Based Piezoresistive Strain Sensors,» *Journal of Sensors,* p. 15, 2012.

[19] T. e. a. Bregar, «Carbon nanotube embedded adhesives for real-time monitoring of adhesion failure in high performance adhesively bonded joints,» *Scientific Reports,* vol. 10, n. 1, pp. 1-20, 2020.

[20] F. C. Campbell Jr, Manufacturing processes for advanced composites, Elsevier, 2003.

[21] A. P. L. V. F. A. F. G. D. Ambrosini, «Feasibility study for the implementation of RFID technology in CFRPs component,» in *IEEE International Conference on Omni-Layer Intelligent System (COINS)*, 2021.

[22] G. P. Talone, RFID Fondamenti di una tecnologia pervasiva, Fondazione Ugo Bordoni, 2008.

[23] C. A. C. Erick C. Jones, RFID and Auto-ID in Planning and Logistic - A Practical Guide for Military UID Application, CRC Press, 2016.

[24] OECD - Organisation for economic co-operation and development, «RFID - A focus on information security and privacy applications, impacts and country initiatives,» 2008.

[25] H. S. a. P. K. Ahsan Kamran, «RFID applications: an introductory and exploratory study,» *International Journal of Computer Science Issues,* 2010.

[26] S. A. Weis, «RFID (Radio Frequency Identification): Principles and Application,» MIT CSAIL, 2007.

[27] A. Italia, «RFID Introduzione alla tecnologia delle etichette intelligenti,» AIM Italia, 2006.

[28] K. Finkenzeller, RFID Handbook: Fundamentals and applications in contactless smart cards, radio frequency identification and near-field communication, 3rd Edition, Wiley, 2010.

[29] M. R. B. M. B. E. V. A. Rizzi Antonio, «Monitoraggio della catena del freddo del prodotto food mediante tecnologia RFID,» in *Logistica e tecnologia RFID*, Milano, Springer Milano, 2011, pp. 217-246.

[30] D. D. D. Supreetha Rao Aroor, «Evaluation of the State of Passive UHF RFID: An Experimental Approach,» *IEEE Systems Journal ,* vol. 1, n. 2, pp. 168-176, 2007.

[31] D. U. U. H. a. J. T. T. C. Gorldt, «Tracking and Tracing in Production Scenarios with passive RFID Transponders,» *3rd European Workshop on RFID Systems and Technologies,* pp. 1-6, 2007.

[32] Xerafy Dot On XS, «Xerafy Products XS series,» [Online]. Available: https://www.xerafy.com/xs-series.

[33] Omni-ID Fit220HT (datasheet), «https://omni-id.com,» [Online]. Available: https://omni-id.com/products/fit-220/.

[34] Omni-ID Fit400HT (datasheet), «https://omni-id.com,» [Online]. Available: https://omni-id.com/products/fit-400/.

[35] Zebra RFD 8500, «Zebra RFD Products,» [Online]. Available: https://www.zebra.com/it/it/products/rfid/rfid-handhelds/rfd8500.html.

[36] Laird RFID Antenna, «https://www.lairdconnect.com/,» [Online]. Available: https://www.lairdconnect.com/rf-antennas/rfid-antennas/s865-series-rfid-antenna.

[37] Impinj reader, «Impinj datasheet,» [Online]. Available: https://www.impinj.com/products/readers/impinj-speedway.

[38] W. F. R. W. H. Peters, «Digital imaging techniques in experimental stress analysis,» *Optical engineering,* vol. 21, n. 3, 1982.

[39] e. a. Sutton Michael A., «Determination of displacements using an improved digital correlation method,» *Image and Vision Compuiting,* vol. 1, n. 3, pp. 133-139, 1983.

[40] R. M. R. M. H. Q. M. M. N. M. &. D. M. A. H. Ma Quanjin, «Experimental investigation of the tensile test using digital image correlation (DIC) method,» *Materials Today: Proceedings,* vol. 27, pp. 757-763, 202.

[41] N. A. T. W. A. L. C. &. D. M. Hoult, «Experimental accuracy of two dimensional strain measurements using digital imge correlation,» *Engineering Structures,* vol. 46, pp. 718-726, 2013.

[42] E. M. F. C. J. T. L. d. S. a. P. d. C. V. Richter-Trummer, «Analysis of crack growth behavior in a double cantilever Analysis of crack growth behavior in a double cantilever processing techniques,» *Materialwissenschaft und Werkstofftechnik,* vol. 42 , n. 5, pp. 452-459, 2011.

[43] X. C. Rims Janeliukstis, «Review of digital image correlation application to large-scale composite structure testing,» *Composite Structure,* vol. 271, pp. 114-143, 2021.

[44] C. P. D. R. D. R. D. Adams, «A review of defect types and nondestructive testing techniques for composites and bonded joints,» *NDT international,* vol. 21, n. 4, pp. 208-222, 1998.

[45] A. Fahr, «Ultrasonic C-scan inspection of composite materials,» 1992.

[46] «Department of Electronic Tecnology of Budapest,» [Online]. Available: https://www.ett.bme.hu/meca/Courses/AIT/8_4.html. [Consultato il giorno 26 01 2021].

[47] Z. J. J. &. G. J. Bergant, «Ultrasonic C-Scan Testing of Epoxy/Glass Fiber Composite,» in *14th International Conference of the Slovenian Society for Non-Destructive Testing*, 2017.

[48] B. C. H. S. T. &. C. D. W. Ray, «Evaluation of defects in FRP composites by NDT techniques.,» *Journal of Reinforced Plastics and composites,* vol. 26, n. 12, pp. 1187-1192, 2007.

[49] T. B. E. &. T. N. G. Hasiotis, «Application of ultrasonic C-scan techniques for tracing defects in laminated composite materials,» *Journal of Mechanical Engineering,* vol. 57, n. 3, pp. 192-203, 2011.

[50] T. F. &. L. F. J. Drouillard, Acoustic emission: a bibliography with abstracts, New York: IFI/Plenum, 1979.

[51] T. F. Drouillard, Introduction to acoustic emission technology. Nondestructive testing handbook, 1987.

[52] T. Drouillard, «A history of acoustic emission,» *Journal of acoustic emission,* vol. 14, pp. 1-34, 1996.

[53] C. G. Ohtsu, «History and Fundamentals,» in *Acoustic Emission Testing: Basics for Research - Applications in Civil Engineering*, Springer Link, 2008.

[54] S. BH, «Acoustic emission under applied stress. Report ARL-150,» Lessels and Associates, Boston, 1961.

[55] B. a. C. S. a. B. G. Djordjevic, «Nondestructive test technology for the composites,» Ljubljana, 2009.

[56] S. K. A.-J. D. C. M. R. P. M. J. E. C. A. F. M. G. K. M. H. R. P. John P McCrory, «Damage classification in carbon fibre composites using acoustic emission: A comparison of three techniques,» *Composites Part B: Engineering,* vol. 68, pp. 424-430, 2015.

[57] M. G. M. E. M. P. S. A.-J. K. H. R. P. Davide Crivelli, «Localisation and identification of fatigue matrix cracking and delamination in a carbon fibre panel by acoustic emission,» *Composites Part B: Engineering,* pp. 1-12, 2015.

[58] V.-S. G. Hartmut Vallen, «AE Testing Fundamentals,Equipment, Applications,» *NDE.net,* vol. 7, n. 09, 2002.

[59] M. O. Christian U. Grosse, «Introduction,» Springer.

[60] M. O. Christian U. Grosse, «Parametric AE Analysis,» in *Acoustic Emission Testing*, Springer.

[61] L. S. Y. S. I. Y. X. &. L. S. V. Li, «Cluster analysis of acoustic emission signals for 2D and 3D woven carbon fiber/epoxy composites,» *Journal of Composite Materials,* vol. 50, n. 14, pp. 1921-1935, 2016.

[62] F. H. A. K. V. H. S. P. F. &. K. M. Lissek, «Acoustic emission for interlaminar toughness testing of CFRP: Evaluation of the crack growth due to burst analysis.,» *Composites Part B: Engineering,* vol. 136, pp. 55-62, 2018.

[63] M. A. N. D. Z. H. H. T. M. J. Milad Saeedifar, «Clustering of interlaminar and intralaminar damages in laminated composites under indentation loading using Acoustic Emission,» *Composites Part B: Engineering,* vol. 144, pp. 206-219, 2018.

[64] I. F. I. B. C. R. F. M. M. Bourchak, «Acoustic emission energy as a fatigue damage parameter,» *International Journal of Fatigue,* vol. 29, pp. 457-470, 2007.

[65] ASTM International, «E2983 - Standard Guide for Application of Acoustic Emission for Structural Health Monitoring,» 2019.

[66] D. Z. Milad Saeedifar, «Damage characterization of laminated composites using acoustic emission: A review,» *Composites Part B: Engineering,* 2020.

[67] L. L. S. V. Y. X. C. V. Li, «Cluster analysis of acoustic emission signals for 2D and 3D woven glass/epoxy composites,» *Composite Structures,* n. 116, pp. 286-299, 2014.

[68] A. Ajith, Artificial neural networks. Handbook of measuring system design, Oklahoma, USA, 2005.

[69] T. Kohonen, «The self-organizing map,» *Proceedings of the IEEE,,* vol. 78, n. 9, pp. 1464-1480, 1990.

[70] M. G. a. A. M. D. Crivelli, «Development of an artificial neural network processing technique for the analysis of damage evolution in pultruded composites with acoustic emission,» *Composites Part B: Engineering,* vol. 56, pp. 948-959, 2014.

[71] R. B. Heslehurst, Defects and damage in composite materials and structures, Boca Raton, FL, USA: CRC press, 2014.

[72] M. M. M. F. C. H. K. H. S. &. P. R. Eaton, «Characterisation of damage in composite structures using acoustic emission,» *Journal of Physics: conference series,* vol. 305, n. 1, pp. 12-86, 2011.

[73] M. Ajit, «Elastic waves from localized sources in composite laminates,» *IUTAM Symposium on Mechanical Waves for Composite Structures Characterization.,* pp. 1-23, 2001.

[74] r. J. Nimdum P., «Use of acoustic emission to discriminate damage modes in carbon fibre reinforced epoxy laminate during tensile and buckling loading,» in *15th European conference on composite materials - ECCM 15*, Venice, 2012.

[75] M. Babu e T. Prakash, «Characterisation of Fiber Failure Mode in T–700 Carbon Fiber Reinforced Epoxy,» *Russian Journal Nondestructive Testing,* vol. 50, pp. 45-57, 2014.

[76] R. Gutkin, C. Green, S. Vangrattanachai, S. Pinho, P. Robinson e P. Curtis, «On acoustic emission for failure investigation in CFRP: Pattern recognition and peak frequency analyses,» *Mechanical System Signal Process,* vol. 25, pp. 1393-1407, 2011.

[77] S. H. R. G. N. Godin, «Integration of the Kohonen's self-organising map and k-means algorithm for the segmentation of the AE data collected during tensile tests on cross-ply composites,» *NDT & E International,* vol. 34, n. 4, pp. 299-309, 2005.

[78] P. A. M. W. a. R. B. F. J. P J De Groot, *Composites Science and Technology,* vol. 55, n. 4, pp. 405-412, 1995.

[79] C. R. Ramirez-Jimenez, «Identification of failure modes in glass/polypropylene composites by means the primary frequency content of the AE event,» *Composites Science and Technology,* vol. 60, pp. 1819-1827, 2004.

[80] Y. A. DZENIS e J. 2. 3.-1. 1.-1. QIAN, «Analysis of microdamage evolution histories in composites.,» *International journal of solids and structures,,* vol. 38, n. 10-13, pp. 1831-1854, 2001.

[81] P. D. P. Ding, Q. Li e X. Huang, «Classification of acoustic emission sources produced by carbon/epoxy composite based on support vector machine,» in *IOP Conference Series: Materials Science and Engineering*, Beijing, 2015.

[82] ASTM International, «D3039-D3039M - Standard Test Method for Tensile Properties of Polymer Matrix Composite Materials,» 2014.

[83] Abaqus, «Abaqus documentation,» [Online]. Available: https://abaqus-docs.mit.edu/2017/English/SIMACAEEXCRefMap/simaexc-c-docproc.htm.

[84] «Correlated solution,» [Online]. Available: https://correlatedsolutions.eu/. [Consultato il giorno 01 2022].

[85] Olympus, «Olympus,» 01 2022. [Online]. Available: https://www.olympus-ims.com/it/shop/item/269-productId.570441332.html.

[86] «Leica microsystem,» 02 2022. [Online]. Available: https://www.leica-microsystems.com/products/light-microscopes/p/leica-dmi8-id/.

[87] G. C. M. R. W. Meisam Jalalvand, «Damage analysis of pseudo-ductile thin-ply UD hybrid composites – A new analytical method,» *Composites Part A: Applied Science and Manufacturing,* vol. 69, pp. 83-93, 2015.

[88] G. C. M. R. W. Meisam Jalalvand, «Parametric study of failure mechanisms and optimal configurations of pseudo-ductile thin-ply UD hybrid composites,» *Composites Part A: Applied Science and Manufacturing,* vol. 74, pp. 123-131, 2015.

[89] P. S. M. J. G. C. M. R. W. Mohamad Fotouhi, «Detection of fibre fracture and ply fragmentation in thin-ply UD carbon/glass hybrid laminates using acoustic emission,» *Composites Part A: Applied Science and Manufacturing,* vol. 86, pp. 66-76, 2016.

[90] ASTM, «E750 - Standard Practice for Characterizing Acoustic Emission Instrumentation,» 2020.

[91] M. D. A. B. M. C. R.A.A. Lima, «On crack tip localisation in quasi-statically loaded, adhesively bonded double cantilever beam specimens by acoustic emission,» *Theoretical and Applied Fracture Mechanics,* vol. 118, 2022.

[92] R. P. Silhouettes, «A graphical aid to the interpretation and validation,» *Computational and Applied Mathematics,* vol. 20, 1987.

[93] B. L. Davies DL, «A cluster separation measure,» *IEEE,* vol. 1, n. 2, 1979.

[94] H. J. Calinski RB, «A dendrite method for cluster analysis,» *Communications in Statistics,* vol. 3, 1974.

[95] M. D. A. B. M. C. R. A. A. Lima, «On crack tip localisation in quasi-statically loaded, adhesively bonded double cantilever beam specimens by acoustic emission,» *Theoretical and Applied Fracture Mechanics,* vol. 118, 2022.

[96] D. Z. R. A. R. B. J.A. Pascoe, «Using acoustic emission to understand fatigue crack growth within a single load cycle,» *Engineering Fracture Mechanics,* vol. 194, pp. 281-300, 2018.

[97] M. S. P. J. M. C. G. &. W. M. R. Fotouhi, «Detection of fibre fracture and ply fragmentation in thin-ply UD carbon/glass hybrid laminates using acoustic emission,» *Composites Part A: Applied Science and Manufacturing,* vol. 86, pp. 66-76, 2016.

[98] J. C. Y. L. J. Z. P.F. Liu, «A study on the failure mechanisms of carbon fiber/epoxy composite laminates using acoustic emission,» *Materials & Design,* vol. 37, pp. 228-235, 2012.

[99] A. M. M. B. A. B. H.Y. Chou, «Acoustic emission analysis of composite pressure vessels under constant and cyclic pressure,» *Composites Part A: Applied Science and Manufacturing,* vol. 70, pp. 111-120, 2015.

[100] V. K. T.H. Loutas, «Health monitoring of carbon/carbon, woven reinforced composites. Damage assessment by using advanced signal processing techniques. Part I: Acoustic emission monitoring and damage mechanisms evolution,» *Composites Science and Technology,* vol. 69, n. 2, pp. 265-272, 2009.